

Metallicity estimation of MW, SMC and LMC classical Cepheids from the shape of the *V*- and *I*-band light curves.

V. Hocdé , R. Smolec , P. Moskalik, O. Ziółkowska, R. Singh Rathour

Nicolaus Copernicus Astronomical Centre, Polish Academy of Sciences, Bartycka 18, 00-716 Warszawa, Poland
email : vhocde@camk.edu.pl

Received ... ; accepted ...

ABSTRACT

Context. Estimating metallicity of classical Cepheids is of prime importance for studying metallicity effect on stellar evolution, chemical evolution of galaxies, and ultimately its impact on period-luminosity relation used in the extragalactic distance scale.

Aims. We aim first at establishing new empirical relations for estimating the iron content of classical Cepheids for short and long-periods based on Fourier parameters from the *V*- and *I*-band light curves. Then we apply these relation to Cepheids from Milky Way (MW), Small and Large Magellanic Clouds (SMC and LMC) available in the literature.

Methods. We retrieved metallicity of 586 fundamental mode Cepheids from spectroscopic determinations in the literature and we found well sampled light-curves for 545 of them in different *V*-band catalogues. We then describe the shape of these light curves by applying Fourier decomposition and we fit empirical relations between the Fourier parameters and the spectroscopic metallicities, separately for short- ($2.5 < P < 6.3$ days) and for long-period Cepheids ($12 < P < 40$ days). We verify the accuracy of these relations by applying them to *V*-band light curves of Cepheids from the Small and Large Magellanic Clouds and comparing the derived metallicities to the literature. We calibrate new interrelations of Fourier parameters to convert these empirical relations into the *I*-band. We then use these *I*-band relations to derive the metallicity of fundamental mode Cepheids from OGLE-IV for MW, SMC and LMC (486, 683 and 1678 stars respectively). Last, we map the metallicity distribution in these galaxies for investigating potential application in galactic archeology.

Results. For short-period Cepheids, our best fit is given for a relation based on explicit amplitude terms A_1 and A_2 of the first and second harmonic respectively. In the *V* and *I* band these empirical relations are found with an intrinsic scatter (rms) of 0.12 dex. This relation performs well for estimating [Fe/H] between about -0.5 and 0.1 dex but remains uncertain outside this range because of the lack of spectroscopic metallicity for the calibration. For the long-period Cepheids we found a metallicity dependence on the Fourier parameters A_1 , ϕ_{21} and R_{41} . We found an intrinsic scatter of 0.25 dex when using this relation. These empirical relations in *V* and *I* bands are able to derive the mean metallicity of a sample of MW, SMC and LMC Cepheids in agreement with literature values within 1σ . We also show that these relations are precise enough to reconstruct the radial metallicity gradients within the MW from OGLE data.

Conclusions. The empirical relations in the *V* and *I* bands calibrated in this paper for short and long-period Cepheids provide a new useful tool to estimate the metallicity of Cepheids which are not accessible by spectroscopy. The calibration can be improved with further high-resolution spectroscopic observations of metal-poor Cepheids and homogeneous photometries in *V* and *I* bands.

Key words. Techniques : photometric, spectroscopic – Methods: data analysis – stars: variables: Cepheids – Galaxy: abundances.

1. Introduction

Cepheids are yellow supergiant variable stars which are essential for distance scale determination as a result of the correlation between their pulsation period and their luminosity (hereafter PL relation) (Leavitt 1908; Leavitt & Pickering 1912). However, the PL relation is still affected by uncertainties on both zero point and slope, which represent one of the main error contribution to the extragalactic distance scale (Riess et al. 2021).

The chemical composition plays an important role on the evolution and the brightness of the Cepheids. As a consequence, metallicity introduces a bias on the zero-point when PL relation is calibrated in different galaxies which have different mean metallicities. The sign of the metallicity term in the Period-Luminosity-Metallicity (PLZ) relation, which also depends on the given passband, is still theoretically and observationally debated, see for example Caputo et al. (2000); Bono et al. (2008); Fiorentino et al. (2013); Gieren et al. (2018); Ripepi et al. (2021); Breuval et al. (2021); Wielgórski et al. (2022); Breuval et al. (2022); De Somma et al. (2022).

Breuval et al. (2021); Wielgórski et al. (2022); Breuval et al. (2022); De Somma et al. (2022).

Determining the metallicity for a large number of Cepheids is also crucial for constraining pulsation and evolution models. The accurate prediction of the Cepheid evolution as well as its pulsation properties are necessary to answer the problem of mass discrepancy of Cepheids (see, e.g. Neilson et al. 2011). The derived stellar mass can be up to 20% lower in pulsation models as compared to stellar evolution models; this discrepancy is still unresolved after 50 years of research (see, e.g. Stobie 1969; Bono et al. 2006; Keller 2008).

Until now, high-resolution spectroscopic observations have led to the determination of the iron-to-hydrogen ratio [Fe/H] for several hundreds of Cepheids, which are in majority in the Sun's vicinity within about 5 kpc. Indeed, these observations are difficult to apply for faint stars which are distant or in the line of sight of significantly reddened environment such as the Galactic Center. However, this limitation can be overcome owing to medium- and high-resolution near-infrared spectroscopy (Inno

et al. 2019; Kovtyukh et al. 2019, 2022c). An interesting alternative to spectroscopy is to estimate the metallicity of the Cepheids using the shape of the light-curve since it contains the information on its physical properties such as pulsation period, temperature and chemical composition. Thus it is possible to infer these parameters using photometry. In the case of RR Lyrae stars, Jurcsik & Kovacs (1996) have shown the possibility to estimate [Fe/H] from the shape of the *V*-band light curve described by Fourier parameters. Several authors have then extended their work to various other photometric wavelength such as in the I_c -band (Smolec 2005; Dékány et al. 2021), or in optical and infrared (Mullen et al. 2021). Other recent approaches make use of learning machine algorithms to infer physical parameters of Cepheids and RR Lyrae stars from the shape of the light curve (Miller et al. 2015; Hajdu et al. 2018; Bellinger et al. 2020). Among photometric methods to estimate the metallicity we also mention the possibility of the inversion of PLZ relation (if the metallicity term is characterized). Bono et al. (2010) also suggested that the differences in distance moduli inferred by different Period-Wesenheit relation can be used to estimate individual metallicities.

In the case of Cepheids, several studies have shown the impact of the chemical abundance on the amplitudes (Klagyivik & Szabados 2007; Bono et al. 2000; Szabados & Klagyivik 2012; Majaess et al. 2013). An attempt was made by Zsoldos (1995) to calibrate a relation with Fourier parameters. The first reliable empirical relation for short-period Cepheids ($P < 6.3$ days) based on the Fourier parameters R_{21} and R_{31} was proposed by Klagyivik et al. (2013). However these relations are based on a small sample of stars and do not cover the metal-poorer regime typical of the Magellanic Cloud Cepheids. These relations were used by Clementini et al. (2019) to estimate the metallicity of Cepheids of *Gaia* DR2. These authors found metallicity distributions for SMC, LMC and MW Cepheids that are shifted by about +0.2 dex compared to the literature values, which might be a hint of the calibration issue. On the other hand, there is still no empirical relation available for estimating the chemical abundance of intermediate ($6 < P < 10$ days) Cepheids. This is due to the resonance between the fundamental and second overtone mode which strongly affects the shape of the light-curve (Simon & Schmidt 1976; Buchler et al. 1990). In the case of long-period ($P > 10$ days) Cepheids, Scowcroft et al. (2016) established a relation based on *Spitzer* infrared colors at 3.6 and 4.5 μm . A complementary relation based on Fourier decomposition of the light curve in common photometric bands would be however useful and convenient to measure directly the metallicity of extragalactic Cepheids. Thus, new photometric metallicity formula, properly calibrated and applicable over a wide range of pulsation periods is needed. The estimation of [Fe/H] for a large number of Galactic and extragalactic Cepheids will be valuable for thorough comparison with evolution and pulsation theoretical models. Combining these estimations with the accurate trigonometric parallaxes of these stars provided by *Gaia* can also help to recalibrate the metallicity dependence of the PL relationship and to refine the cosmic distance scale.

In this paper we first present new empirical relations for estimating the metallicity of Cepheids, based on the Fourier parameters of the *V*-band light curve. We improve qualitatively and quantitatively the calibration for the short-period Cepheids ($2.5 < P < 6.3$ days) and we provide for the first time an empirical relation for estimating [Fe/H] of the long-period Cepheids ($12 < P < 40$ days). Then, we convert these relations to the *I*-band and we use them to estimate the metallicities of Cepheids in the MW, SMC and LMC. In Section 2 we present the data

set used for spectroscopic metallicities and for the *V*-band light curves. In Section 3 we apply Fourier decomposition of the light curves and we then establish empirical relations for short and long-period Cepheids in Sections 4 and 5 respectively. In Section 6 we calibrate interrelations of Fourier parameters and we use it to convert *V*-band relations into the *I*-band. Finally, we apply them to estimate the metallicity of Cepheids in the MW, SMC and LMC. We then discuss the results and conclude in Section 7 and 8.

2. Metallicity and V-band light curve data sets

In this section we first gather the spectroscopic metallicities of Cepheids from the literature, then we cross-match these stars with existing photometric catalogues in the *V*-band.

2.1. Metallicity

2.1.1. Milky Way Cepheids

The two largest data sets of metallicities for Galactic Cepheids are given by Luck (2018) and Groenewegen (2018) with 435 and 452 Cepheids respectively (all pulsation modes included). While Luck (2018) determined homogeneously the metallicities, Groenewegen (2018) compiled different data from the literature (mostly from Genovali et al. (2014, 2015)) and transformed them into the same scale.

In this paper, we first re-scaled the [Fe/H] abundance of Luck (2018) to solar abundance value of $A(\text{Fe})_\odot = 7.50$ given by Asplund et al. (2009). The iron-to-hydrogen ratio is given by

$$[\text{Fe}/\text{H}] = A(\text{Fe})_\star - A(\text{Fe})_\odot \quad (1)$$

where $A(\text{Fe}) = \log(\text{NFe}/\text{NH}) + 12$ is the logarithmic iron abundance with respect to hydrogen. In the following, all the metallicity data set discussed in this paper will be consistently re-scaled to this solar reference if needed. Then we cross-matched these two data sets to obtain a sample of 478 Milky Way Cepheids. 409 stars are in common between these two catalogues and we derived a mean offset of $-0.07 \text{ dex} \pm 0.06$ which is used to correct the iron abundance of Groenewegen (2018). We rejected 17 stars of our final sample because they are discrepant at more than 2σ between these two data sets, and thus the measurements may not be reliable. When possible, metallicity from Luck (2018) are preferred in the following of our study since they were determined from a single homogeneous method. If abundances are not available in this latter study, we then chose abundances from Groenewegen (2018). We also followed the preference order among the different references as defined by this author. This merge data set constitutes our main metallicity sample. Additional spectroscopic determination were found in Trentin et al. (2022) (44 fundamental mode Cepheids), Kovtyukh et al. (2022a) (54 fundamental mode Cepheids) and Ripepi et al. (2021) (19 fundamental mode Cepheids). From Kovtyukh et al. (2022a) we found 13 stars in common with our main metallicity sample. We derived a mean offset of -0.06 ± 0.11 which is used to correct the iron abundance of Kovtyukh et al. (2022a). Finally, fundamental mode classification is verified directly from Fourier decomposition of the *V*-band light curves presented in the next section. To this end, stars which are discrepant with the Hertzsprung progression of fundamental mode Cepheids are discarded since they can belong to other pulsation modes (Antonello & Poretti 1986; Antonello et al. 1990).

The final metallicity sample consists of 472 fundamental mode MW Cepheids with spectroscopic metallicities. For an

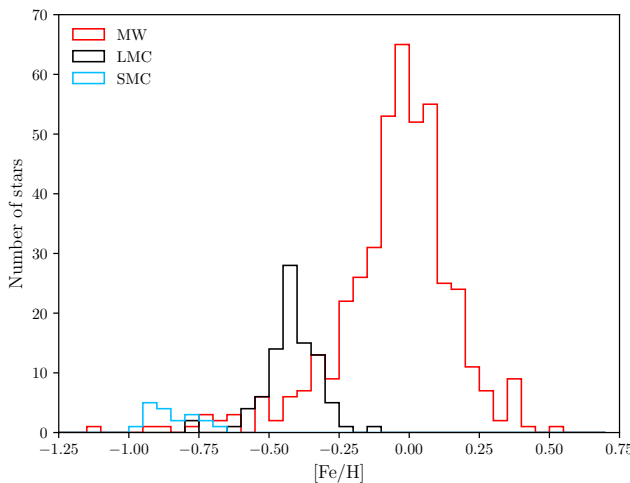


Fig. 1: Histogram of the iron abundance of the calibration sample (545 fundamental mode Cepheids with *V*-band light-curve) gathered and re-scaled from the literature.

overview of the calibration sample construction see Table 1. Although our sample might be inhomogeneous because of the different source of metallicity, we emphasize that about 90% of metallicities for the MW Cepheids of this sample are taken from a single source (specifically, from Luck (2018), Table C.1).

2.1.2. LMC and SMC Cepheids

We retrieved the iron abundances of 89 stars in the recent work of Romaniello et al. (2022). However, we note that Romaniello et al. (2022) re-analysed 21 LMC Cepheids from Romaniello et al. (2008) and found systematic errors in this latter study, yielding an additive offset of -0.11 dex to obtain the new values. Therefore, we assumed that the 14 SMC Cepheids from Romaniello et al. (2008) are affected by the same error. We thus retrieved these stars and we corrected by applying this offset. We found 4 additional Cepheids from the SMC and 5 stars from the LMC cluster NGC 1866 given by Lemasse et al. (2017). From NGC 1866, 2 more Cepheids are retrieved in Molinaro et al. (2012).

The final metallicity sample, combining MW, LMC, and SMC Cepheids, consists of 586 Cepheids which span a $[\text{Fe}/\text{H}]$ range from about -1.0 to $+0.4$ dex. It is however difficult to attribute consistent uncertainties for each measurement. Indeed different observations and methods are used to measure the iron abundance and the uncertainties may not be homogeneous from a study to another. For example, da Silva et al. (2022) have studied the impact of different systematics on metallicity measurement. In addition, we cannot derive any systematic difference of $[\text{Fe}/\text{H}]$ between the two largest data sets, that are the MW sample of Luck (2018) and the LMC sample of Romaniello et al. (2022) since they have no stars in common. Therefore we associated a conservative uncertainty of ± 0.15 dex to every abundance in our sample. This value represents an upper limit for most of the uncertainties, and is also consistent with the mean uncertainty from the sample of Luck (2018).

2.2. *V*-band light curves

The first objective of this work is to increase the sample of Cepheids with both spectroscopic metallicity and well sampled *V*-band light curve. Thus, we do not limit our sample to a single catalogue as it was done by Klagyivik et al. (2013) who used catalogue from Berdnikov (2008), but we rather cross-match the metallicity sample with different catalogues in the *V*-band. For MW Cepheids we have retrieved 169 stars in the All-Sky Automated Survey (ASAS) catalogue (Pojmanski 2002) and 438 stars from the All-Sky Automated Survey for Supernovae (ASAS-SN) catalogue (Jayasinghe et al. 2018). We also extracted 349 stars from Berdnikov (2008). Among the 472 fundamental mode Cepheids with spectroscopic metallicities we thus found 438 stars which have also a light curve in the *V*-band.

For SMC and LMC stars we first collected the light curves from Optical Gravitational Lensing Experiment (OGLE) publicly available¹ (Soszyński et al. 2008, 2010). The SMC and LMC light curves were retrieved from OGLE III and OGLE IV. For 35 stars the pulsation cycle is poorly covered or light curves are not available. For 29 of them we retrieved the light curves from ASAS-SN. For the remaining 6 stars we could not find any *V*-band light curves in the literature. Our LMC and SMC sample thus consists of 107 fundamental Cepheids from LMC and SMC with both spectroscopic metallicities and *V*-band light curves with an excellent phase coverage. In the next section, we apply Fourier decomposition to every *V*-band light curves from the different catalogue and we select the best fit for MW Cepheids among the different *V*-band catalogues.

3. Fourier decomposition of the *V*-band light-curve

Fourier decomposition is a very useful technique to study the structure of light curves. In particular the Fourier parameters describe efficiently the bump progression (Hertzsprung 1926). The favored hypothesis to explain the bump progression is a resonance between the fundamental and the second overtone pulsation modes (Simon & Schmidt 1976), characterized by a pulsation period of P_0 and P_2 respectively. This resonance model is qualitatively reproduced by hydrodynamical models (Buchler et al. 1990) and quantitatively using the amplitude equation (Kovacs & Buchler 1989). Alternatively, the echo model proposes that a wave pressure travels inward from He ionization zone and echoes on the stellar core, then travels back to reach the surface and produces the observed bump on the light curves (Whitney 1956; Christy 1968, 1975). For arguments against echo hypothesis see Klapp et al. (1985).

For each light curve we applied a Fourier series of the form:

$$m(t) = A_0 + \sum_{k=1}^n A_k \cos[k\omega t + \phi_k] \quad (2)$$

where $m(t)$ is the magnitude observed at the time t and $\omega = 2\pi/P$, A_k and ϕ_k are the amplitude and the phase of the k harmonic. We used the dimensionless Fourier parameters introduced by Simon & Lee (1981):

$$R_{i1} = \frac{A_i}{A_1} \quad (3)$$

$$\phi_{i1} = \phi_i - i\phi_1 \quad (4)$$

¹ https://ogledb.astroww.edu.pl/~ogle/OCVS/ceph_query.php

Table 1: Summary of the data sets used to compose the calibration sample for empirical metallicity relation from the V -band (see Sect. 2 and 3). The final data set consists of 545 fundamental mode Cepheids and is presented in detail in C.1. The first row describes the spectroscopic metallicities retrieved from the literature for a total of 586 stars (see Sect. 2.1). The second row describes the V -band light curves we found in the literature after cross-matching with the precedent metallicity sample (see Sect. 2.2).

| | MW | LMC | SMC | |
|--------------------------|--|--|--|-----|
| Metallicity (Sect. 2.1) | Luck (2018) (435) Groenewegen (2018) (452) Ripepi et al. (2021) (19) Trentin et al. (2022) (44) Kovtyukh et al. (2022a) (54) | Romanillo et al. (2022)(89) Lemasle et al. (2017) (5) Molinaro et al. (2012) (2) | Romanillo et al. (2008)(14) Lemasle et al. (2017) (4) | |
| Total cross-match [Fe/H] | fundamental only : 472 | 96 | 18 | 586 |
| V-band (Sect. 2.2) | ASAS (169) ASAS-SN (438) Berdnikov (2008) (349) | OGLE IV (72) OGLE III (3) ASAS-SN (15) | OGLE III (4) ASAS-SN (14) | |
| Total ([Fe/H]+V-band) | 438 | 89 | 18 | 545 |

where ϕ_{i1} are then adjusted to lie between 0 and 2π . For each curve, the order of the fit n is iterated until $A_n/\sigma_{A_n} > 4$. The uncertainty of the fit is given by

$$\sigma^2 = \frac{\chi^2}{N - 2n - 2} \quad (5)$$

where N is the number of data points, n the order of the fit and χ^2 is the sum of the squared residuals. This uncertainty is used to apply an iterative 3σ clipping during the fitting process. For each light-curve, the period is estimated using Lomb-Scargle method (Lomb 1976; Scargle 1982). The uncertainty on the Fourier parameters are derived following Petersen (1986). For every light-curve of the different catalogues in the V -band, we selected the fit having the smallest uncertainty for Fourier parameter ϕ_{21} . This criterion also ensures Fourier parameters are accurate enough for establishing empirical relations. A selection based on the fit uncertainty as defined by Eq. 5 is also possible, but this criterion is less accurate to select the best fits. We also inspected visually the light curves to ensure the overall quality of the fits in particular for the period ranges studied in this paper in Sect. 4 and 5. The final sample of Cepheids with well sampled V -band light curves and spectroscopic metallicities consists of 545 stars and is presented in Table C.1. The metallicity distribution of this sample is presented in Fig. 1, the distribution of the fit uncertainty in our sample is shown in Fig. 2 and Fourier parameters are presented in Fig. 3.

We note that a significant fraction of Cepheids are binary or multiple systems (Szabados 2003; Kervella et al. 2019). Following Klagyivik et al. (2013) we also included binary stars in our final sample since in most cases, the companions do not affect the amplitude ratios and phases. However, the presence of companion lead to smaller peak-to-peak amplitude and the Fourier amplitudes on a magnitude scale. Although most of the companions are main-sequence stars with a negligible contribution to the total luminosity (Karczmarek et al. 2022), some Cepheids can have red giant companion that can affect significantly the luminosity and thus the amplitudes (Pilecki et al. 2021; Karczmarek et al. 2022). Similarly, several studies have shown the occurrence of circumstellar envelopes (CSE) around Cepheids (Kervella et al. 2006; Mérand et al. 2006; Gallenne et al. 2013; Nardetto et al. 2016; Gallenne et al. 2021). Thus these envelopes could decrease the amplitude in case of constant emission in the infrared (Hocdé et al. 2020b,a, 2021; Kovtyukh et al. 2022b). In the following of the paper we also work with Fourier amplitudes,

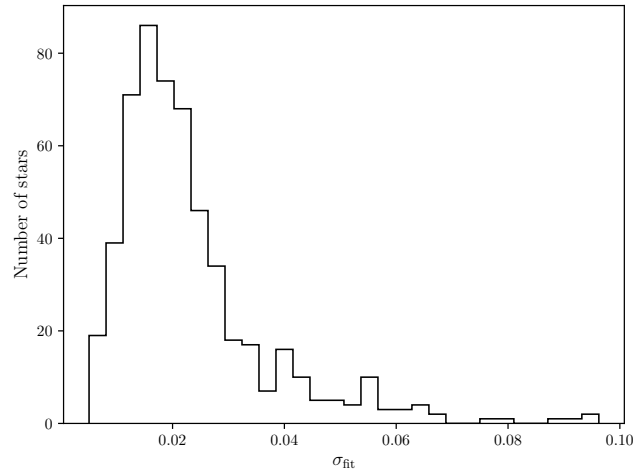


Fig. 2: Histogram of the uncertainty from the Fourier fitting of the 545 Cepheids. (see Eq. 5).

therefore we must keep in mind that binarity and CSE can be a source of scattering in our results.

4. Empirical metallicity relation for short-period Cepheids ($2.5 < P < 6.3$ days)

4.1. Choice of period range and Fourier parameters

In this section we extend quantitatively and qualitatively the metallicity relation for short-periods Cepheids in the V -band following the findings of Klagyivik et al. (2013). In their study they calibrated linear metallicity relations depending on the amplitude ratios R_{21} and R_{31} between 2.5 and 6.3 days. The lower boundary of these relations, defined as $\log P = 0.4$ (≈ 2.5 days), corresponds to a local maxima on the amplitude ratio R_{21} . This can be observed for SMC and LMC Cepheids in I -band in Soszyński et al. (2008, 2010). On the other hand, above $P = 6.3$ days the amplitude ratios are increasingly affected by the pulsation period when they approach the $P_2/P_0 = 0.5$ resonance at 10 days. Thus Klagyivik et al. (2013) focused on Cepheids with

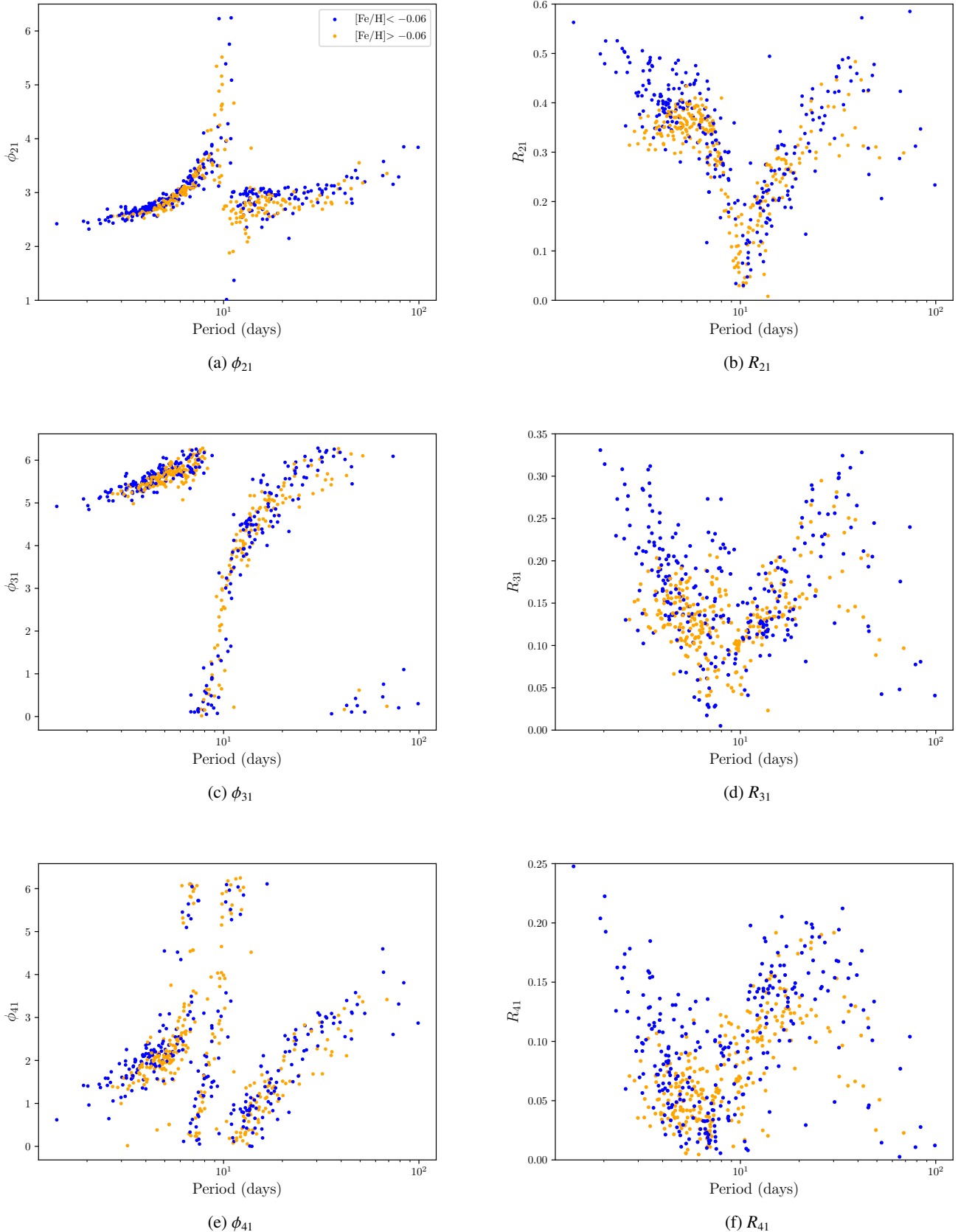


Fig. 3: Fourier parameters of the final sample of the 545 fundamental mode Cepheids in the V -band with spectroscopic metallicities. The different colors refer to metallicity above and below the median of the sample, and are indicated in Figure (a). The peculiar appearance of ϕ_{41} with a break around 7 days was noted by [Simon & Moffett \(1985\)](#); [Kovacs et al. \(1990\)](#). The latter proposed an unknown atmospherical effect since these authors did not observed this break in radial velocity curves.

pulsation period between 2.5 and 6.3 days where the effect of the period is mitigated in particular for R_{21} . This influence of the period can be better observed by displaying Cepheids of the SMC, LMC and our star sample on Figs. 4a and 4b. The Fourier parameters for the SMC and LMC were derived by applying our Fourier decomposition in Sect. 3 to the V -band light curves of classical Cepheids from SMC and LMC from OGLE-IV (Udalski et al. 2015, 2018; Soszyński et al. 2017). From these figures we observe that R_{21} and R_{31} have a smooth linear dependence with the pulsation period.

In the following we choose to fit linear relations based on an unique period interval between 2.5 and 6.3 days. We re-analyze relations based on R_{21} and R_{31} but we also explore others possible linear combinations between the different Fourier coefficients and the pulsation period.

4.2. Fit of the empirical relation with Orthogonal Distance Regression

In this part we fit linear relations based on R_{21} and R_{31} and we also test all possible combinations of Fourier parameters two by two. We considered the following set of Fourier parameters: $R_{21}, R_{31}, R_{41}, \phi_{21}, \phi_{31}, \phi_{41}$. In addition we also take into account the amplitudes A_1 and A_2 and the pulsation period P . We selected the stars for which $\sigma_{\phi_{21}} < 0.05$ to ensure the overall accuracy of the Fourier parameters. We employed Orthogonal Distance Regression (ODR) to take into account both the errors on Fourier parameters and errors on metallicity. We adopted the ODR routine of the SciPy package². To summarize we fit linear relations of the form:

$$[\text{Fe}/\text{H}] = aX + b \quad (6)$$

for R_{21} and R_{31} , and the following form

$$[\text{Fe}/\text{H}] = aX + bY + c \quad (7)$$

for all possible combinations. In order to compare the performance of the different fits to predict accurately and precisely the metallicity, we used a Monte-Carlo Cross-Validation analysis (Xu & Liang 2001). This technique consists in selecting randomly 80% of the data set to fit a relation then to test its ability to estimate the metallicity on the remaining 20% of the sample. This is done by deriving the average difference with the expected $[\text{Fe}/\text{H}]$ values to evaluate the bias, and the precision is estimated by deriving the rms. This procedure is repeated 1000 times and the final fitted coefficients, rms and bias are given by the average of all the results (see Table 2).

From these results, the best fit is achieved by the combination of parameters A_1-A_2 : (see Fig. 5a):

$$[\text{Fe}/\text{H}] = (6.27 \pm 0.53) A_1 + (-11.73 \pm 0.93) A_2 + (-0.59 \pm 0.07) \quad (8)$$

with $\text{rms} = 0.12$ dex. In Fig. 5 we compare this result with a linear relation based on R_{21} only as used by Klagyivik et al. (2013). The relation based on A_1A_2 presents a lower rms than the one based on R_{21} and is in better agreement for lower and higher metallicity range. Thus A_1A_2 relation performs better to recognize the light curves features sensitive to metallicity. In order to further assess the capability of the A_1A_2 relation to estimate the metallicity, we test it in the next section on SMC and LMC sample and compare the results to the literature.

Table 2: Results of the ODR fitting and Monte-Carlo analysis. Only the best results with a final rms below 0.145 dex are presented.

| Param. | rms (dex) | bias (dex) |
|--------------------|-----------|------------|
| A_1-A_2 | 0.123 | -0.001 |
| A_1-R_{21} | 0.126 | -0.000 |
| A_2-R_{21} | 0.128 | -0.000 |
| A_1-R_{41} | 0.129 | -0.001 |
| A_1-A_3 | 0.129 | -0.000 |
| A_1-R_{31} | 0.134 | -0.002 |
| $R_{21}-P$ | 0.134 | -0.000 |
| R_{21} | 0.139 | -0.001 |
| $R_{21}-\phi_{21}$ | 0.139 | -0.001 |
| $R_{31}-R_{21}$ | 0.139 | -0.000 |
| A_2-R_{41} | 0.140 | -0.001 |
| A_3-R_{31} | 0.141 | -0.002 |
| $R_{31}-\phi_{31}$ | 0.141 | -0.002 |
| $R_{31}-\phi_{41}$ | 0.142 | -0.003 |
| $R_{41}-R_{21}$ | 0.142 | -0.002 |
| R_{31} | 0.143 | -0.001 |
| A_2-R_{31} | 0.143 | -0.000 |
| A_3-R_{21} | 0.143 | -0.001 |
| $R_{41}-P$ | 0.143 | -0.000 |
| $R_{21}-\phi_{31}$ | 0.143 | -0.002 |
| $R_{21}-\phi_{41}$ | 0.144 | -0.002 |
| $R_{31}-P$ | 0.144 | -0.000 |
| $R_{31}-\phi_{21}$ | 0.145 | -0.001 |
| $R_{41}-\phi_{41}$ | 0.145 | -0.002 |
| $R_{41}-\phi_{41}$ | 0.145 | -0.002 |

4.3. Testing the empirical relations to the SMC and LMC sample

We retrieved V -band light curves of classical Cepheids from SMC and LMC from OGLE-IV (Udalski et al. 2015, 2018; Soszyński et al. 2017). We first removed the stars which are used in our calibration sample. We then consistently applied the same Fourier decomposition algorithm as established in Sect. 3. We also considered only the stars having more than 30 photometric measurements and with an uncertainty of $\sigma_{\phi_{21}} < 0.05$. We used the Fourier parameters obtained for the Cepheids with a pulsation period between 2.5 and 6.3 days to estimate the metallicity of these stars using the empirical relation previously determined.

The final sample consists of 52 stars from the SMC and 1206 stars from the LMC in the period range 2.5 – 6.3 days. As noted by Soszyński et al. (2008, 2010), there are fewer Cepheids in this period range in the SMC since the distribution of the pulsation periods is dependent on metallicity (Becker et al. 1977; Bono et al. 2000). Indeed metal-poor Cepheids in the SMC have a lower mass cut-off to cross the instability strip than the more metal-rich Cepheids from the LMC. As a result, a majority of short-period Cepheids in the SMC have pulsation period below 2.5 days. The estimated $[\text{Fe}/\text{H}]$ for SMC and LMC Cepheids of our sample are presented in Fig. 6a.

From this histogram we can see that the relation is able to distinguish the populations of the SMC and the LMC. The mean metallicity of the LMC objects is -0.19 ± 0.11 dex that is within the uncertainties in agreement with values found in the literature based on supergiant measurements such as -0.30 ± 0.20 (Russell & Bessell 1989); -0.27 ± 0.15 (Hill et al. 1995); -0.40 ± 0.15 (Andrievsky et al. 2001); -0.34 ± 0.11 (Urbaneja et al. 2017) and -0.41 ± 0.12 (Romaniello et al. 2022) (taking into account

² <https://docs.scipy.org/doc/scipy/reference/odr.html>

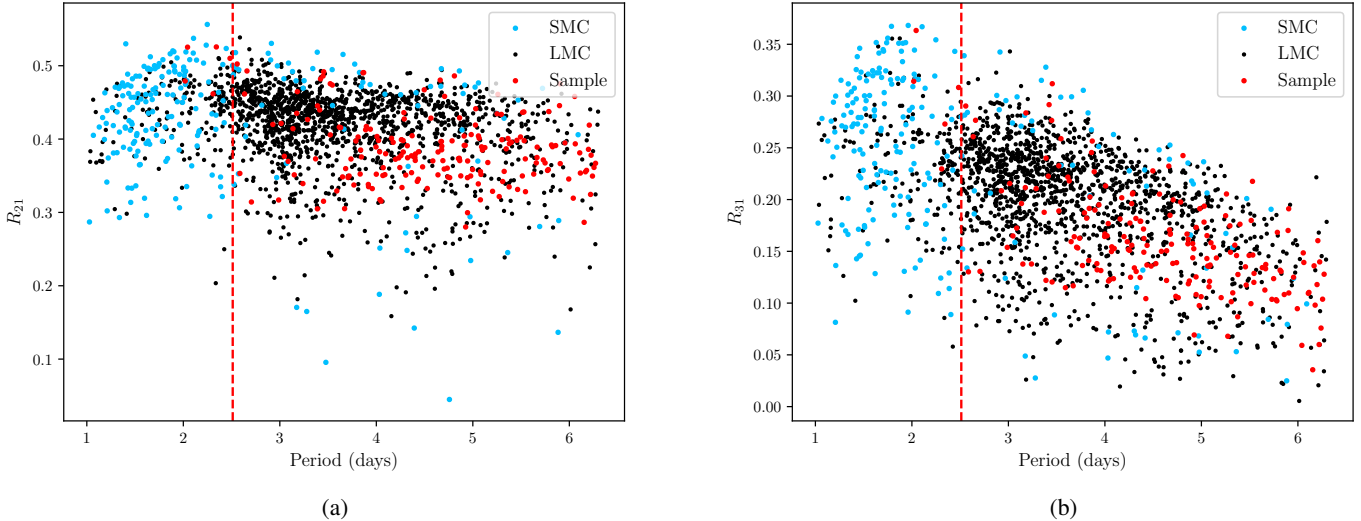


Fig. 4: **(a) and (b)**: Amplitude ratios R_{21} and R_{31} against the pulsation periods for the OGLE SMC, LMC and our star sample is shown for consistency. The dashed vertical line shows the cut at period $P = 2.5$ days.

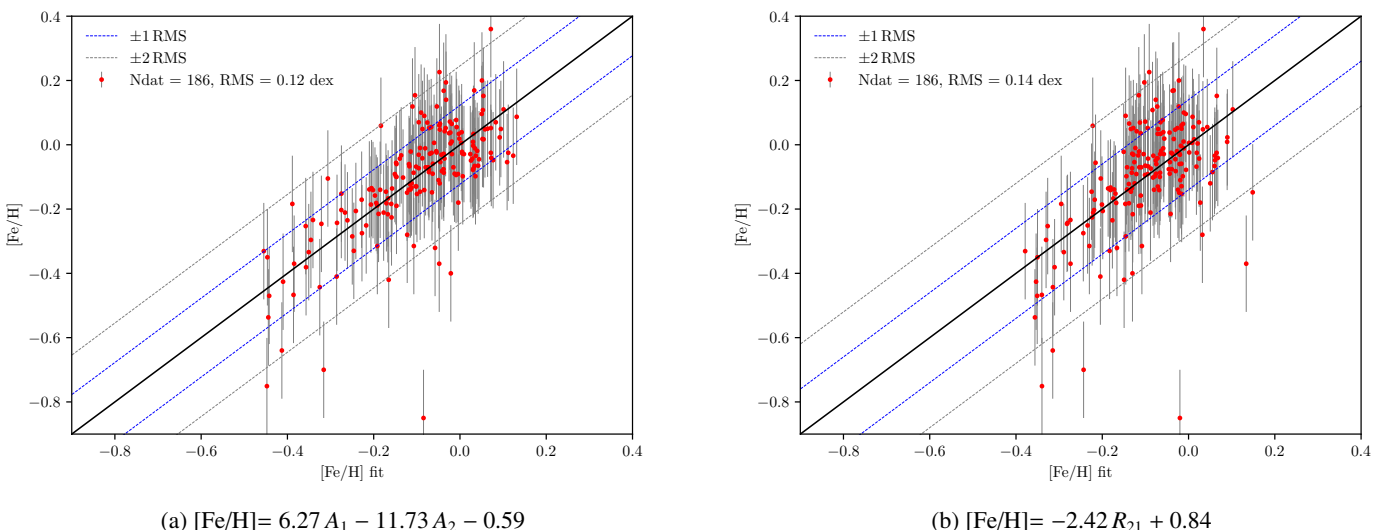


Fig. 5: Comparison of [Fe/H] from the literature and from the fitted empirical relations based on (a) A_{12} and (b) R_{21} for short-period Cepheids. The number of points used in the fit is indicated (N_{dat}) as well as RMS of the fit. The dashed lines represent RMS deviation to guide the eye.

systematic error). Moreover, based on 1206 Cepheids from the LMC, we find a narrow metallicity distribution of the LMC of $\sigma=0.11$ dex (see Fig. 8a). This is in agreement with the findings of Romanillo et al. (2022) who found a dispersion of $\sigma=0.076$ dex from a sample of 89 Cepheids, and the dispersion of 0.069 mag observed in the near-infrared Hubble Space Telescope LMC period–luminosity relation (Riess et al. 2019).

However, this relation seems to overestimate the metallicity for the SMC with a mean $[Fe/H]$ of -0.30 ± 0.14 dex. In the case of the SMC the overestimation is significantly higher than spectroscopic measurements of 14 long-period SMC Cepheids giving $[Fe/H] = -0.75 \pm 0.08$ dex (Romaniello et al. 2008) while it is in marginal agreement within about 1σ with others mean metallicity estimation based on giant and supergiant stars: $-0.65 \pm$

0.20 dex (Russell & Bessell 1989) (8 stars); -0.62 ± 0.14 dex, (Trundle et al. 2007) (5 stars); and B stars with -0.70 ± 0.20 dex (Korn et al. 2000) (6 stars) (see Fig. 8b). We note however that these studies are based on few stars only, whereas we derived the metallicity from a larger sample of 52 Cepheids.

This overestimation of [Fe/H] could be attributed to the poor coverage of the low metallicity regime in our calibration sample (4 stars only lower than -0.6 dex). Moreover, a linear relation might not be valid at low metallicity as noted by [Klagyivik et al. \(2013\)](#). It is also possible that the SMC testing sample is statistically not large enough to properly determine the mean and the dispersion of the metallicity distribution. A more significant result for the mean metallicity of the SMC Cepheids will be ob-

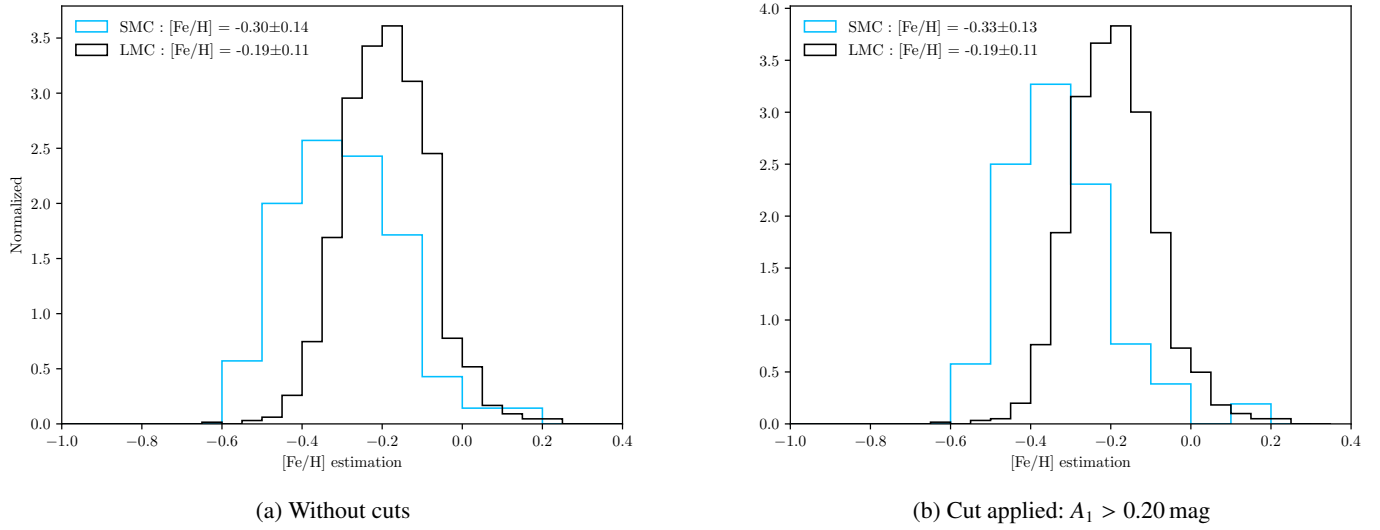


Fig. 6: Normalized histograms (unit area) of the metallicity estimation of the SMC (blue) (52 stars in (a)) and LMC (black) (1206 stars in (a)) Classical Cepheids from the relations established in Sect. 4.2 for short-period Cepheids. The mean metallicity of these distributions and the standard deviation around the mean are indicated in the legend.

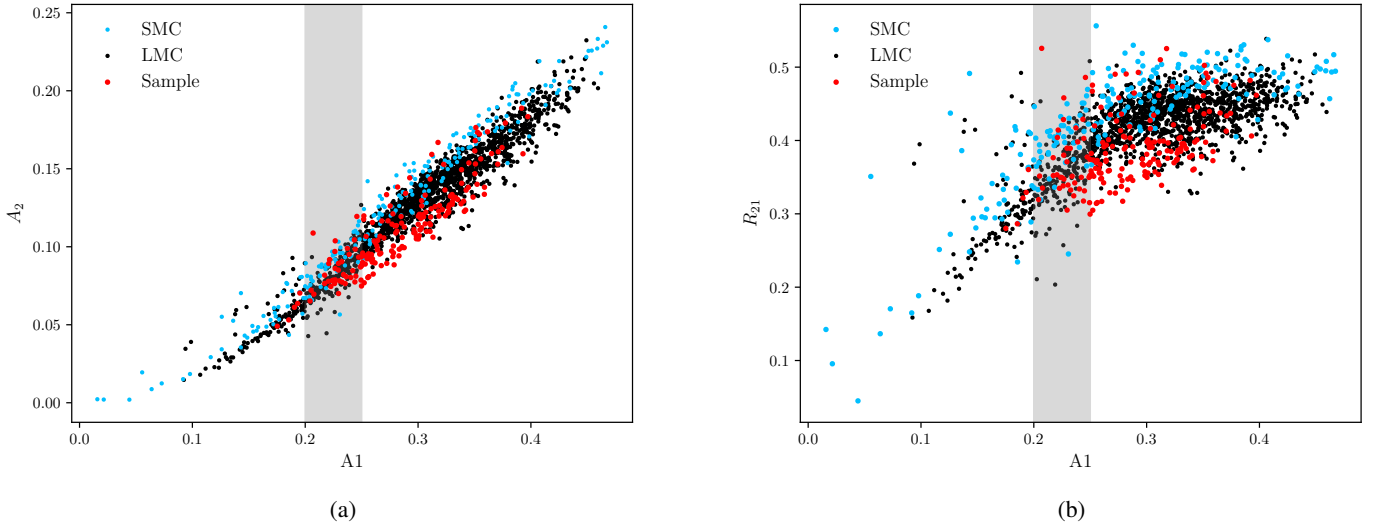


Fig. 7: (a) and (b): Relations between the first and second harmonic A_1 and A_2 used in the empirical relation for short-period Cepheids between 2.5 and 6.3 days. The vertical strip represent the values of A_1 where a cut can be applied (for A_1 between 0.20 and 0.25 mag) to remove the stars of low amplitudes to mitigate the effect of location inside the instability strip.

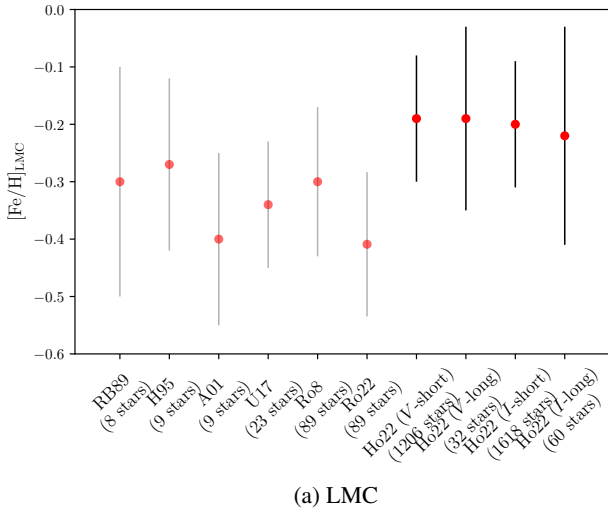
tained from I -band OGLE-IV light curves in Sect. 6, which are available for a much larger sample of stars.

Last, a part of the spread observed in these distributions may be caused by the influence of other physical effects than metallicity such as the location in the instability strip. Indeed the amplitude of Cepheids, and their amplitude ratios, depend on the location in the instability strip (Sandage & Tamman 1971; Sandage et al. 2004). The amplitudes are higher close to the blue edge and decrease toward the red edge as the damping from convection increases.

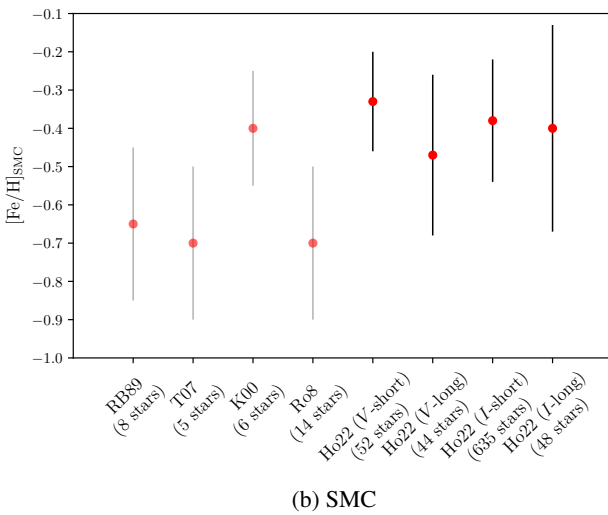
In order to illustrate this effect we displayed the LMC Cepheids with pulsation period between 2.5 and 6.3 days in the instability strip in Fig. 9. We used Wesenheit index $W_{I,V}$ as a

function of the color $m_V - m_I$ corrected by extinction (Skowron et al. 2021). From this figure we clearly see that lower amplitude stars with $A_1 < 0.25$ mag are concentrated at the red edge of the strip. Hence, the stars which are closer to the blue or the red edge have different amplitudes, and thus the empirical metallicity estimation based on $A_1 A_2$ could be affected. The relation between A_1 and A_2 can be seen on Fig. 7. From this figure, we observe that the relation between A_1 and A_2 is not linear anymore below about $A_1 = 0.20$ -0.25 mag. On the contrary, above $A_1 = 0.20$ -0.25 mag the amplitude ratio R_{21} saturates to about 0.45 and most of the dispersion is attributed to a metallicity effect.

Thus, we propose to cut out from the sample all stars with $A_1 < 0.20$ mag in order to mitigate the effect due to the loca-



(a) LMC



(b) SMC

Fig. 8: Comparison of mean [Fe/H] derived from the literature (grey bars) and from [Fe/H] estimations presented in this paper (black bars). For each reference the number of stars used to derive the mean is indicated. For details see Sect. 4.3 for short-period Cepheids in V -band, 5.2 for long-period Cepheids in V -band, and Sect. 6.2 for I -band relation.

tion inside the instability strip. This limit is defined only approximately to show the influence on the derived metallicity. A more restrictive cut at $A_1=0.25$ mag can be applied if the objective is to favorize the precision of individual measurement over the statistical size of the sample. By removing stars for which $A_1 < 0.20$ mag, we obtain a slightly better distinction between the SMC and LMC as we can see on Fig. 6b. However the mean metallicity and the deviation from the mean are not significantly affected because the majority of the stars are above this threshold. Although the mean of the distribution remains unchanged, applying this cut to the empirical relation based on A_1 and A_2 prevents contamination by stars with intrinsically low pulsation amplitudes and stars that would be significantly blended by a companion in the visible. Therefore we recommend to apply this cut when using the empirical relations based on A_1 , A_2 . We also note that some stars of our calibrating sample are slightly below this threshold. However removing them does not change the result of the fit and we decided to keep them in the calibration set.

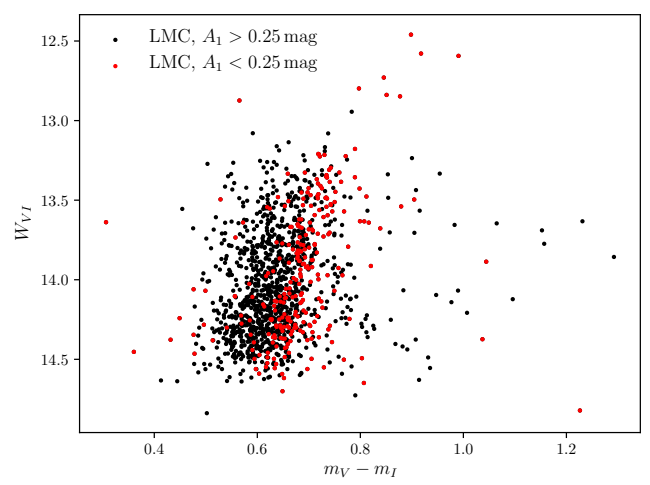


Fig. 9: Luminosity-color diagram of LMC Cepheids between 2.5 and 6.3 days using V - and I -band magnitudes.

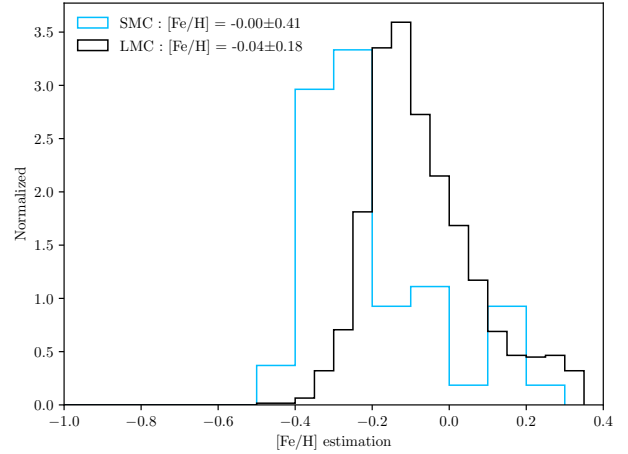


Fig. 10: V -band metallicity estimation using (Klagyivik et al. 2013)

We discuss the use of these cuts in Sect. 7. Finally, we apply the relation obtained by Klagyivik et al. (2013) in the V -band for the same period range (see Fig. 10). As discussed in the previous section, relation based on R_{21} and R_{31} overfit the metallicity around 0 dex and thus are not able to generalize for low and metal-rich stars. For that reason, the distributions observed on Fig. 10 are shifted by about +0.2 dex compared to our results, in agreement with verification made by Clementini et al. (2019).

5. Empirical metallicity relation for long-period Cepheids ($12 < P < 40$ days)

5.1. Fit of the empirical relation with ODR technique

Finding a correlation between the Fourier parameters and the metallicity for long-period Cepheids is a challenge mainly because there are fewer spectroscopic observations of metal-poor long-period Cepheids. Moreover these stars are colder in average

and thus the convection affects the photosphere and the resulting light curves. However, the recent spectroscopic metallicities obtained by Romaniello et al. (2022) for 89 metal-poor Cepheids from the LMC allow for the first time to compare with metal-rich Cepheids from the Milky Way. In the case of long-period Cepheids between 10 and 40 days, a visual inspection of Fig. 3a shows that there is a concentration of metal-poor Cepheids at the top of the ϕ_{21} branch, while metal-rich Cepheids seem to have lower values. Several evidences in the literature are supporting this observation. Observationally this effect was noticed by Pont et al. (2001) who studied metal-poor Cepheids in the outer part of the MW. Theoretically, this phenomenon was reproduced by Buchler (1997, 1998) who used radiative pulsation models. However it could not be compared to observations at that time. The amplitudes of long-period Cepheids may also be affected by the metallicity. The models computed by Bono et al. (2000) indicate that metal-rich Cepheids with a pulsation period of 10–30 days pulsate with larger peak-to-peak amplitudes than metal-poor ones. This estimation was observationally supported by Majaess et al. (2013) who found that metal-rich long-period Cepheids display larger V-band amplitudes than their counterparts in very metal-poor galaxies.

In order to assess quantitatively whether or not the shape of the V-band light curves depends on the metallicity, we followed the method of the previous section by fitting several possible combinations of Fourier parameters. We considered the following set of Fourier parameters: $A_1, R_{21}, R_{31}, R_{41}, \phi_{21}, \phi_{31}, \phi_{41}$, as well as the pulsation period P , and $[\text{Fe}/\text{H}]$. We selected the Cepheids with pulsation periods from 12 days and no longer than 40 days. Indeed, our data set contains too few stars above $P=40$ days, and longer periods could behave differently, as we can guess from Fig. 3, or be affected by possible resonance effects (Antonello 1998). We also selected Cepheids with ϕ_{21} between 2.5 and 3.3 to remove the stars which could be affected by the resonance around 10 days and with $\sigma_{\phi_{21}} < 0.05$. Our final data set consists of 120 long-period Cepheids.

As in the case of short-periods we employed ODR technique to take into account errors on both Fourier parameters and metallicity. We tested all combinations of parameters two by two, and we also tested all possible combinations three by three. We estimated the rms and the bias of this relation following the method used in the previous section. We selected randomly 80% of the sample to fit a relation and tested it on the 20% remaining, and repeated the procedure 1000 times. We found a significantly better result in the case of the triplet $A_1 - R_{41} - \phi_{21}$. The histograms of their distribution are presented in Fig. 11. From these figures, we can see that R_{41} and ϕ_{21} decrease with larger metallicity while the amplitude of the harmonic A_1 seem to increase with metallicity. The $[\text{Fe}/\text{H}]$ from the literature and $[\text{Fe}/\text{H}]$ obtained from the fit is presented in Fig. 12. We obtained the following equation:

$$\begin{aligned} [\text{Fe}/\text{H}] = & (3.94 \pm 0.46) A_1 + (-5.80 \pm 0.85) R_{41} \\ & + (-0.93 \pm 0.16) \phi_{21} + (1.67 \pm 0.39) \end{aligned} \quad (9)$$

We find $\text{rms}= 0.25$ dex for estimating individual metallicity, and the relation is accurate with a bias of 0.001 dex.

5.2. Testing the empirical relations to the SMC and LMC sample

We followed the method employed in Sect. 4.3 to check the validity of this empirical relation on a sample of SMC and LMC stars. The Cepheids of the LMC were retrieved from OGLE-IV.

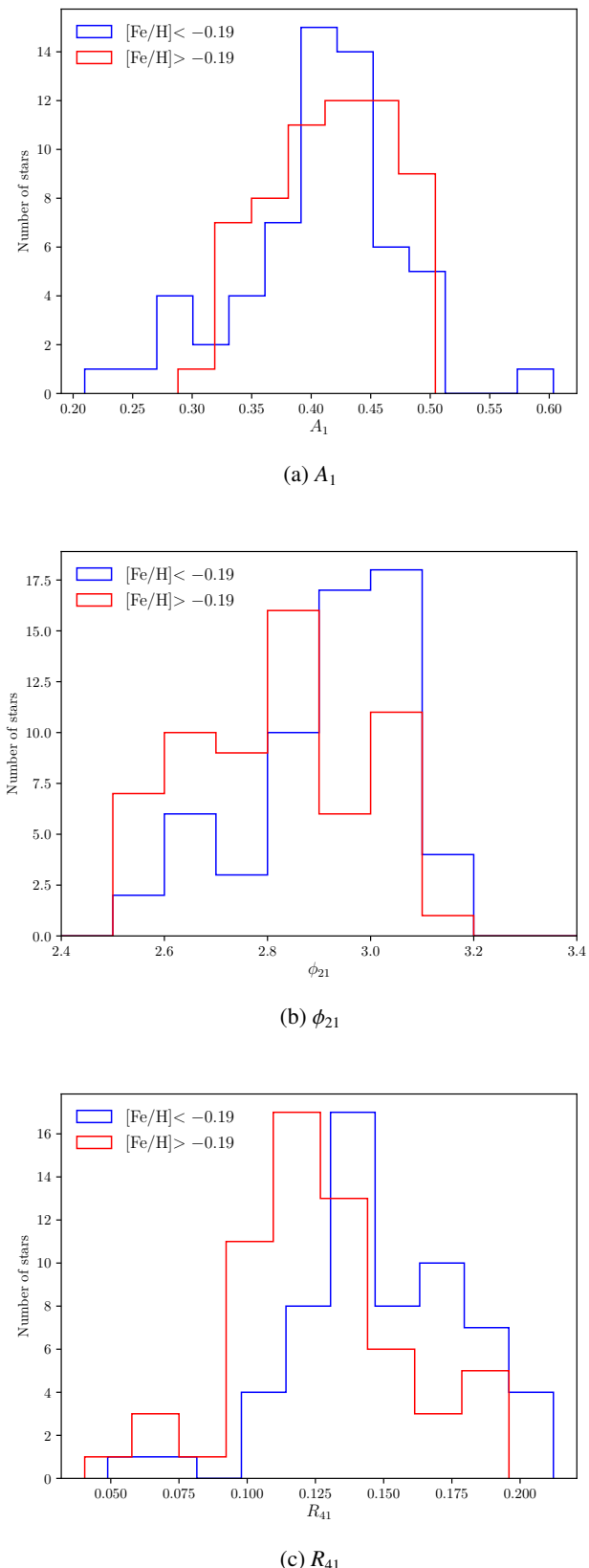


Fig. 11: Histogram of A_1 , ϕ_{21} and R_{41} for Cepheids with pulsation period between 12 and 40 days for metal-rich ($[\text{Fe}/\text{H}] > -0.19$) and metal-poor ($[\text{Fe}/\text{H}] < -0.19$) stars. $[\text{Fe}/\text{H}] = -0.19$ dex represents the median of the metallicity sample of long-period Cepheids.

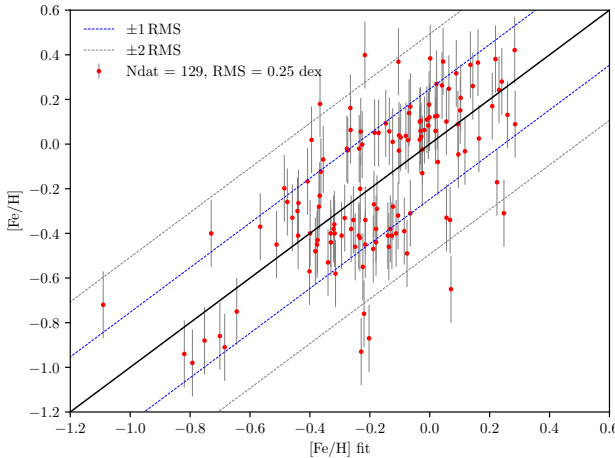


Fig. 12: Comparison of the fitted $[Fe/H]$ with $[Fe/H]$ from literature for long-period Cepheids between 12 and 40 days.

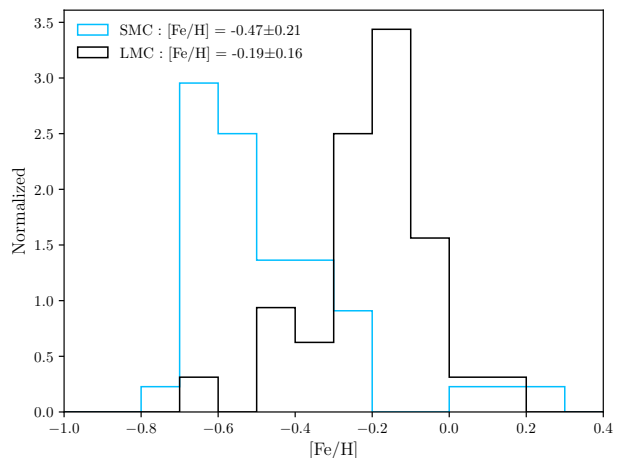


Fig. 13: Normalized histogram (unit area) for estimated metallicity of SMC and LMC long-period Cepheids (44 and 32 stars respectively) based on empirical relation in the V -band.

However the long-period Cepheids of the SMC are in average poorly sampled in OGLE-IV. Thus we rather compiled the light curves from OGLE III for Cepheids in the SMC. We applied Fourier decomposition from Sect. 3 and we removed the stars with $\sigma_{\phi_{21}} > 0.05$ and those which are already used for the calibration. We selected Cepheids with ϕ_{21} between 2.5 and 3.3 consistently to the calibration sample. The final sample consists of 44 stars from the SMC and 32 star from the LMC. The result is presented in Fig. 13. As it can be seen from this figure, the empirical relations for long-period Cepheids are able to nicely distinguish between SMC and LMC populations of Cepheids. The mean of the distributions are -0.19 ± 0.16 and -0.47 ± 0.21 dex for LMC and SMC respectively. While the tested sample is relatively small, the mean distributions are in agreement within 1-sigma with the mean values from the literature presented in Sect. 4.3 (see Fig. 8). As a conclusion, the empirical relation based on Fourier parameters $A_1 - R_{41} - \phi_{21}$ performs well to derive accurately the mean metallicity for a sample of long-period Cepheids between 12 and 40 days. The estimation of individual metallicity however, has to be associated with an uncertainty of ± 0.25 dex.

In the next section, we establish empirical relations in the I -band and we further test them owing to the larger sample of stars with well sampled light-curves in I -band available in OGLE-IV.

parameters in V - and I -band to transform V -band relations into the I -band. Interrelations are linear relations existing between the same Fourier parameters in different bands. These interrelation can be used to convert the V -bands Fourier parameters into the I -band and inversely (Hendry et al. 1999; Kanbur et al. 2000; Ngeow et al. 2003). Moreover Ngeow et al. (2003) emphasized that the change in metallicity does not affect significantly the interrelations between the Fourier coefficient in different bands. Hence these interrelations are convenient to apply in the case of Cepheids. This seems to be more difficult in the case of RR Lyrae stars for which interrelations are affected by metallicity (Skowron et al. 2016). Thus, our empirical relations Eqs. 8 and 9 can be converted to the I -band.

We choose to re-calibrate interrelations in V and I -bands using the sample of SMC and LMC OGLE data. In particular we focus on the relevant Fourier parameters needed for the conversion, within the specific period ranges adopted by the empirical relations. For the short-period Cepheids between 2.5 and 6.3 days, we crossed-matched the stars in common between OGLE LMC for V and I -band (1342 stars) and we fitted linear (ODR) relations between $A_1(V)$ and $A_1(I)$, as well as $A_2(V)$ and $A_2(I)$ amplitudes (see Fig. A.1a). We obtain the following interrelations:

$$A_1(V) = (1.7035 \pm 0.0066) A_1(I) + (-0.0023 \pm 0.0011) \quad (10)$$

$$A_2(V) = (1.7011 \pm 0.0046) A_2(I) + (-0.0002 \pm 0.0003). \quad (11)$$

$$(12)$$

For the long-period Cepheids between 12 and 40 days, we used both SMC and LMC OGLE data to maximize the number of stars for the calibration (120 stars in total, see Fig. A.2) to obtain the following interrelations:

$$A_1(V) = (1.6332 \pm 0.0303) A_1(I) + (0.0060 \pm 0.0070) \quad (13)$$

$$R_{41}(V) = (1.0399 \pm 0.0239) R_{41}(I) + (-0.0056 \pm 0.0034) \quad (14)$$

$$\phi_{21}(V) = (0.8389 \pm 0.0184) \phi_{21}(I) + (0.0693 \pm 0.0633) \quad (15)$$

$$(16)$$

6. Empirical relations in the I-band using Fourier interrelations

6.1. Conversion using interrelations

The near-infrared I -band is particularly interesting for observing obscured galactic or extragalactic Cepheids since it is less affected by extinction than in the visible. Therefore empirical calibrations in the I -band could be useful for studying the effect on the metallicity on the PL relation and also for galactic archeology. However it is more difficult to calibrate this relation in the I -band because there are less I -band light curves available with a good sampling in the MW for short and long-period Cepheids. Although empirical relations remain to be calibrated for the I -band, we can use interrelations between Fourier pa-

Then, there are two equivalent strategies to convert the V -band metallicity relations into the I -band using interrelations. One possibility is to convert the Fourier parameters of our calibrating sample and then to re-process the fit as done in the V -band in the last sections. The other idea is to directly convert the empirical V -band relations. We applied the latter possibility in the following, by substituting the precedent relation into V -band empirical relations. For the short-period Cepheids we obtain:

$$[\text{Fe}/\text{H}] = (10.69 \pm 0.90)A_1 + (-19.96 \pm 1.58)A_2 + (-0.60 \pm 0.07) \quad (17)$$

This relation is valid for P between 2.5 and 6.3 days. The cuts that can be applied for $A_1(I)$ are between 0.12 and 0.16 mag (corresponding to $A_1(V)$ between 0.20 and 0.25 mag) to mitigate the effect of location of the star inside the instability strip. For the long-period Cepheids, we obtain:

$$[\text{Fe}/\text{H}] = (6.43 \pm 0.76)A_1 + (-6.03 \pm 0.89)R_{41} + (-0.77 \pm 0.13)\phi_{21} + (1.66 \pm 0.40) \quad (18)$$

with $\phi_{21}(I)$ between 2.9 and 3.85 (corresponding to $\phi_{21}(V)$ between 2.5 and 3.3).

As a first check, it is important to assess if these relations in the I -band are consistent within the uncertainties with empirical relation in the V -band. In order to compare these relations, we consistently applied the empirical relations for the stars in common. The result is shown in Fig. 14a. Applying a linear fit to the data we found that $[\text{Fe}/\text{H}]_V = 1.01(\pm 0.01)[\text{Fe}/\text{H}]_I + 0.005(\pm 0.002)$. The resulting $[\text{Fe}/\text{H}]$ estimation in the I -band is also consistent with the V -band within 0 ± 0.04 dex that is below the rms of 0.12 dex for V -band empirical relation.

We repeat the procedure for the long-period Cepheids (see Fig. 14b). Applying a linear fit we obtain $[\text{Fe}/\text{H}]_V = 1.02(\pm 0.03)[\text{Fe}/\text{H}]_I + 0.001(\pm 0.014)$ which is also consistent with colinearity and no offset. The resulting estimation in the I -band is in agreement in the V -band within 0 ± 0.10 dex that is below the V -band rms of 0.25 dex.

6.2. Testing the empirical relations to MW, SMC and LMC OGLE-IV sample

In order to further test the performance of the I -band relation we first verify the metallicity distribution obtained for the MW, SMC and LMC. Similarly to previous sections, we apply these empirical relations to OGLE-IV light curves in the I -band to derive the metallicity of SMC, LMC and MW Cepheids. For the MW Cepheids we gathered the light curves from the Galactic Disk and the Bulge.

In case of short period Cepheids we cut out from the sample all stars with $A_1 < 0.12$ mag (corresponding to $A_1 < 0.20$ mag in V -band). This was done to mitigate the effect of the location within the instability strip. The testing sample is thus composed of 394 stars from the MW, 635 stars in the SMC and 1618 stars in the LMC. Results are presented in Fig. 15a. We can see that the I -band relation is able to distinguish the three populations of stars. For each distribution we derived a mean metallicity for the SMC: -0.38 ± 0.17 dex, LMC: -0.20 ± 0.11 dex and MW: -0.13 ± 0.18 dex which are in agreement with mean values from the literature. As a comparison, we also apply empirical relation from Klagyivik et al. (2013) based on R_{21} in the I -band in the same period range (see Fig. 15b). As noticed by Clementini

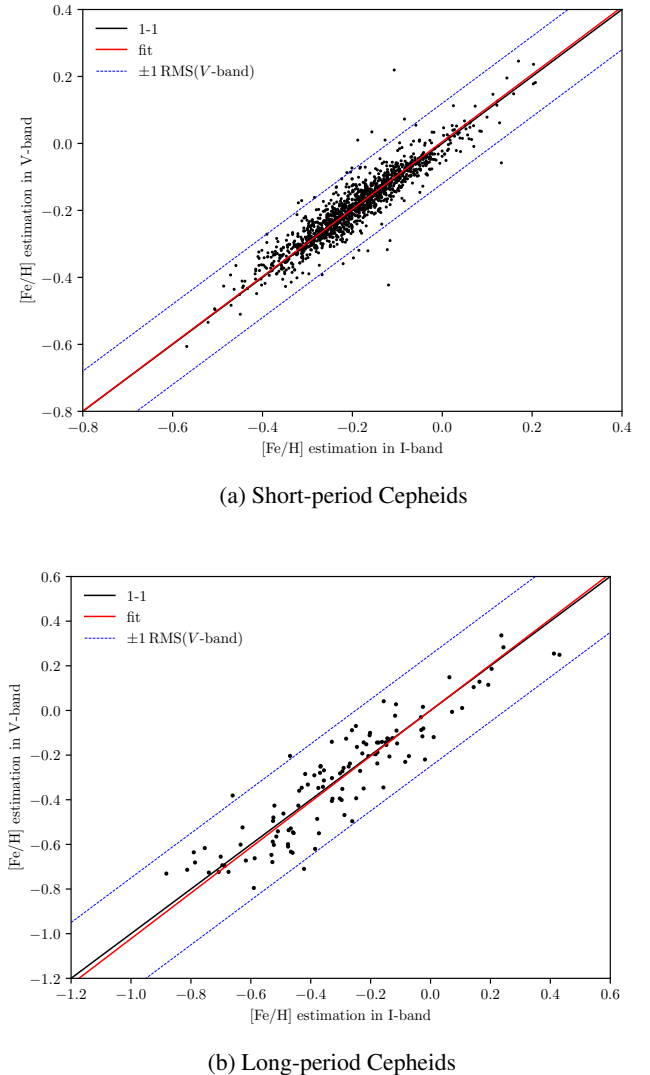


Fig. 14: Comparison of metallicities derived with both V -band and I -band empirical relations. Black line indicate a one-to-one correspondence and the red thick line is the fit between the two bands. Blue dashed lines represent the rms of the empirical relation in the V -band.

et al. (2019) this relation overestimates the metallicities by about $+0.2$ dex. This problem disappears when using the relation calibrated in this paper.

For the long-period Cepheids the testing sample is composed of 92 stars from the MW, 60 stars in the SMC and 48 stars in the LMC. The empirical relation performs well to obtain the distribution of the expected metallicity for these galaxies (see Fig. 15c), although the sample of star is much smaller than the short-periods. For each distribution we derived a mean metallicity for the SMC: -0.40 ± 0.27 dex and LMC: -0.22 ± 0.19 dex which are in agreement within 1σ with both mean values from literature and our previous result for the short-period Cepheids. For the MW we derived a mean $[\text{Fe}/\text{H}]$ of $+0.22 \pm 0.30$ dex, which have a large spread as observed for short-period Cepheids. We show in the next section that this effect is due to the metallicity gradient in the Galaxy.

6.3. Mapping the metallicity distribution in the MW, SMC and the LMC

In this part we use our metallicity estimations for the fundamental mode Cepheids in the MW, SMC and LMC and we retrieve their coordinates from 3D maps available in the literature. Then, we test if our relations are precise enough to obtain information of the metallicity gradient in these galaxies for potential applications in galactic archeology.

For stars with metallicity estimation of the MW Cepheids, we cross-match OGLE-IV sample in the I -band with the stars from galactic 3D map from Skowron et al. (2019). For the literature sample we cross-match the 472 fundamental Cepheids of our metallicity sample (see Table 1) with the map from Skowron et al. (2019) and Kovtyukh et al. (2022a). As a result we obtain 868 stars in the MW, with 460 having metallicity from the literature and 408 others estimated by our relations. The galactic coordinates and the distance of these stars available allow to plot the metallicity distribution in the MW (see Fig. 16a). By adopting a Sun galactocentric distance of 8.1 ± 0.1 kpc (Bobylev & Bakjikova 2021) we can also display the metallicity as a function of the galactocentric radius R_G (see Fig. 16b). From these distributions we observe that spectroscopic observations are mostly given in the vicinity of the Sun while the OGLE sample covers farther distances. This is due to the sensitivity of spectroscopy which limits the observation to the closest (bright) stars while it saturates OGLE detectors. We also note that for galactocentric distances below about 7 kpc, almost only long-periods Cepheids are observed. The higher level of interstellar extinction at these distances toward the galactic center likely limits the observation of faint short-period Cepheids. We fitted a straight line for three different samples, taking into account the uncertainty on the galactocentric distance and the metallicity. For the sample of the spectroscopic metallicity that we gathered from the literature (460 stars) we obtain:

$$[\text{Fe}/\text{H}] = (-0.0598 \pm 0.0018) R_G + (0.5263 \pm 0.01848). \quad (19)$$

For the metallicity estimations from I -band light curves only (408 stars):

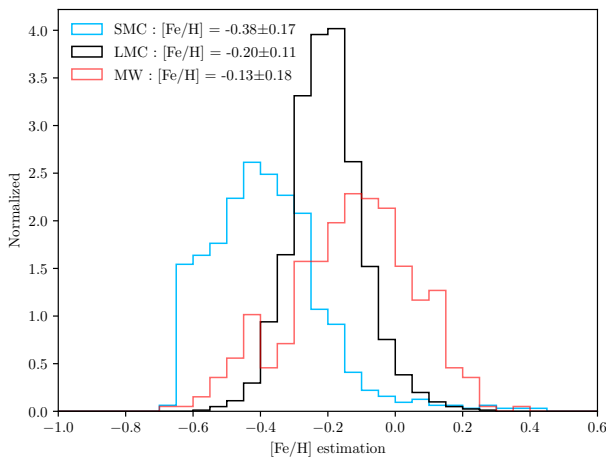
$$[\text{Fe}/\text{H}] = (-0.0562 \pm 0.0023) R_G + (0.5514 \pm 0.0280). \quad (20)$$

And the sample with both literature and estimations (868 stars):

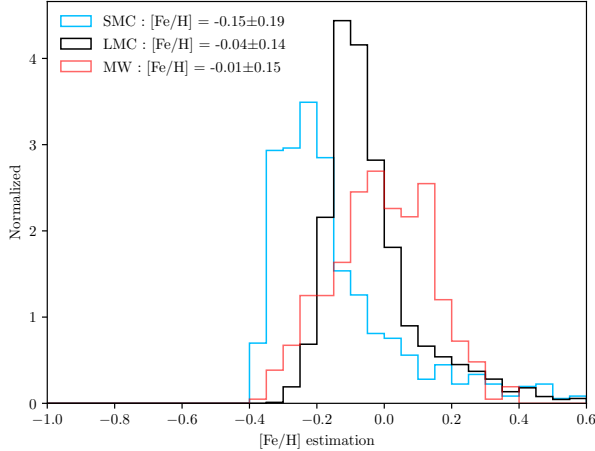
$$[\text{Fe}/\text{H}] = (-0.0556 \pm 0.0015) R_G + (0.5156 \pm 0.0163). \quad (21)$$

The relation obtained only from the literature sample is in agreement with the precedent results in the near- and far-side of the disk (Genovali et al. 2014; Luck 2018; Minniti et al. 2020) which provide a gradient between -0.05 and -0.06 dex kpc^{-1} . The empirical relation in the I -band performs well to reconstruct a metallicity gradient in the galaxy of the same order of magnitude as in literature with -0.056 dex kpc^{-1} . It is difficult to properly compare the slope obtained from the empirical relations with the results from the literature. Indeed, the OGLE-IV MW sample encompasses regions which are different from the spectroscopic observations, in both radial and azimuthal angle (see small vs big points in Fig. 16a, a larger figure is presented in the annex for visualization Fig. B.1). Our result suggests that empirical relations in V and I bands are useful tools to obtain informations on the metallicity distribution in the Galaxy particularly in regions which are not accessible by spectroscopy up to 20 kpc from the Sun.

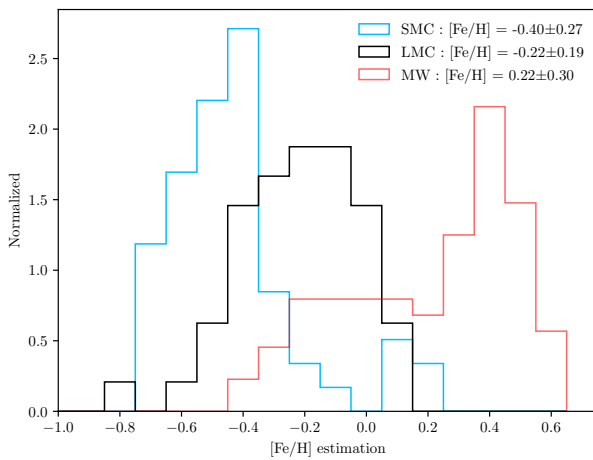
We also mapped the SMC and the LMC with our metallicity estimation by using the distances and coordinates of Cepheids



(a) I -band metallicity estimation for short-period Cepheids



(b) I -band metallicity estimation (Klagyivik et al. 2013)



(c) I -band metallicity estimation for long-period Cepheids

Fig. 15: Normalized histograms (unit area) of the metallicity estimation of the SMC (blue) and LMC (black) and MW(GD+BULGE) (red) fundamental Cepheids from the shape of the I -band light curve. For short-periods, SMC, LMC and MW(GD+BULGE) : 635, 1618 and 394 stars respectively. For long-periods, SMC, LMC and MW(GD+BULGE) : 48, 60 and 92 stars respectively.

for the SMC and the LMC (Jacyszyn-Dobrzeniecka et al. 2016) (see Figs. 16e and 16c). After cross-matching we obtained 1561 LMC Cepheids and 674 SMC Cepheids with estimated metallicities. Interestingly, we observe higher metallicities in the LMC bar in the LMC map. We also displayed the metallicity as a function of the galactocentric radius (see Figs. 16f and 16d). Since the distribution of the relatively young population of Cepheids is highly non-uniform contrary to older RR Lyrae for example, displaying the metallicity as a function of the galactocentric radius has the only interest to show non-correlation. In order to observe the metallicity gradient for the SMC and the LMC we followed the method described by Skowron et al. (2016) in the case of RR Lyrae stars. For each bin of 1 kpc we derived the median of the metallicity and we derived the standard deviation (see red crosses and dashed lines in Figs. 16d and 16f)). We find similar results as obtained from Skowron et al. (2016) with an apparent decrease of the median metallicity within 4 kpc from the center in the case of the LMC, while no slope is visible in the SMC. Because of the large scatter of the metallicity gradient observed in these galaxies, as observed similarly for RR Lyrae metallicities (Skowron et al. 2016), our findings on the slope remain qualitative only.

As a conclusion our metallicity estimates are able not only to reproduce the peak of metallicity distributions of galaxies as shown in the previous sections, but they can also reproduce the trends of the metallicity gradient in MW. Therefore, the empirical relations calibrated in this paper can be applied for further studies in galactic archeology.

6.4. A quantitative test: Investigation of systematics using Cepheid-cluster pairs

A relevant quantitative test can be performed by comparing Cepheid metallicity with open cluster metallicity in order to investigate possible systematics. A recent paper investigated the open-cluster (OC) housing MW classical Cepheids (Hao et al. 2022) from Gaia DR3 release. They identified 39 probable open cluster-Cepheid pairs. Most of these Cepheids-OC pairs are in the Sun's vicinity and thus are already part of our calibrating sample. For this reason this MW sample cannot be independently used to check systematics in our relations.

Alternatively we can use OC-Cepheid pairs in the LMC or SMC for performing those tests at lower metallicity. This is also interesting since we expect systematics at the more metal-poor regime of our empirical relations. The two massive LMC clusters NGC 1866 and NGC 2031 have the largest known Cepheid population (Welch & Stetson 1993; Testa et al. 2007; Musella et al. 2016). In NGC 1866 we found light-curves for five Cepheids from OGLE. Among these stars three are already part of our calibration sample (Lemasle et al. 2017) and one has a low amplitude (LMC-CEP-3731, $A_1(I) < 0.12$ mag). Thus we have only estimation for LMC-CEP-3721 with $[Fe/H] = -0.14 \pm 0.12$ dex. Although one photometric estimation is not enough to compare, this measurement seems to be biased by at least $+0.2$ dex compared to various NGC 1866 spectroscopic measurements (see Lemasle et al. 2017). We note however that light-curves for others Cepheids in NGC 1866 might be obtained by combining photometry from different instruments (see Musella et al. 2016).

In NGC 2031 we found five others Cepheids with light-curves available from OGLE, and we determined the following metallicities using our empirical relations: OGLE LMC-CEP-2377 (-0.08 dex); LMC-CEP-2371 (0.03 dex); LMC-CEP-2391 (-0.17 dex); LMC-CEP-2385 (-0.18 dex); LMC-CEP-2375 (-0.27 dex), which yields the average $[Fe/H]$ of $-0.13 \pm$

0.10 dex. To our knowledge, the only spectroscopic metallicity of NGC 2031 available is -0.52 ± 0.21 dex (Dirsch et al. 2000). On the other hand, Chilingarian & Asa'd (2018) obtained $[Fe/H] = -0.14 \pm 0.02$ dex from fitting of integrated optical spectra. They also find that the metallicity of NGC 2031 is in excellent agreement with age-metallicity relation and models of LMC chemical enrichment history. Our empirical value is discrepant with the spectroscopic measurement but is in agreement with the second one. Hence, it is unclear whether or not our estimations are affected by systematics based on this cluster.

In the case of the SMC, the cluster NGC 330 is the brightest young cluster which also hosts several Cepheids (Sebo & Wood 1994). Among the classical Cepheids in NGC 330 our empirical relation is valid (period and amplitude range, light-curve quality) only for OGLE-SMC-CEP-2634 and we derived $[Fe/H] = -0.61 \pm 0.12$ dex. Several metallicity estimates obtained from different methods are available for NGC 330 which also complicates the comparison. Using high-resolution spectroscopy Hill (1999) found that NGC 330 is metal-deficient compared to the field stars (-0.82 ± 0.11 dex vs -0.69 ± 0.10 dex). More recently, Narloch et al. (2021) found $-0.98 \pm 0.08(\text{stat.}) \pm 0.10(\text{syst.})$ dex from stromgren photometry. Based on these values, our empirical estimation might be biased by about $+0.2$ dex or more at low metallicity. However we cannot firmly conclude since we compare with only one empirical estimation.

As a conclusion, it is difficult at this stage to check potential systematics in empirical relations by comparison with cluster metallicity. Clusters host generally one Cepheid (see Dinnbier et al. (2022) and reference therein) thus the identification of a significant number of OC-Cepheid pair in MW and beyond, together with reliable metallicities measurements are necessary to further investigate systematics.

7. Discussion

In this paper we provided new empirical relations for estimating the metallicity for short and long-period Cepheids in the V -band, and we used interrelation from the literature between V and I bands to convert these relations into the I -band. For individual metallicity determination, uncertainties of $\sigma=0.12$ dex and $\sigma=0.25$ dex have to be attributed for short- and long-period Cepheids respectively. As noted by Cacciari et al. (2005) in the case of RR Lyrae stars, photometric formulae are good tools to study mean metallicities in a population, but are less precise to determine metallicity of individual stars. Hence our empirical relations can be more adapted to characterise large population of Cepheids. Finally, we also tested the relations in the I -band to map the metallicity distribution of MW, SMC and LMC and we were able to recover the metallicity gradient consistent with the literature. However, our calibration sample lacks spectroscopic measurements of metal-poor Cepheids below about -0.5 dex especially for the short-periods. Thus our relation has to be used with caution when measuring metallicity of metal-poor galaxies or at the outer most region of the Milky Way. On the other hand, the calibration of such empirical relations can be still improved in the future. A way to improve the calibration would be to obtain an homogeneous data set for spectroscopic metallicity, determined with a single method which mitigates the systematics measurements (da Silva et al. 2022). Homogeneous sample of light curves in both V and I -bands will be also helpful. In this paper we also assumed simple linear relation between the Fourier coefficients. Klagyivik et al. (2013) suggested this relation might not be linear at low metallicity in the case of R_{21} and this is also likely the case for the relation based on $A_1 A_2$. Further

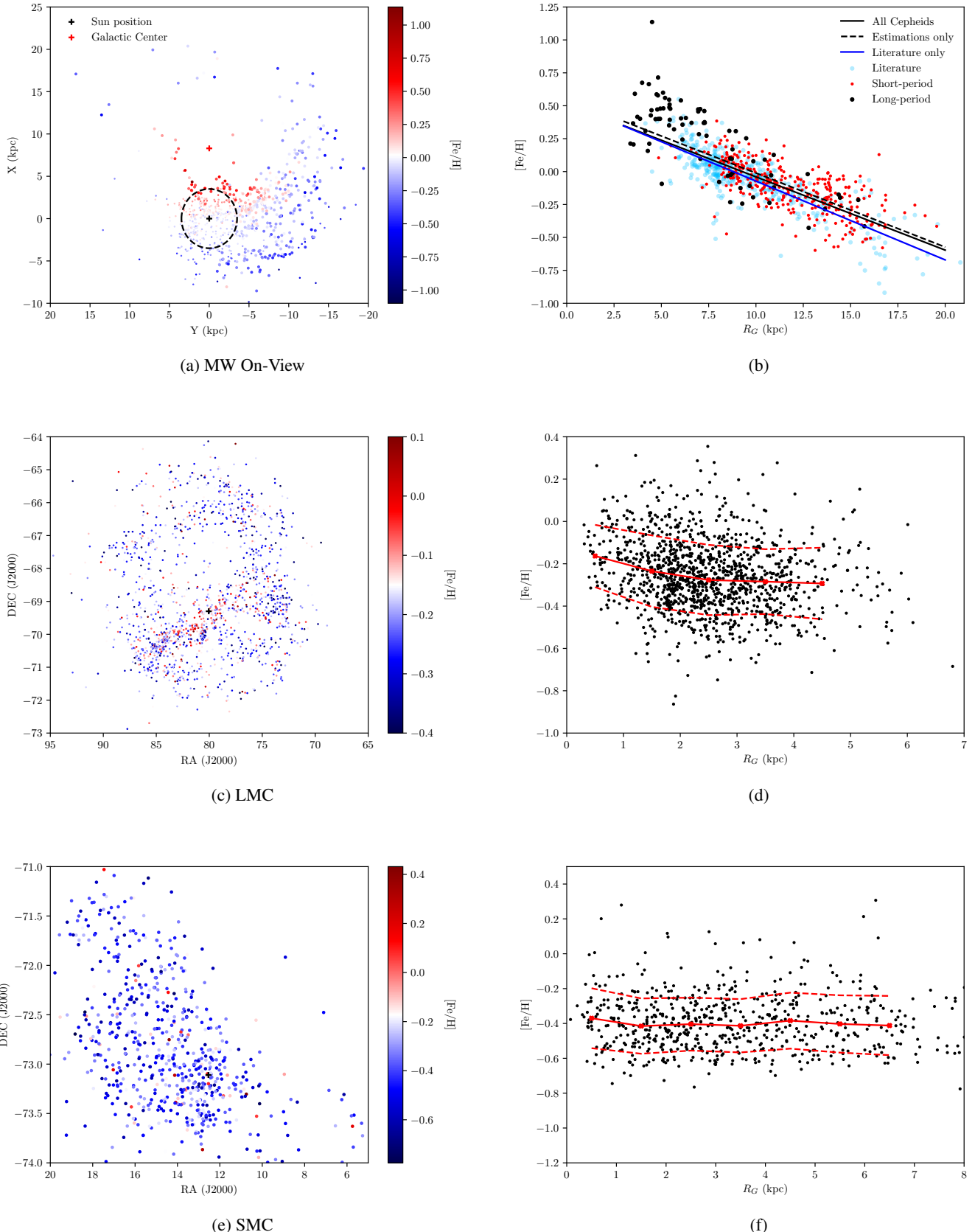


Fig. 16: (a), (c) and (e): Metallicity distribution of the Milky Way (868 stars), LMC (1561 stars) and SMC (674 stars) from empirical metallicity relations in the I -band. In a) small points represent stars with metallicity from the literature while bigger points are new metallicity estimation. Dashed circle encloses the solar neighbour region which concentrates most of the spectroscopic measurements. (b), (d) and (f): Estimated Cepheid metallicities versus the galactocentric distance for MW, LMC and SMC. Red dashed lines are the 1σ deviation in each bin of 1 kpc around the median value of each bin.

investigations are needed to find a unique relation between the Fourier coefficients that would be able to generalize from poor to rich metallic Cepheids.

Apart from the assumption of a linear relation, several physical source of scattering can affect the estimation of the metallicity. As discussed in the introduction, the presence of a companion or constant CSE emission would blend the amplitudes of the harmonics used in our relations and thus can be a source of scattering for empirical metallicity relations. Another significant source of scattering in these relations comes from physical effect such as the location in the instability strip that we were not able to correct for. As an alternative, we proposed to use selection threshold on A_1 in the case of short-period Cepheids. Although this cut was defined approximately, we think it is however necessary to mitigate the dependence of the amplitude on the location within the instability strip. It is thus important to better understand the influence of the location within the instability strip on the Fourier parameters to correct for this effect.

Theoretically, the impact of the metallicity on the Fourier parameters remains to be explained, just as it is for RR Lyrae. The metallicity dependence of the Fourier parameters can help to constraint hydrodynamical models of pulsation (Paxton et al. 2019). In this paper we also did not analyze the possibility of metallicity dependence between 6 and 10 days because of the strong sensitivity of the Fourier parameters to the P_2/P_0 resonance. A thorough understanding of the influence of the resonance on the Cepheid light curves is a prerequisite for the calibration of metallicity relation in this period range.

Using these relations for Cepheids in MW, SMC and LMC we have shown their capabilities for galactic archeology applications. Another possible application is to determine the metallicity term in PL relation. In order to study the metallicity term authors attribute in general the average metallicity of the host galaxy (measured from a restricted sample of stars) to the sample of Cepheids used in PL relation (see for example Breuval et al. (2022)). Our empirical relations offer the possibility to either derive the mean [Fe/H] of the studied sample used in PL relation, or to correct individually the stars. Although the associated uncertainties for these photometric [Fe/H] are of the order of 0.12-0.25 dex, our relations offer the advantage to be applicable to a significant number of stars.

This relation can be difficult to apply for galaxies beyond our local group as observed with HST or JWST. Indeed our empirical relations are limited to stars for which the photometry provides a good coverage of the pulsation cycle for applying a Fourier decomposition. This is not the case for Cepheids observed by space telescopes which contains usually only few epochs and make use of template to reconstruct the light-curve. A second limitation is due to the blending which affects more significantly the extragalactic Cepheids ($D > 10 \text{ Mpc}$) since the resolution of telescopes is not able to separate Cepheids from the stellar background (eg. Mochejska et al. (2000); Riess et al. (2020)). Although Fourier parameters (R_{j1} and ϕ_{j1}) are only slightly affected by the blending (Antonello 2002), this is not the case of the amplitudes and the harmonics on a magnitude scale. Thus an estimation of the blending for correcting the amplitudes would be necessary for applying empirical relations.

8. Conclusion

In this paper we gathered 586 [Fe/H] of fundamental Cepheids from the literature and we transformed them into the same scale. We then retrieved well sampled light curves for 545 of these stars

from different V -band catalogues. Using this data set we performed Fourier decomposition of the light curves. Then we fitted linear relations with all possible combinations of Fourier parameters (up to 4 at the same time) to provide the best empirical relations for estimating the metallicity of short ($2.5 < P < 6.3 \text{ days}$) and long-period Cepheids ($12 < P < 40 \text{ days}$).

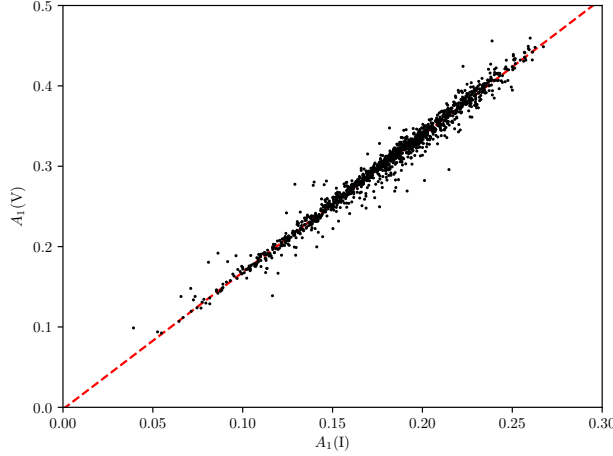
In the case of short-period Cepheids, we suggest to use relations based on explicit amplitudes A_1 and A_2 . Testing these relations on a sample of SMC and LMC Cepheids show that the relations are able to distinguish the populations. In the case of long-period Cepheids, we found that the metallicity can be estimated from the Fourier parameters A_1 , ϕ_{21} and R_{41} . We also found that this empirical relation can accurately derive the mean metallicity of a sample of SMC and LMC Cepheids. For individual metallicity determination, precisions of $\sigma=0.12 \text{ dex}$ and $\sigma=0.25 \text{ dex}$ have to be attributed for short- and long-period Cepheids respectively. These relations can be more efficient for estimating the average metallicity of a group of Cepheids rather than isolated stars. We then established new interrelations between V and I bands using OGLE data to convert these relations into the I -band. We have shown that our empirical relations are able to derive the mean metallicity of OGLE sample of the MW, SMC and LMC in agreement with spectroscopic mean estimates found in the literature. We also tested the relations in the I -band to map the metallicity distribution of MW, SMC and LMC and we were able to derive metallicity gradient consistent with the literature. Finally, the calibration of empirical relations can be still improved owing to further spectroscopic observations and homogeneous photometries in V and I band.

Acknowledgements. The authors would like to thank Dorota Skowron and Anna Jacyszyn-Dobrzeniecka for their valuable comments and discussion. VH, RS, OZ and RSR are supported by the National Science Center, Poland, Sonata BIS project 2018/30/E/ST9/00598. This research made use of the SIMBAD and VIZIER databases at CDS, Strasbourg (France) and the electronic bibliography maintained by the NASA/ADS system. This research also made use of Astropy, a community-developed core Python package for Astronomy (Astropy Collaboration et al. 2018, 2022).

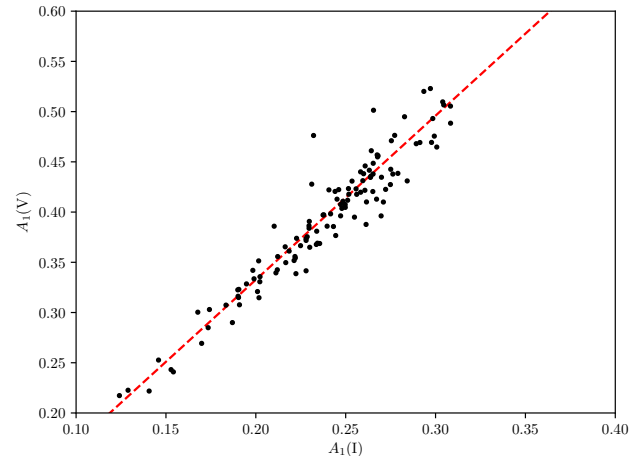
References

- Andrievsky, S. M., Kovtyukh, V. V., Korotin, S. A., Spite, M., & Spite, F. 2001, A&A, 367, 605
- Antonello, E. 1998, A&A, 333, L35
- Antonello, E. 2002, A&A, 391, 795
- Antonello, E. & Poretti, E. 1986, A&A, 169, 149
- Antonello, E., Poretti, E., & Reduzzi, L. 1990, A&A, 236, 138
- Asplund, M., Grevesse, N., Sauval, A. J., & Scott, P. 2009, ARA&A, 47, 481
- Astropy Collaboration, Price-Whelan, A. M., Lim, P. L., et al. 2022, ApJ, 935, 167
- Astropy Collaboration, Price-Whelan, A. M., Sipócz, B. M., et al. 2018, AJ, 156, 123
- Becker, S. A., Iben, I. J., & Tuggle, R. S. 1977, ApJ, 218, 633
- Bellinger, E. P., Kanbur, S. M., Bhardwaj, A., & Marconi, M. 2020, MNRAS, 491, 4752
- Berdnikov, L. N. 2008, VizieR Online Data Catalog, II/285
- Bobylev, V. V. & Bajkova, A. T. 2021, Astronomy Reports, 65, 498
- Bono, G., Caputo, F., & Castellani, V. 2006, Mem. Soc. Astron. Italiana, 77, 207
- Bono, G., Caputo, F., Fiorentino, G., Marconi, M., & Musella, I. 2008, ApJ, 684, 102
- Bono, G., Caputo, F., Marconi, M., & Musella, I. 2010, ApJ, 715, 277
- Bono, G., Castellani, V., & Marconi, M. 2000, ApJ, 529, 293
- Breuval, L., Kervella, P., Wielgórski, P., et al. 2021, ApJ, 913, 38
- Breuval, L., Riess, A. G., & Kervella, P. 2022, arXiv e-prints, arXiv:2205.06280
- Buchler, J. R. 1997, in Variables Stars and the Astrophysical Returns of the Microlensing Surveys, ed. R. Ferlet, J.-P. Maillard, & B. Raban, 181
- Buchler, J. R. 1998, in Astronomical Society of the Pacific Conference Series, Vol. 135, A Half Century of Stellar Pulsation Interpretation, ed. P. A. Bradley & J. A. Guzik, 220
- Buchler, J. R., Moskalik, P., & Kovacs, G. 1990, ApJ, 351, 617
- Cacciari, C., Corwin, T. M., & Carney, B. W. 2005, AJ, 129, 267

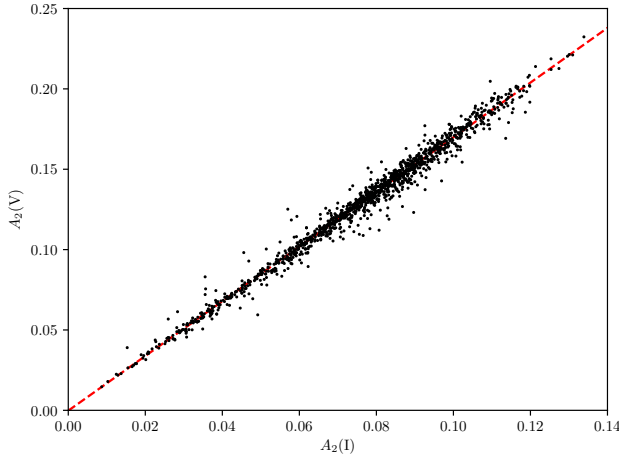
- Caputo, F., Marconi, M., Musella, I., & Santolamazza, P. 2000, A&A, 359, 1059
- Chilingarian, I. V. & Asa'd, R. 2018, ApJ, 858, 63
- Christy, R. F. 1968, QJRAS, 9, 13
- Christy, R. F. 1975, in NASA Special Publication, Vol. 383, 85–98
- Clementini, G., Ripepi, V., Molinaro, R., et al. 2019, A&A, 622, A60
- da Silva, R., Crestani, J., Bono, G., et al. 2022, arXiv e-prints, arXiv:2202.07945
- De Somma, G., Marconi, M., Molinaro, R., et al. 2022, arXiv e-prints, arXiv:2206.11154
- Dékány, I., Grebel, E. K., & Pojmanski, G. 2021, ApJ, 920, 33
- Dinnbier, F., Anderson, R. I., & Kroupa, P. 2022, A&A, 659, A169
- Dirsch, B., Richtler, T., Gieren, W. P., & Hilker, M. 2000, A&A, 360, 133
- Fiorentino, G., Musella, I., & Marconi, M. 2013, MNRAS, 434, 2866
- Gallenne, A., Mérard, A., Kervella, P., et al. 2013, A&A, 558, A140
- Gallenne, A., Mérard, A., Kervella, P., et al. 2021, A&A, 651, A113
- Genovali, K., Lemasle, B., Bono, G., et al. 2014, A&A, 566, A37
- Genovali, K., Lemasle, B., da Silva, R., et al. 2015, A&A, 580, A17
- Gieren, W., Storm, J., Konorski, P., et al. 2018, A&A, 620, A99
- Groenewegen, M. A. T. 2018, A&A, 619, A8
- Hajdu, G., Dékány, I., Catelan, M., Grebel, E. K., & Jurcsik, J. 2018, ApJ, 857, 55
- Hao, C. J., Xu, Y., Wu, Z. Y., et al. 2022, arXiv e-prints, arXiv:2210.01521
- Hendry, M. A., Tanvir, N. R., & Kanbur, S. M. 1999, in Astronomical Society of the Pacific Conference Series, Vol. 167, Harmonizing Cosmic Distance Scales in a Post-HIPPARCOS Era, ed. D. Egret & A. Heck, 192–197
- Hertzprung, E. 1926, Bull. Astron. Inst. Netherlands, 3, 115
- Hill, V. 1999, A&A, 345, 430
- Hill, V., Andrievsky, S., & Spite, M. 1995, A&A, 293, 347
- Hocdé, V., Nardetto, N., Borgniet, S., et al. 2020a, A&A, 641, A74
- Hocdé, V., Nardetto, N., Lagadec, E., et al. 2020b, A&A, 633, A47
- Hocdé, V., Nardetto, N., Matter, A., et al. 2021, A&A, 651, A92
- Inno, L., Urbaneja, M. A., Matsunaga, N., et al. 2019, MNRAS, 482, 83
- Jacyszyn-Dobrzeniecka, A. M., Skowron, D. M., Mróz, P., et al. 2016, Acta Astron., 66, 149
- Jayasinghe, T., Kochanek, C. S., Stanek, K. Z., et al. 2018, MNRAS, 477, 3145
- Jurcsik, J. & Kovacs, G. 1996, A&A, 312, 111
- Kanbur, S., Nikolaev, S., & Bouche, N. 2000, in American Astronomical Society Meeting Abstracts, Vol. 197, American Astronomical Society Meeting Abstracts, 104.02
- Karczmarek, P., Smolec, R., Hajdu, G., et al. 2022, ApJ, 930, 65
- Keller, S. C. 2008, ApJ, 677, 483
- Kervella, P., Gallenne, A., Remage Evans, N., et al. 2019, A&A, 623, A116
- Kervella, P., Mérard, A., Perrin, G., & Coudé du Foresto, V. 2006, A&A, 448, 623
- Klagyivik, P. & Szabados, L. 2007, Astronomische Nachrichten, 328, 825
- Klagyivik, P., Szabados, L., Szing, A., Leccia, S., & Mowlavi, N. 2013, MNRAS, 434, 2418
- Klapp, J., Goupil, M. J., & Buchler, J. R. 1985, ApJ, 296, 514
- Korn, A. J., Becker, S. R., Gummersbach, C. A., & Wolf, B. 2000, A&A, 353, 655
- Kovacs, G. & Buchler, J. R. 1989, ApJ, 346, 898
- Kovacs, G., Kisvársányi, E. G., & Buchler, J. R. 1990, ApJ, 351, 606
- Kovtyukh, V., Lemasle, B., Bono, G., et al. 2022a, MNRAS, 510, 1894
- Kovtyukh, V. V., Andrievsky, S. M., & Korotin, S. A. 2022b, MNRAS, 517, L143
- Kovtyukh, V. V., Andrievsky, S. M., Martin, R. P., et al. 2019, MNRAS, 489, 2254
- Kovtyukh, V. V., Korotin, S. A., Andrievsky, S. M., Matsunaga, N., & Fukue, K. 2022c, MNRAS, 516, 4269
- Leavitt, H. S. 1908, Annals of Harvard College Observatory, 60, 87
- Leavitt, H. S. & Pickering, E. C. 1912, Harvard College Observatory Circular, 173, 1
- Lemasle, B., Groenewegen, M. A. T., Grebel, E. K., et al. 2017, A&A, 608, A85
- Lomb, N. R. 1976, Ap&SS, 39, 447
- Luck, R. E. 2018, AJ, 156, 171
- Luck, R. E. & Lambert, D. L. 2011, AJ, 142, 136
- Majaess, D., Turner, D., Gieren, W., Berdnikov, L., & Lane, D. 2013, Ap&SS, 344, 381
- Mérard, A., Kervella, P., Coudé du Foresto, V., et al. 2006, A&A, 453, 155
- Miller, A. A., Bloom, J. S., Richards, J. W., et al. 2015, ApJ, 798, 122
- Minniti, J. H., Sbordone, L., Rojas-Arriagada, A., et al. 2020, A&A, 640, A92
- Mochejska, B. J., Macri, L. M., Sasselov, D. D., & Stanek, K. Z. 2000, AJ, 120, 810
- Molinaro, R., Ripepi, V., Marconi, M., et al. 2012, ApJ, 748, 69
- Mullen, J. P., Marengo, M., Martínez-Vázquez, C. E., et al. 2021, ApJ, 912, 144
- Musella, I., Marconi, M., Stetson, P. B., et al. 2016, MNRAS, 457, 3084
- Nardetto, N., Mérard, A., Mourard, D., et al. 2016, A&A, 593, A45
- Narlock, W., Pietrzyński, G., Gieren, W., et al. 2021, A&A, 647, A135
- Neilson, H. R., Cantiello, M., & Langer, N. 2011, A&A, 529, L9
- Ngeow, C.-C., Kanbur, S. M., Nikolaev, S., Tanvir, N. R., & Hendry, M. A. 2003, ApJ, 586, 959
- Paxton, B., Smolec, R., Schwab, J., et al. 2019, ApJS, 243, 10
- Petersen, J. O. 1986, A&A, 170, 59
- Pilecki, B., Pietrzyński, G., Anderson, R. I., et al. 2021, ApJ, 910, 118
- Pojmanski, G. 2002, Acta Astron., 52, 397
- Pont, F., Kienzle, F., Gieren, W., & Fouqué, P. 2001, A&A, 376, 892
- Riess, A. G., Casertano, S., Yuan, W., Macri, L. M., & Scolnic, D. 2019, ApJ, 876, 85
- Riess, A. G., Yuan, W., Casertano, S., Macri, L. M., & Scolnic, D. 2020, ApJ, 896, L43
- Riess, A. G., Yuan, W., Macri, L. M., et al. 2021, arXiv e-prints, arXiv:2112.04510
- Ripepi, V., Catanzaro, G., Molinaro, R., et al. 2021, MNRAS, 508, 4047
- Romanillo, M., Primas, F., Mottini, M., et al. 2008, A&A, 488, 731
- Romanillo, M., Riess, A., Mancino, S., et al. 2022, A&A, 658, A29
- Russell, S. C. & Bessell, M. S. 1989, ApJS, 70, 865
- Sandage, A. & Tammann, G. A. 1971, ApJ, 167, 293
- Sandage, A., Tammann, G. A., & Reindl, B. 2004, A&A, 424, 43
- Scargle, J. D. 1982, ApJ, 263, 835
- Scowcroft, V., Seibert, M., Freedman, W. L., et al. 2016, MNRAS, 459, 1170
- Sebo, K. M. & Wood, P. R. 1994, AJ, 108, 932
- Simon, N. R. & Lee, A. S. 1981, ApJ, 248, 291
- Simon, N. R. & Moffett, T. J. 1985, PASP, 97, 1078
- Simon, N. R. & Schmidt, E. G. 1976, ApJ, 205, 162
- Skowron, D. M., Skowron, J., Mróz, P., et al. 2019, Science, 365, 478
- Skowron, D. M., Skowron, J., Udalski, A., et al. 2021, ApJS, 252, 23
- Skowron, D. M., Soszyński, I., Udalski, A., et al. 2016, Acta Astron., 66, 269
- Smolec, R. 2005, Acta Astron., 55, 59
- Soszyński, I., Poleski, R., Udalski, A., et al. 2008, Acta Astron., 58, 163
- Soszyński, I., Poleski, R., Udalski, A., et al. 2010, Acta Astron., 60, 17
- Soszyński, I., Udalski, A., Szymański, M. K., et al. 2017, Acta Astron., 67, 297
- Stobie, R. S. 1969, MNRAS, 144, 511
- Szabados, L. 2003, Information Bulletin on Variable Stars, 5394, 1
- Szabados, L. & Klagyivik, P. 2012, A&A, 537, A81
- Testa, V., Marconi, M., Musella, I., et al. 2007, A&A, 462, 599
- Trentin, E., Ripepi, V., Catanzaro, G., et al. 2022, arXiv e-prints, arXiv:2209.03792
- Trundle, C., Dufton, P. L., Hunter, I., et al. 2007, A&A, 471, 625
- Udalski, A., Soszyński, I., Pietrukowicz, P., et al. 2018, Acta Astron., 68, 315
- Udalski, A., Szymański, M. K., & Szymański, G. 2015, Acta Astron., 65, 1
- Urbaneja, M. A., Kudritzki, R. P., Gieren, W., et al. 2017, AJ, 154, 102
- Welch, D. L. & Stetson, P. B. 1993, AJ, 105, 1813
- Whitney, C. 1956, AJ, 61, 192
- Wielgórski, P., Pietrzyński, G., Pilecki, B., et al. 2022, ApJ, 927, 89
- Xu, Q.-S. & Liang, Y.-Z. 2001, Chemometrics and Intelligent Laboratory Systems, 56, 1
- Zsoldos, E. 1995, in Astronomical Society of the Pacific Conference Series, Vol. 83, IAU Colloq. 155: Astrophysical Applications of Stellar Pulsation, ed. R. S. Stobie & P. A. Whitelock, 351



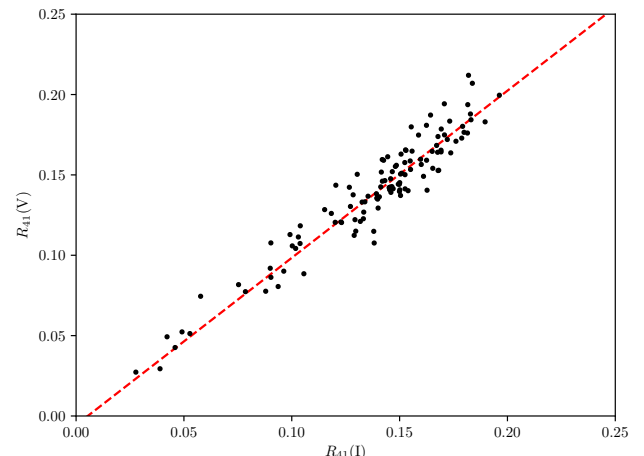
(a)



(a)



(b)



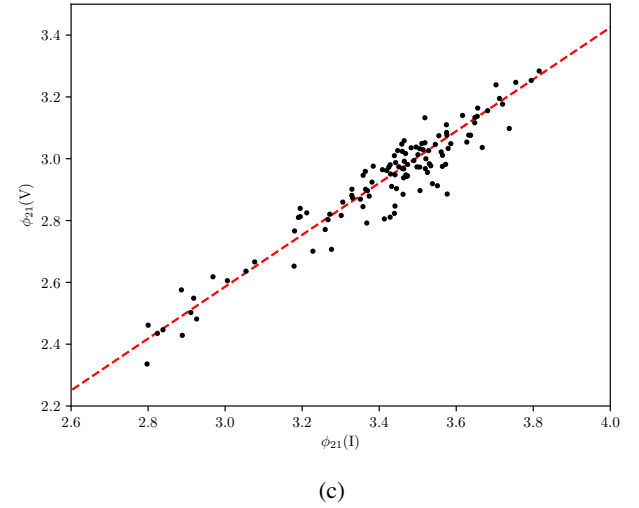
(b)

Fig. A.1: Interrelations for A_1 and A_2 between V and I -bands for short short-periods Cepheids between 2.5 and 6.3 days.

Appendix A: Interrelations

Appendix B: MW and LMC map

Appendix C: Data set



(c)

Fig. A.2: Interrelations for A_1 , R_{41} and ϕ_{21} between V and I -bands for long-periods Cepheids between 12 and 40 days.

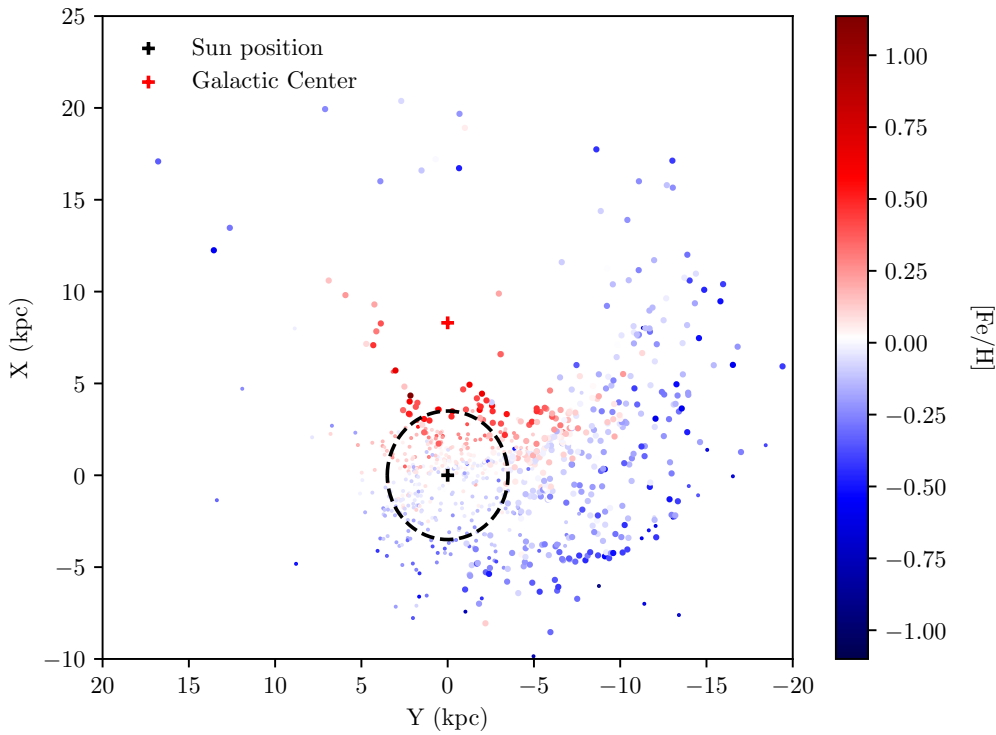


Fig. B.1: MW On-View

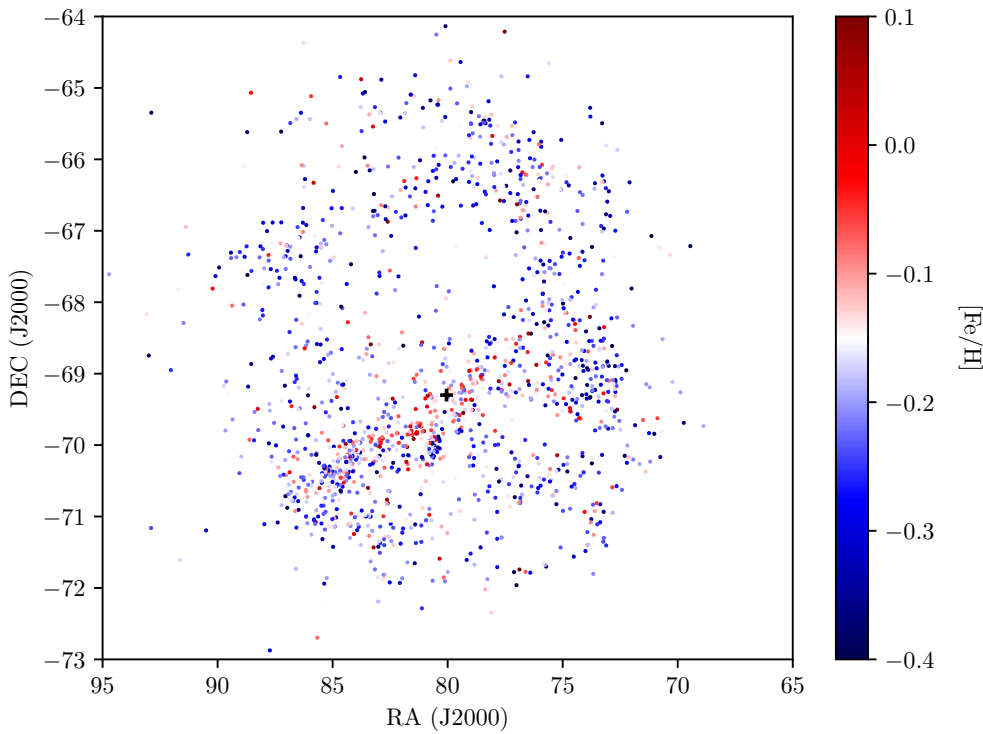


Fig. B.2: LMC

Table C.1: Final data set of Fourier parameters of V -band light-curves with spectroscopic metallicities. This data set is composed of 545 Cepheids with metallicity from about -1.0 to 0.4 dex which are from L11 (Luck & Lambert 2011); L18 (Luck 2018); G14 (Genovali et al. 2014); G15 (Genovali et al. 2015); L17 (Lemasle et al. 2017); R21 (Ripepi et al. 2021); R08 (Romaniello et al. 2008); R22 (Romaniello et al. 2022); T22 (Trentin et al. 2022); K22 (Kovtyukh et al. 2022a). All [Fe/H] are scaled to solar abundance value $A(\text{Fe})_0=7.50$ given by Asplund et al. (2009) and corrected from offsets if necessary, see Sect. 2 for details. Sources of the V -band light curve are from ASAS-SN (Jayasinghe et al. 2018); ASAS (Pojmanski 2002); BER08 (Berdnikov 2008); OGLE-III and OGLE-IV (Soszyński et al. 2008, 2010). The dispersion of the fit σ is indicated, as defined in Eq. 5.

| Star | Source | Period | [Fe/H] | Ref. | A_1 | ϕ_{21} | ϕ_{31} | ϕ_{41} | R_{21} | R_{31} | R_{41} | σ |
|------------|---------|--------|--------|------|-------|-------------|-------------|-------------|----------|----------|----------|----------|
| U Aql | BER08 | 7.024 | 0.081 | L18 | 0.322 | 3.306 | 5.891 | 5.656 | 0.345 | 0.146 | 0.028 | 0.024 |
| SZ Aql | BER08 | 17.139 | 0.151 | L18 | 0.493 | 2.891 | 5.092 | 1.426 | 0.277 | 0.161 | 0.143 | 0.021 |
| TT Aql | BER08 | 13.755 | 0.100 | L18 | 0.443 | 2.893 | 4.681 | 1.000 | 0.217 | 0.139 | 0.132 | 0.021 |
| EV Aql | ASAS | 38.576 | -0.021 | L18 | 0.309 | 3.025 | 6.197 | 3.086 | 0.373 | 0.137 | 0.080 | 0.052 |
| FM Aql | BER08 | 6.114 | 0.052 | L18 | 0.311 | 2.980 | 5.759 | 2.017 | 0.354 | 0.110 | 0.034 | 0.022 |
| FN Aql | ASAS | 9.482 | -0.113 | L18 | 0.259 | 5.796 | 3.474 | 0.192 | 0.021 | 0.079 | 0.043 | 0.014 |
| KL Aql | ASAS | 6.108 | 0.226 | L18 | 0.300 | 3.056 | 5.709 | 2.639 | 0.381 | 0.109 | 0.054 | 0.024 |
| η Aql | BER08 | 7.177 | 0.054 | L18 | 0.333 | 3.391 | 5.938 | 0.237 | 0.337 | 0.172 | 0.033 | 0.028 |
| V336 Aql | ASAS | 7.304 | 0.081 | L18 | 0.308 | 3.350 | 6.009 | 6.070 | 0.346 | 0.146 | 0.038 | 0.014 |
| V480 Aql | ASAS-SN | 18.996 | 0.170 | T22 | 0.358 | 2.617 | 0.032 | 1.050 | 0.245 | 0.131 | 0.077 | 0.019 |
| V493 Aql | ASAS-SN | 2.987 | -0.048 | L18 | 0.268 | 2.563 | 5.381 | 0.877 | 0.307 | 0.139 | 0.062 | 0.027 |
| V600 Aql | ASAS | 7.240 | -0.110 | L18 | 0.278 | 3.409 | 6.258 | 0.452 | 0.361 | 0.121 | 0.034 | 0.018 |
| V733 Aql | BER08 | 6.179 | -0.022 | L18 | 0.197 | 3.058 | 5.072 | 5.317 | 0.300 | 0.045 | 0.040 | 0.024 |
| V912 Aql | ASAS-SN | 4.400 | 0.140 | R21 | 0.296 | 2.680 | 5.411 | 2.093 | 0.375 | 0.172 | 0.062 | 0.014 |
| V916 Aql | ASAS-SN | 13.442 | 0.248 | L18 | 0.386 | 2.676 | 4.257 | 0.575 | 0.201 | 0.117 | 0.112 | 0.018 |
| V1162 Aql | BER08 | 5.376 | -0.025 | L18 | 0.223 | 2.885 | 5.964 | 3.751 | 0.335 | 0.087 | 0.009 | 0.027 |
| V1495 Aql | ASAS-SN | 8.797 | 0.550 | R21 | 0.283 | 3.508 | 0.890 | 2.617 | 0.136 | 0.093 | 0.089 | 0.011 |
| V1496 Aql | BER08 | 55.917 | -0.070 | R21 | 0.242 | 3.222 | 2.932 | 1.641 | 0.163 | 0.100 | 0.070 | 0.026 |
| V340 Ara | BER08 | 20.810 | 0.381 | L18 | 0.467 | 2.828 | 5.102 | 1.463 | 0.298 | 0.161 | 0.116 | 0.022 |
| Y Aur | ASAS-SN | 3.860 | -0.074 | L18 | 0.283 | 2.696 | 5.589 | 2.124 | 0.345 | 0.214 | 0.058 | 0.040 |
| RT Aur | ASAS-SN | 3.729 | 0.032 | L18 | 0.363 | 2.610 | 5.393 | 1.681 | 0.363 | 0.203 | 0.107 | 0.077 |
| RX Aur | BER08 | 11.624 | -0.045 | L18 | 0.301 | 2.448 | 3.928 | 0.138 | 0.142 | 0.104 | 0.065 | 0.021 |
| SY Aur | BER08 | 10.145 | -0.063 | L18 | 0.300 | 2.748 | 2.530 | 3.908 | 0.155 | 0.042 | 0.038 | 0.024 |
| YZ Aur | BER08 | 18.193 | -0.359 | L18 | 0.366 | 2.957 | 4.702 | 1.285 | 0.188 | 0.110 | 0.117 | 0.022 |
| AN Aur | BER08 | 10.289 | -0.211 | L18 | 0.307 | 3.954 | 1.809 | 3.574 | 0.131 | 0.151 | 0.105 | 0.015 |
| AO Aur | ASAS-SN | 6.762 | -0.345 | L18 | 0.361 | 3.070 | 5.725 | 2.727 | 0.444 | 0.188 | 0.108 | 0.042 |
| AS Aur | ASAS-SN | 3.175 | -0.203 | L18 | 0.268 | 2.616 | 5.308 | 1.643 | 0.435 | 0.212 | 0.098 | 0.016 |
| AX Aur | ASAS-SN | 3.047 | -0.140 | L18 | 0.217 | 2.512 | 5.212 | 1.432 | 0.377 | 0.165 | 0.070 | 0.018 |
| BK Aur | BER08 | 7.805 | -0.025 | L18 | 0.320 | 3.613 | 0.410 | 6.184 | 0.220 | 0.120 | 0.031 | 0.039 |
| CY Aur | ASAS-SN | 13.845 | -0.259 | L18 | 0.377 | 3.012 | 4.493 | 0.944 | 0.192 | 0.119 | 0.144 | 0.011 |
| ER Aur | ASAS-SN | 15.698 | -0.367 | L18 | 0.250 | 2.356 | 4.387 | 0.403 | 0.202 | 0.133 | 0.079 | 0.012 |
| EW Aur | ASAS-SN | 2.660 | -0.537 | L18 | 0.293 | 2.561 | 5.313 | 1.735 | 0.493 | 0.277 | 0.142 | 0.017 |
| GT Aur | ASAS-SN | 4.405 | -0.074 | L18 | 0.340 | 2.582 | 5.248 | 1.736 | 0.380 | 0.162 | 0.077 | 0.022 |
| GV Aur | ASAS-SN | 5.260 | -0.243 | L18 | 0.350 | 2.876 | 5.775 | 2.366 | 0.461 | 0.205 | 0.106 | 0.013 |
| IN Aur | ASAS-SN | 4.910 | -0.285 | L18 | 0.221 | 2.981 | 6.061 | 2.815 | 0.404 | 0.157 | 0.055 | 0.028 |
| V335 Aur | BER08 | 3.413 | -0.315 | L18 | 0.371 | 2.636 | 5.315 | 1.658 | 0.475 | 0.256 | 0.134 | 0.021 |
| T Ant | ASAS | 5.898 | -0.275 | L18 | 0.345 | 3.027 | 5.916 | 2.550 | 0.446 | 0.170 | 0.092 | 0.017 |
| RW Cam | BER08 | 16.415 | 0.050 | L18 | 0.363 | 2.768 | 4.574 | 0.883 | 0.208 | 0.136 | 0.121 | 0.016 |
| RX Cam | BER08 | 7.909 | -0.011 | L18 | 0.317 | 3.295 | 0.040 | 1.344 | 0.258 | 0.086 | 0.143 | 0.030 |
| TV Cam | ASAS-SN | 5.295 | -0.056 | L18 | 0.371 | 2.878 | 5.696 | 2.103 | 0.434 | 0.175 | 0.104 | 0.013 |
| AB Cam | ASAS-SN | 5.787 | -0.146 | L18 | 0.365 | 3.003 | 5.658 | 2.384 | 0.438 | 0.168 | 0.115 | 0.015 |
| AC Cam | ASAS-SN | 4.157 | -0.182 | L18 | 0.266 | 2.801 | 5.599 | 2.395 | 0.401 | 0.181 | 0.088 | 0.019 |
| AD Cam | ASAS-SN | 11.262 | -0.343 | L18 | 0.364 | 3.009 | 4.727 | 0.966 | 0.278 | 0.167 | 0.198 | 0.015 |
| AM Cam | ASAS-SN | 3.997 | -0.189 | L18 | 0.232 | 2.714 | 5.532 | 2.354 | 0.389 | 0.164 | 0.059 | 0.012 |
| CF Cam | ASAS-SN | 9.435 | -0.170 | R21 | 0.283 | 3.120 | 0.447 | 2.054 | 0.165 | 0.084 | 0.079 | 0.014 |
| CK Cam | ASAS-SN | 3.295 | -0.040 | L18 | 0.262 | 2.599 | 5.422 | 1.410 | 0.344 | 0.136 | 0.061 | 0.068 |
| LO Cam | ASAS-SN | 12.646 | -0.149 | L18 | 0.333 | 2.585 | 3.753 | 5.850 | 0.201 | 0.088 | 0.068 | 0.040 |
| MN Cam | ASAS-SN | 8.179 | -0.084 | L18 | 0.260 | 3.727 | 0.722 | 2.088 | 0.254 | 0.135 | 0.088 | 0.024 |
| MQ Cam | ASAS-SN | 6.604 | -0.163 | L18 | 0.247 | 3.282 | 6.070 | 5.644 | 0.368 | 0.126 | 0.026 | 0.017 |
| OX Cam | ASAS-SN | 5.066 | -0.122 | L18 | 0.301 | 2.772 | 5.512 | 2.213 | 0.401 | 0.136 | 0.061 | 0.022 |
| QS Cam | ASAS-SN | 5.125 | -0.315 | L18 | 0.280 | 2.873 | 5.744 | 1.977 | 0.388 | 0.154 | 0.050 | 0.020 |
| V359 Cam | ASAS-SN | 6.570 | -0.221 | L18 | 0.299 | 3.171 | 5.864 | 3.059 | 0.387 | 0.135 | 0.033 | 0.015 |
| U Car | BER08 | 38.783 | 0.056 | L18 | 0.451 | 3.158 | 6.270 | 3.050 | 0.483 | 0.249 | 0.130 | 0.031 |
| V Car | BER08 | 6.697 | -0.056 | L18 | 0.254 | 3.299 | 5.975 | 6.104 | 0.346 | 0.085 | 0.037 | 0.014 |

Continued on next page

Table C.1 – continued from previous page

| Star | Source | Period | [Fe/H] | Ref. | A_1 | ϕ_{21} | ϕ_{31} | ϕ_{41} | R_{21} | R_{31} | R_{41} | σ |
|------------|---------|--------|--------|------|-------|-------------|-------------|-------------|----------|----------|----------|----------|
| SX Car | ASAS | 4.860 | -0.043 | L18 | 0.327 | 2.769 | 5.614 | 1.908 | 0.374 | 0.157 | 0.054 | 0.019 |
| UW Car | BER08 | 5.346 | -0.029 | L18 | 0.350 | 2.798 | 5.583 | 1.992 | 0.386 | 0.171 | 0.087 | 0.019 |
| UX Car | BER08 | 3.682 | -0.025 | L18 | 0.341 | 2.626 | 5.333 | 1.714 | 0.360 | 0.164 | 0.071 | 0.011 |
| UY Car | ASAS | 5.544 | 0.034 | L18 | 0.326 | 2.915 | 5.751 | 2.193 | 0.373 | 0.120 | 0.051 | 0.010 |
| UZ Car | BER08 | 5.209 | 0.048 | L18 | 0.270 | 2.912 | 5.903 | 1.975 | 0.362 | 0.113 | 0.044 | 0.013 |
| VY Car | BER08 | 18.897 | 0.025 | L18 | 0.461 | 2.810 | 4.963 | 1.194 | 0.259 | 0.146 | 0.124 | 0.024 |
| WW Car | ASAS | 4.677 | -0.094 | L18 | 0.330 | 2.745 | 5.578 | 2.139 | 0.385 | 0.167 | 0.068 | 0.018 |
| WZ Car | ASAS | 23.011 | -0.020 | L18 | 0.496 | 3.015 | 5.913 | 2.618 | 0.404 | 0.266 | 0.184 | 0.017 |
| XX Car | BER08 | 15.705 | 0.093 | L18 | 0.482 | 2.929 | 5.264 | 1.665 | 0.289 | 0.204 | 0.173 | 0.016 |
| XY Car | ASAS | 12.437 | -0.024 | L18 | 0.362 | 2.670 | 3.831 | 0.416 | 0.110 | 0.127 | 0.111 | 0.014 |
| XZ Car | BER08 | 16.652 | 0.126 | L18 | 0.437 | 2.852 | 4.832 | 1.142 | 0.254 | 0.136 | 0.125 | 0.015 |
| YZ Car | BER08 | 18.166 | -0.046 | L18 | 0.356 | 2.580 | 5.047 | 1.396 | 0.275 | 0.175 | 0.101 | 0.009 |
| AQ Car | ASAS | 9.769 | -0.062 | L18 | 0.265 | 5.161 | 2.720 | 5.154 | 0.067 | 0.094 | 0.043 | 0.011 |
| CC Car | ASAS-SN | 4.760 | 0.100 | K22 | 0.227 | 2.716 | 0.107 | 1.925 | 0.347 | 0.105 | 0.036 | 0.034 |
| CN Car | BER08 | 4.932 | 0.050 | L18 | 0.288 | 2.782 | 5.643 | 1.862 | 0.348 | 0.136 | 0.042 | 0.020 |
| CR Car | ASAS-SN | 9.758 | 0.080 | K22 | 0.244 | 4.542 | 0.079 | 4.044 | 0.111 | 0.099 | 0.067 | 0.017 |
| CT Car | ASAS-SN | 18.067 | 0.010 | K22 | 0.391 | 2.821 | 0.038 | 1.242 | 0.261 | 0.144 | 0.124 | 0.019 |
| CY Car | ASAS | 4.266 | 0.004 | L18 | 0.240 | 2.671 | 5.524 | 1.865 | 0.334 | 0.125 | 0.035 | 0.015 |
| DY Car | ASAS-SN | 4.675 | -0.031 | G14 | 0.304 | 2.756 | 5.591 | 2.112 | 0.397 | 0.185 | 0.073 | 0.021 |
| ER Car | BER08 | 7.718 | 0.036 | L18 | 0.245 | 3.579 | 0.016 | 0.820 | 0.292 | 0.071 | 0.057 | 0.011 |
| FI Car | BER08 | 13.458 | 0.176 | L18 | 0.332 | 2.234 | 3.679 | 6.200 | 0.087 | 0.118 | 0.066 | 0.021 |
| FN Car | ASAS-SN | 4.586 | 0.070 | K22 | 0.255 | 2.693 | 0.069 | 2.150 | 0.370 | 0.150 | 0.036 | 0.030 |
| FO Car | ASAS-SN | 10.358 | -0.511 | L11 | 0.244 | 1.014 | 3.238 | 6.095 | 0.030 | 0.108 | 0.055 | 0.015 |
| FR Car | ASAS | 10.717 | -0.019 | L18 | 0.317 | 1.881 | 3.538 | 0.185 | 0.035 | 0.117 | 0.063 | 0.015 |
| GX Car | ASAS | 7.197 | 0.029 | L18 | 0.324 | 3.377 | 6.014 | 0.660 | 0.343 | 0.181 | 0.054 | 0.020 |
| HQ Car | ASAS-SN | 14.102 | -0.171 | G14 | 0.411 | 3.055 | 5.551 | 0.314 | 0.494 | 0.088 | 0.040 | 0.056 |
| HW Car | ASAS | 9.200 | -0.032 | L18 | 0.165 | 5.345 | 2.808 | 0.403 | 0.080 | 0.046 | 0.011 | 0.011 |
| ℓ Car | BER08 | 35.548 | 0.059 | L18 | 0.324 | 2.820 | 5.425 | 2.117 | 0.314 | 0.141 | 0.063 | 0.023 |
| RS Cas | BER08 | 6.296 | 0.085 | L18 | 0.334 | 3.029 | 5.765 | 3.316 | 0.408 | 0.114 | 0.059 | 0.037 |
| RY Cas | BER08 | 12.139 | 0.120 | L18 | 0.392 | 2.451 | 3.931 | 5.960 | 0.204 | 0.110 | 0.109 | 0.027 |
| SW Cas | BER08 | 5.441 | 0.016 | L18 | 0.293 | 2.876 | 5.929 | 1.987 | 0.378 | 0.137 | 0.083 | 0.028 |
| SY Cas | BER08 | 4.071 | -0.054 | L18 | 0.342 | 2.687 | 5.438 | 1.561 | 0.361 | 0.154 | 0.071 | 0.025 |
| UZ Cas | ASAS-SN | 4.260 | -0.146 | L18 | 0.312 | 2.751 | 5.575 | 2.236 | 0.399 | 0.177 | 0.082 | 0.009 |
| VV Cas | BER08 | 6.206 | -0.133 | L18 | 0.379 | 3.190 | 6.075 | 2.802 | 0.430 | 0.207 | 0.144 | 0.030 |
| VW Cas | BER08 | 5.994 | 0.096 | L18 | 0.289 | 3.044 | 5.695 | 2.465 | 0.370 | 0.113 | 0.025 | 0.028 |
| XY Cas | BER08 | 4.501 | -0.038 | L18 | 0.238 | 2.773 | 5.841 | 2.369 | 0.333 | 0.111 | 0.012 | 0.038 |
| AP Cas | ASAS-SN | 6.846 | -0.060 | L18 | 0.236 | 3.280 | 6.065 | 6.092 | 0.341 | 0.082 | 0.039 | 0.017 |
| AW Cas | ASAS-SN | 4.278 | -0.073 | L18 | 0.307 | 2.685 | 5.423 | 2.139 | 0.398 | 0.196 | 0.094 | 0.015 |
| AY Cas | ASAS-SN | 2.871 | -0.064 | L18 | 0.300 | 2.566 | 5.212 | 1.372 | 0.342 | 0.152 | 0.067 | 0.034 |
| BF Cas | ASAS-SN | 3.630 | -0.139 | L18 | 0.339 | 2.640 | 5.354 | 1.792 | 0.416 | 0.218 | 0.113 | 0.021 |
| BP Cas | ASAS-SN | 6.272 | -0.029 | L18 | 0.311 | 3.111 | 5.643 | 3.246 | 0.367 | 0.128 | 0.043 | 0.019 |
| BV Cas | ASAS-SN | 5.400 | -0.054 | L18 | 0.333 | 2.683 | 5.509 | 1.981 | 0.396 | 0.176 | 0.088 | 0.014 |
| CD Cas | BER08 | 7.800 | 0.043 | L18 | 0.350 | 3.319 | 6.088 | 1.027 | 0.298 | 0.163 | 0.059 | 0.027 |
| CF Cas | BER08 | 4.875 | -0.059 | L18 | 0.242 | 2.765 | 5.700 | 1.971 | 0.350 | 0.121 | 0.031 | 0.019 |
| CG Cas | ASAS-SN | 4.365 | -0.034 | L18 | 0.338 | 2.687 | 5.386 | 1.978 | 0.377 | 0.179 | 0.081 | 0.015 |
| CH Cas | BER08 | 15.089 | 0.039 | L18 | 0.426 | 2.751 | 4.611 | 0.734 | 0.242 | 0.167 | 0.138 | 0.031 |
| CT Cas | ASAS-SN | 3.811 | -0.139 | L18 | 0.244 | 2.685 | 5.481 | 1.956 | 0.403 | 0.182 | 0.063 | 0.012 |
| CY Cas | BER08 | 14.378 | -0.036 | L18 | 0.469 | 3.053 | 5.222 | 1.655 | 0.298 | 0.165 | 0.146 | 0.040 |
| CZ Cas | ASAS-SN | 5.665 | -0.049 | L18 | 0.327 | 2.899 | 5.714 | 2.332 | 0.375 | 0.133 | 0.067 | 0.019 |
| DD Cas | BER08 | 9.812 | -0.028 | L18 | 0.269 | 5.351 | 3.262 | 0.519 | 0.059 | 0.079 | 0.064 | 0.029 |
| DF Cas | BER08 | 3.822 | 0.119 | G14 | 0.267 | 2.733 | 5.121 | 2.072 | 0.331 | 0.124 | 0.052 | 0.013 |
| DL Cas | BER08 | 8.001 | -0.054 | L18 | 0.254 | 3.453 | 6.041 | 0.878 | 0.282 | 0.099 | 0.049 | 0.016 |
| DW Cas | ASAS-SN | 4.997 | -0.028 | L18 | 0.251 | 2.867 | 5.807 | 1.458 | 0.358 | 0.106 | 0.027 | 0.022 |
| EX Cas | BER08 | 4.298 | -0.110 | L18 | 0.256 | 2.748 | 5.494 | 1.846 | 0.372 | 0.158 | 0.031 | 0.018 |
| FM Cas | ASAS-SN | 5.809 | -0.178 | L18 | 0.237 | 3.034 | 5.837 | 4.521 | 0.440 | 0.039 | 0.045 | 0.064 |
| FO Cas | ASAS-SN | 6.799 | -0.516 | L18 | 0.251 | 3.196 | 0.110 | 1.959 | 0.290 | 0.273 | 0.136 | 0.021 |
| FW Cas | ASAS-SN | 6.240 | -0.153 | L18 | 0.225 | 3.217 | 6.122 | 0.114 | 0.350 | 0.076 | 0.026 | 0.013 |
| GL Cas | ASAS-SN | 4.007 | -0.098 | L18 | 0.285 | 2.672 | 5.481 | 2.159 | 0.404 | 0.213 | 0.108 | 0.016 |
| GM Cas | ASAS-SN | 7.468 | -0.172 | L18 | 0.203 | 3.451 | 6.167 | 0.165 | 0.324 | 0.086 | 0.063 | 0.056 |
| GO Cas | ASAS-SN | 3.239 | 0.006 | L18 | 0.230 | 2.533 | 5.152 | 1.333 | 0.339 | 0.138 | 0.051 | 0.017 |
| KK Cas | ASAS-SN | 8.192 | 0.012 | L18 | 0.253 | 3.736 | 0.632 | 2.164 | 0.259 | 0.127 | 0.087 | 0.023 |

Continued on next page

Table C.1 – continued from previous page

| Star | Source | Period | [Fe/H] | Ref. | A_1 | ϕ_{21} | ϕ_{31} | ϕ_{41} | R_{21} | R_{31} | R_{41} | σ |
|-----------|---------|--------|--------|------|-------|-------------|-------------|-------------|----------|----------|----------|----------|
| LT Cas | BER08 | 5.904 | -0.443 | L18 | 0.388 | 2.821 | 5.639 | 2.126 | 0.446 | 0.171 | 0.095 | 0.029 |
| NP Cas | ASAS-SN | 6.167 | -0.082 | L18 | 0.260 | 2.800 | 5.627 | 2.249 | 0.355 | 0.136 | 0.049 | 0.020 |
| OP Cas | ASAS-SN | 5.513 | 0.060 | L18 | 0.249 | 2.924 | 5.728 | 2.570 | 0.350 | 0.099 | 0.026 | 0.013 |
| OZ Cas | ASAS-SN | 5.079 | -0.034 | L18 | 0.279 | 2.758 | 5.548 | 2.233 | 0.317 | 0.116 | 0.042 | 0.019 |
| PW Cas | ASAS-SN | 4.000 | -0.149 | L18 | 0.217 | 2.742 | 5.344 | 1.338 | 0.352 | 0.167 | 0.032 | 0.017 |
| V342 Cas | ASAS-SN | 3.920 | -0.068 | L18 | 0.208 | 2.614 | 5.292 | 1.434 | 0.335 | 0.132 | 0.038 | 0.014 |
| V395 Cas | ASAS-SN | 4.037 | -0.066 | L18 | 0.244 | 2.617 | 5.418 | 1.499 | 0.317 | 0.121 | 0.039 | 0.014 |
| V407 Cas | BER08 | 4.566 | -0.014 | L18 | 0.204 | 2.741 | 5.737 | 1.331 | 0.319 | 0.106 | 0.017 | 0.011 |
| V556 Cas | ASAS-SN | 6.041 | -0.085 | L18 | 0.204 | 3.064 | 5.938 | 4.349 | 0.319 | 0.059 | 0.015 | 0.013 |
| V1017 Cas | ASAS-SN | 5.030 | -0.251 | L18 | 0.339 | 2.863 | 5.739 | 2.256 | 0.441 | 0.194 | 0.112 | 0.014 |
| V1020 Cas | ASAS-SN | 4.743 | 0.065 | L18 | 0.260 | 2.735 | 5.502 | 1.830 | 0.348 | 0.139 | 0.048 | 0.015 |
| V1100 Cas | ASAS-SN | 4.703 | -0.076 | L18 | 0.267 | 2.761 | 5.602 | 1.872 | 0.359 | 0.138 | 0.049 | 0.018 |
| V1206 Cas | ASAS-SN | 4.735 | -0.215 | L18 | 0.195 | 2.780 | 5.893 | 3.063 | 0.360 | 0.107 | 0.027 | 0.025 |
| V Cen | BER08 | 5.494 | -0.070 | L18 | 0.329 | 2.926 | 5.810 | 2.205 | 0.403 | 0.146 | 0.070 | 0.012 |
| TX Cen | BER08 | 17.098 | 0.355 | L18 | 0.464 | 2.831 | 5.014 | 1.246 | 0.266 | 0.145 | 0.128 | 0.028 |
| VW Cen | BER08 | 15.035 | 0.280 | L18 | 0.431 | 2.711 | 4.415 | 0.622 | 0.204 | 0.134 | 0.106 | 0.027 |
| XX Cen | BER08 | 10.952 | 0.054 | L18 | 0.373 | 2.657 | 3.459 | 5.418 | 0.138 | 0.116 | 0.100 | 0.016 |
| AY Cen | ASAS | 5.309 | -0.024 | L18 | 0.236 | 2.869 | 5.924 | 2.468 | 0.342 | 0.101 | 0.023 | 0.013 |
| KK Cen | ASAS-SN | 12.183 | 0.131 | L18 | 0.390 | 2.538 | 4.118 | 6.249 | 0.210 | 0.143 | 0.103 | 0.017 |
| KN Cen | BER08 | 34.037 | 0.369 | L18 | 0.437 | 2.913 | 5.680 | 2.482 | 0.385 | 0.233 | 0.138 | 0.024 |
| MY Cen | ASAS-SN | 3.718 | 0.050 | K22 | 0.300 | 2.605 | 0.033 | 1.685 | 0.350 | 0.153 | 0.072 | 0.017 |
| MZ Cen | ASAS-SN | 10.354 | 0.199 | G15 | 0.303 | 5.305 | 3.055 | 5.544 | 0.002 | 0.092 | 0.038 | 0.018 |
| OO Cen | BER08 | 12.881 | 0.129 | G15 | 0.357 | 2.459 | 3.908 | 0.404 | 0.074 | 0.107 | 0.062 | 0.028 |
| QY Cen | BER08 | 17.751 | 0.139 | G14 | 0.439 | 2.945 | 5.071 | 1.357 | 0.268 | 0.150 | 0.127 | 0.027 |
| V339 Cen | BER08 | 9.477 | 0.053 | L18 | 0.270 | 4.884 | 2.330 | 2.854 | 0.085 | 0.068 | 0.066 | 0.040 |
| V381 Cen | BER08 | 5.079 | -0.045 | L18 | 0.301 | 2.828 | 5.729 | 2.077 | 0.356 | 0.136 | 0.050 | 0.014 |
| V496 Cen | BER08 | 4.424 | 0.006 | L18 | 0.262 | 2.686 | 5.605 | 2.014 | 0.342 | 0.104 | 0.062 | 0.011 |
| V737 Cen | BER08 | 7.066 | 0.043 | L18 | 0.172 | 3.292 | 5.717 | 5.999 | 0.249 | 0.046 | 0.033 | 0.014 |
| V881 Cen | ASAS-SN | 15.212 | 0.070 | T22 | 0.202 | 2.814 | 0.253 | 0.914 | 0.305 | 0.200 | 0.192 | 0.081 |
| V1253 Cen | ASAS-SN | 4.321 | -0.070 | K22 | 0.305 | 2.720 | 0.022 | 2.126 | 0.391 | 0.182 | 0.074 | 0.013 |
| AK Cep | ASAS-SN | 7.231 | -0.060 | L18 | 0.261 | 3.122 | 5.757 | 3.567 | 0.364 | 0.103 | 0.050 | 0.016 |
| CN Cep | ASAS-SN | 9.504 | -0.041 | L18 | 0.287 | 3.283 | 0.732 | 2.398 | 0.152 | 0.105 | 0.090 | 0.016 |
| CP Cep | BER08 | 17.863 | -0.080 | L18 | 0.344 | 2.662 | 4.418 | 0.835 | 0.175 | 0.127 | 0.116 | 0.021 |
| DR Cep | ASAS-SN | 19.079 | -0.331 | L18 | 0.434 | 3.020 | 5.375 | 1.762 | 0.311 | 0.154 | 0.149 | 0.025 |
| IY Cep | ASAS-SN | 5.658 | -0.011 | L18 | 0.259 | 2.959 | 5.839 | 2.278 | 0.368 | 0.113 | 0.037 | 0.016 |
| MU Cep | ASAS-SN | 3.768 | 0.017 | L18 | 0.278 | 2.644 | 5.402 | 1.874 | 0.337 | 0.136 | 0.051 | 0.013 |
| V901 Cep | ASAS-SN | 8.976 | 0.016 | L18 | 0.320 | 3.232 | 0.480 | 2.040 | 0.186 | 0.127 | 0.115 | 0.013 |
| V911 Cep | ASAS-SN | 4.278 | -0.043 | L18 | 0.251 | 2.739 | 5.597 | 2.173 | 0.382 | 0.156 | 0.050 | 0.018 |
| AX Cir | BER08 | 5.273 | -0.120 | L18 | 0.190 | 2.855 | 5.914 | 3.085 | 0.322 | 0.068 | 0.014 | 0.014 |
| EV Cir | ASAS-SN | 16.707 | 0.270 | K22 | 0.416 | 2.644 | 0.037 | 1.387 | 0.286 | 0.200 | 0.144 | 0.024 |
| FL Cir | ASAS-SN | 10.519 | 0.200 | K22 | 0.227 | 0.682 | 0.088 | 6.180 | 0.046 | 0.075 | 0.017 | 0.018 |
| RW CMa | ASAS-SN | 5.730 | -0.141 | G15 | 0.264 | 3.039 | 5.961 | 2.726 | 0.372 | 0.104 | 0.035 | 0.018 |
| RY CMa | ASAS | 4.678 | 0.069 | G14 | 0.302 | 2.773 | 5.644 | 2.177 | 0.390 | 0.167 | 0.061 | 0.014 |
| RZ CMa | BER08 | 4.255 | -0.102 | L18 | 0.258 | 2.691 | 5.621 | 1.850 | 0.366 | 0.139 | 0.034 | 0.013 |
| SS CMa | ASAS | 12.354 | -0.032 | L18 | 0.388 | 2.692 | 3.664 | 5.511 | 0.161 | 0.122 | 0.101 | 0.015 |
| TV CMa | ASAS | 4.670 | 0.052 | L18 | 0.319 | 2.755 | 5.615 | 1.988 | 0.397 | 0.171 | 0.071 | 0.017 |
| TW CMa | ASAS | 6.995 | -0.031 | G14 | 0.268 | 3.326 | 6.141 | 5.936 | 0.354 | 0.112 | 0.030 | 0.014 |
| VX CMa | ASAS-SN | 2.044 | -0.920 | T22 | 0.318 | 2.322 | 0.059 | 0.962 | 0.525 | 0.363 | 0.193 | 0.055 |
| XZ CMa | ASAS-SN | 2.558 | -0.331 | G14 | 0.351 | 2.536 | 5.236 | 1.583 | 0.502 | 0.290 | 0.174 | 0.028 |
| AO CMa | ASAS-SN | 5.815 | -0.033 | L18 | 0.270 | 3.015 | 5.725 | 2.749 | 0.392 | 0.132 | 0.062 | 0.016 |
| V418 CMa | ASAS-SN | 3.523 | -0.640 | T22 | 0.252 | 2.675 | 0.080 | 2.026 | 0.475 | 0.233 | 0.110 | 0.045 |
| SV Cru | ASAS-SN | 7.006 | 0.100 | K22 | 0.317 | 3.086 | 0.078 | 3.615 | 0.300 | 0.120 | 0.011 | 0.021 |
| VX Cru | ASAS-SN | 12.214 | 0.260 | K22 | 0.360 | 2.551 | 0.033 | 0.224 | 0.238 | 0.136 | 0.100 | 0.012 |
| FQ Cru | ASAS-SN | 13.769 | 0.180 | K22 | 0.320 | 2.775 | 0.062 | 0.736 | 0.232 | 0.138 | 0.124 | 0.019 |
| R Cru | BER08 | 5.826 | 0.036 | L18 | 0.330 | 2.969 | 5.762 | 2.439 | 0.390 | 0.131 | 0.074 | 0.017 |
| S Cru | BER08 | 4.690 | -0.029 | L18 | 0.310 | 2.727 | 5.616 | 2.001 | 0.371 | 0.157 | 0.065 | 0.015 |
| T Cru | BER08 | 6.734 | 0.030 | L18 | 0.215 | 3.290 | 6.245 | 5.822 | 0.287 | 0.041 | 0.018 | 0.018 |
| X Cru | ASAS | 6.220 | 0.055 | L18 | 0.235 | 3.096 | 5.862 | 5.201 | 0.325 | 0.060 | 0.018 | 0.015 |
| VW Cru | BER08 | 5.261 | 0.070 | L18 | 0.256 | 2.829 | 5.717 | 0.509 | 0.346 | 0.088 | 0.006 | 0.018 |
| AD Cru | BER08 | 6.398 | 0.023 | L18 | 0.330 | 2.971 | 5.659 | 1.952 | 0.404 | 0.129 | 0.051 | 0.015 |
| AG Cru | BER08 | 3.837 | -0.065 | L18 | 0.359 | 2.676 | 5.465 | 1.920 | 0.385 | 0.191 | 0.097 | 0.013 |

Continued on next page

Table C.1 – continued from previous page

| Star | Source | Period | [Fe/H] | Ref. | A_1 | ϕ_{21} | ϕ_{31} | ϕ_{41} | R_{21} | R_{31} | R_{41} | σ |
|-------------|---------|--------|--------|------|-------|-------------|-------------|-------------|----------|----------|----------|----------|
| X Cyg | BER08 | 16.387 | 0.059 | L18 | 0.436 | 2.911 | 4.894 | 1.118 | 0.247 | 0.134 | 0.116 | 0.029 |
| SU Cyg | BER08 | 3.846 | -0.098 | L18 | 0.319 | 2.549 | 5.152 | 1.359 | 0.376 | 0.203 | 0.108 | 0.022 |
| SZ Cyg | BER08 | 15.110 | 0.128 | L18 | 0.392 | 2.872 | 4.382 | 0.851 | 0.202 | 0.144 | 0.121 | 0.025 |
| TX Cyg | BER08 | 14.711 | 0.105 | L18 | 0.461 | 2.824 | 4.804 | 1.028 | 0.251 | 0.166 | 0.155 | 0.022 |
| VX Cyg | BER08 | 20.134 | 0.051 | L18 | 0.412 | 2.937 | 4.971 | 1.333 | 0.256 | 0.160 | 0.124 | 0.027 |
| VY Cyg | BER08 | 7.857 | -0.094 | L18 | 0.361 | 3.528 | 0.347 | 1.429 | 0.251 | 0.192 | 0.104 | 0.022 |
| VZ Cyg | BER08 | 4.864 | -0.087 | L18 | 0.286 | 2.813 | 5.697 | 1.995 | 0.371 | 0.119 | 0.024 | 0.018 |
| BZ Cyg | BER08 | 10.141 | 0.075 | L18 | 0.244 | 3.801 | 1.075 | 3.215 | 0.174 | 0.062 | 0.062 | 0.022 |
| CD Cyg | BER08 | 17.075 | 0.124 | L18 | 0.482 | 2.966 | 5.170 | 1.543 | 0.283 | 0.157 | 0.138 | 0.023 |
| EP Cyg | ASAS-SN | 4.289 | -0.186 | L18 | 0.303 | 2.749 | 5.609 | 2.122 | 0.427 | 0.206 | 0.095 | 0.019 |
| EU Cyg | ASAS-SN | 14.984 | -0.238 | L18 | 0.335 | 2.926 | 4.784 | 1.179 | 0.262 | 0.163 | 0.155 | 0.025 |
| EX Cyg | ASAS-SN | 4.851 | 0.119 | L18 | 0.253 | 2.699 | 5.457 | 1.793 | 0.373 | 0.167 | 0.062 | 0.012 |
| EZ Cyg | ASAS-SN | 11.661 | 0.215 | L18 | 0.352 | 2.527 | 3.740 | 0.193 | 0.117 | 0.123 | 0.103 | 0.012 |
| GH Cyg | BER08 | 7.818 | 0.096 | L18 | 0.339 | 3.319 | 6.282 | 1.139 | 0.282 | 0.166 | 0.099 | 0.023 |
| GI Cyg | ASAS-SN | 5.782 | 0.168 | L18 | 0.266 | 2.919 | 5.759 | 2.193 | 0.358 | 0.102 | 0.035 | 0.011 |
| GL Cyg | ASAS-SN | 3.371 | -0.042 | L18 | 0.264 | 2.591 | 5.382 | 1.716 | 0.373 | 0.188 | 0.102 | 0.022 |
| IY Cyg | ASAS-SN | 21.756 | -0.231 | L18 | 0.457 | 2.887 | 5.566 | 2.209 | 0.376 | 0.270 | 0.200 | 0.020 |
| KX Cyg | ASAS-SN | 20.061 | 0.083 | L18 | 0.439 | 2.860 | 5.175 | 1.516 | 0.287 | 0.158 | 0.130 | 0.021 |
| MW Cyg | BER08 | 5.955 | -0.010 | L18 | 0.302 | 3.026 | 5.822 | 2.998 | 0.395 | 0.125 | 0.057 | 0.025 |
| V347 Cyg | ASAS-SN | 8.736 | 0.125 | L18 | 0.310 | 3.549 | 0.973 | 2.449 | 0.169 | 0.147 | 0.116 | 0.013 |
| V356 Cyg | BER08 | 5.057 | 0.087 | L18 | 0.330 | 2.741 | 5.581 | 1.906 | 0.354 | 0.139 | 0.071 | 0.018 |
| V383 Cyg | ASAS-SN | 4.613 | 0.170 | R21 | 0.237 | 2.580 | 5.478 | 1.552 | 0.298 | 0.135 | 0.035 | 0.018 |
| V386 Cyg | BER08 | 5.278 | -0.030 | L18 | 0.295 | 2.915 | 5.719 | 1.933 | 0.364 | 0.108 | 0.032 | 0.023 |
| V396 Cyg | ASAS-SN | 33.246 | 0.063 | L18 | 0.375 | 2.810 | 5.539 | 2.264 | 0.334 | 0.188 | 0.097 | 0.023 |
| V402 Cyg | BER08 | 4.365 | -0.020 | L18 | 0.252 | 2.695 | 5.604 | 2.008 | 0.354 | 0.125 | 0.029 | 0.012 |
| V438 Cyg | BER08 | 11.211 | 0.190 | L18 | 0.403 | 2.691 | 3.885 | 0.087 | 0.146 | 0.122 | 0.124 | 0.018 |
| V459 Cyg | ASAS-SN | 7.251 | 0.025 | L18 | 0.293 | 3.396 | 6.137 | 0.310 | 0.354 | 0.147 | 0.034 | 0.046 |
| V492 Cyg | ASAS-SN | 7.578 | 0.103 | L18 | 0.208 | 3.491 | 6.012 | 0.842 | 0.282 | 0.063 | 0.061 | 0.013 |
| V514 Cyg | ASAS-SN | 5.099 | 0.072 | L18 | 0.322 | 2.821 | 5.616 | 1.953 | 0.385 | 0.158 | 0.071 | 0.016 |
| V520 Cyg | ASAS-SN | 4.049 | -0.025 | L18 | 0.256 | 2.691 | 5.452 | 1.843 | 0.315 | 0.123 | 0.046 | 0.014 |
| V538 Cyg | BER08 | 6.119 | -0.046 | L18 | 0.231 | 3.108 | 5.686 | 6.159 | 0.301 | 0.089 | 0.019 | 0.026 |
| V547 Cyg | ASAS-SN | 6.226 | 0.108 | L18 | 0.349 | 2.974 | 5.446 | 2.256 | 0.378 | 0.140 | 0.076 | 0.017 |
| V609 Cyg | ASAS-SN | 31.111 | 0.162 | L18 | 0.428 | 2.949 | 6.025 | 2.887 | 0.446 | 0.281 | 0.153 | 0.019 |
| V621 Cyg | BER08 | 5.864 | -0.025 | L18 | 0.379 | 2.945 | 5.342 | 2.062 | 0.409 | 0.170 | 0.053 | 0.021 |
| V1020 Cyg | ASAS-SN | 4.921 | 0.154 | L18 | 0.288 | 2.771 | 5.483 | 1.564 | 0.391 | 0.153 | 0.058 | 0.022 |
| V1025 Cyg | ASAS-SN | 6.961 | 0.151 | L18 | 0.250 | 3.166 | 5.703 | 4.572 | 0.359 | 0.116 | 0.022 | 0.016 |
| V1033 Cyg | ASAS-SN | 4.953 | 0.034 | L18 | 0.225 | 2.550 | 5.325 | 1.750 | 0.371 | 0.158 | 0.071 | 0.022 |
| V1046 Cyg | ASAS-SN | 4.945 | 0.110 | L18 | 0.250 | 2.784 | 5.754 | 1.818 | 0.300 | 0.108 | 0.029 | 0.023 |
| V1154 Cyg | BER08 | 4.925 | -0.148 | L18 | 0.175 | 2.733 | 5.618 | 1.517 | 0.280 | 0.069 | 0.021 | 0.016 |
| V1364 Cyg | ASAS-SN | 12.972 | 0.193 | L18 | 0.310 | 2.240 | 3.799 | 0.329 | 0.117 | 0.142 | 0.096 | 0.015 |
| V1397 Cyg | ASAS-SN | 4.639 | -0.031 | L18 | 0.253 | 2.766 | 5.516 | 2.085 | 0.351 | 0.122 | 0.045 | 0.022 |
| V1788 Cyg | ASAS-SN | 14.091 | 0.370 | R21 | 0.341 | 2.575 | 4.049 | 0.377 | 0.175 | 0.133 | 0.100 | 0.024 |
| V2475 Cyg | ASAS-SN | 11.557 | 0.250 | R21 | 0.376 | 2.614 | 4.114 | 6.228 | 0.194 | 0.151 | 0.108 | 0.021 |
| β Dor | BER08 | 9.843 | -0.056 | L18 | 0.270 | 5.008 | 2.959 | 5.334 | 0.057 | 0.103 | 0.057 | 0.020 |
| W Gem | ASAS | 7.914 | -0.080 | L18 | 0.346 | 3.471 | 0.151 | 1.656 | 0.289 | 0.215 | 0.096 | 0.016 |
| RZ Gem | ASAS | 5.529 | -0.226 | L18 | 0.374 | 2.729 | 5.568 | 2.117 | 0.437 | 0.218 | 0.127 | 0.022 |
| AA Gem | ASAS | 11.301 | -0.222 | L18 | 0.266 | 1.370 | 3.492 | 0.117 | 0.062 | 0.136 | 0.086 | 0.018 |
| AD Gem | ASAS | 3.788 | -0.216 | L18 | 0.261 | 2.670 | 5.307 | 1.977 | 0.397 | 0.187 | 0.072 | 0.025 |
| BB Gem | ASAS-SN | 2.308 | -0.185 | L18 | 0.397 | 2.497 | 5.108 | 1.446 | 0.462 | 0.230 | 0.126 | 0.010 |
| BW Gem | ASAS-SN | 2.635 | -0.246 | L18 | 0.311 | 2.556 | 5.252 | 1.488 | 0.462 | 0.261 | 0.125 | 0.028 |
| BB Her | BER08 | 7.441 | 0.159 | L18 | 0.282 | 3.379 | 6.123 | 0.964 | 0.281 | 0.095 | 0.055 | 0.023 |
| V Lac | BER08 | 4.983 | -0.022 | L18 | 0.393 | 2.707 | 5.445 | 1.949 | 0.406 | 0.191 | 0.089 | 0.022 |
| Y Lac | BER08 | 4.324 | -0.090 | L18 | 0.306 | 2.676 | 5.477 | 1.897 | 0.375 | 0.131 | 0.065 | 0.023 |
| Z Lac | BER08 | 10.886 | -0.005 | L18 | 0.377 | 2.828 | 3.667 | 6.087 | 0.112 | 0.132 | 0.126 | 0.017 |
| RR Lac | BER08 | 6.416 | -0.040 | L18 | 0.344 | 2.973 | 5.489 | 2.198 | 0.349 | 0.115 | 0.059 | 0.019 |
| BG Lac | BER08 | 5.332 | -0.041 | L18 | 0.251 | 2.899 | 5.771 | 2.375 | 0.361 | 0.168 | 0.056 | 0.024 |
| DF Lac | ASAS-SN | 4.479 | -0.076 | G14 | 0.255 | 2.764 | 5.677 | 2.202 | 0.362 | 0.136 | 0.046 | 0.015 |
| SV Mon | ASAS | 15.237 | -0.029 | L18 | 0.451 | 3.029 | 4.899 | 1.132 | 0.231 | 0.119 | 0.130 | 0.019 |
| TW Mon | BER08 | 7.143 | -0.227 | L18 | 0.231 | 3.289 | 0.032 | 0.601 | 0.324 | 0.113 | 0.048 | 0.019 |
| TX Mon | BER08 | 8.702 | -0.103 | L18 | 0.287 | 3.908 | 1.169 | 2.974 | 0.211 | 0.124 | 0.098 | 0.020 |
| TY Mon | BER08 | 4.023 | -0.135 | L18 | 0.254 | 2.726 | 5.659 | 2.000 | 0.377 | 0.154 | 0.084 | 0.021 |

Continued on next page

Table C.1 – continued from previous page

| Star | Source | Period | [Fe/H] | Ref. | A_1 | ϕ_{21} | ϕ_{31} | ϕ_{41} | R_{21} | R_{31} | R_{41} | σ |
|-----------|---------|--------|--------|------|-------|-------------|-------------|-------------|----------|----------|----------|----------|
| TZ Mon | BER08 | 7.428 | -0.094 | L18 | 0.306 | 3.467 | 0.158 | 1.088 | 0.328 | 0.155 | 0.064 | 0.020 |
| VZ Mon | ASAS-SN | 5.091 | -0.158 | L18 | 0.229 | 2.963 | 6.041 | 2.740 | 0.389 | 0.137 | 0.030 | 0.021 |
| WW Mon | ASAS-SN | 4.662 | -0.253 | L18 | 0.362 | 2.858 | 5.816 | 2.347 | 0.480 | 0.232 | 0.131 | 0.024 |
| XX Mon | ASAS-SN | 5.456 | -0.087 | L18 | 0.300 | 2.958 | 5.821 | 2.104 | 0.398 | 0.135 | 0.061 | 0.029 |
| YY Mon | ASAS-SN | 3.454 | -0.426 | L18 | 0.353 | 2.645 | 5.503 | 1.870 | 0.492 | 0.312 | 0.185 | 0.042 |
| AA Mon | ASAS-SN | 3.938 | -0.181 | L18 | 0.277 | 2.730 | 5.620 | 2.107 | 0.413 | 0.195 | 0.091 | 0.027 |
| AC Mon | ASAS | 8.015 | -0.132 | L18 | 0.302 | 3.718 | 0.592 | 2.117 | 0.276 | 0.188 | 0.090 | 0.014 |
| BE Mon | BER08 | 2.706 | -0.041 | L18 | 0.256 | 2.621 | 5.300 | 1.790 | 0.342 | 0.157 | 0.067 | 0.023 |
| BV Mon | ASAS-SN | 3.014 | -0.136 | L18 | 0.324 | 2.611 | 5.273 | 1.608 | 0.421 | 0.216 | 0.120 | 0.009 |
| CS Mon | BER08 | 6.732 | -0.196 | L18 | 0.230 | 3.211 | 0.154 | 3.780 | 0.313 | 0.076 | 0.023 | 0.019 |
| CU Mon | ASAS-SN | 4.708 | -0.234 | L18 | 0.275 | 2.886 | 5.855 | 2.679 | 0.458 | 0.200 | 0.090 | 0.038 |
| CV Mon | ASAS | 5.379 | -0.091 | L18 | 0.264 | 2.875 | 5.876 | 2.163 | 0.394 | 0.128 | 0.065 | 0.020 |
| EE Mon | BER08 | 4.809 | -0.467 | L18 | 0.371 | 2.894 | 5.797 | 2.182 | 0.426 | 0.184 | 0.068 | 0.028 |
| EK Mon | BER08 | 3.958 | -0.043 | L18 | 0.246 | 2.575 | 5.339 | 1.645 | 0.307 | 0.101 | 0.024 | 0.015 |
| FG Mon | ASAS-SN | 4.497 | -0.184 | L18 | 0.252 | 2.703 | 5.454 | 1.866 | 0.467 | 0.228 | 0.131 | 0.015 |
| FI Mon | ASAS-SN | 3.288 | -0.206 | L18 | 0.273 | 2.618 | 5.403 | 1.796 | 0.427 | 0.211 | 0.101 | 0.017 |
| FT Mon | BER08 | 3.422 | -0.296 | L18 | 0.419 | 2.617 | 5.243 | 1.753 | 0.464 | 0.254 | 0.134 | 0.038 |
| V446 Mon | ASAS-SN | 1.919 | -0.386 | L18 | 0.303 | 2.467 | 5.093 | 1.418 | 0.499 | 0.331 | 0.204 | 0.040 |
| V447 Mon | BER08 | 2.484 | -0.316 | L18 | 0.320 | 2.621 | 5.401 | 1.993 | 0.476 | 0.245 | 0.156 | 0.028 |
| V484 Mon | ASAS-SN | 3.136 | -0.152 | L18 | 0.222 | 2.476 | 5.168 | 1.163 | 0.414 | 0.196 | 0.099 | 0.032 |
| V495 Mon | ASAS-SN | 4.097 | -0.211 | L18 | 0.227 | 2.737 | 5.702 | 2.391 | 0.380 | 0.153 | 0.038 | 0.023 |
| V508 Mon | BER08 | 4.134 | -0.214 | L18 | 0.190 | 2.683 | 5.350 | 2.156 | 0.305 | 0.136 | 0.021 | 0.014 |
| V510 Mon | ASAS-SN | 7.457 | -0.201 | L18 | 0.165 | 3.446 | 6.198 | 0.694 | 0.265 | 0.029 | 0.019 | 0.012 |
| V911 Mon | ASAS-SN | 4.978 | -0.129 | L18 | 0.224 | 2.876 | 5.680 | 4.548 | 0.350 | 0.098 | 0.011 | 0.023 |
| RT Mus | ASAS | 3.086 | -0.019 | L18 | 0.324 | 2.581 | 5.202 | 1.588 | 0.370 | 0.172 | 0.084 | 0.017 |
| TZ Mus | BER08 | 4.945 | -0.011 | L18 | 0.292 | 2.801 | 5.787 | 2.245 | 0.314 | 0.118 | 0.071 | 0.013 |
| UU Mus | ASAS | 11.635 | 0.079 | L18 | 0.416 | 2.829 | 4.260 | 0.327 | 0.192 | 0.136 | 0.147 | 0.015 |
| S Nor | BER08 | 9.755 | 0.074 | L18 | 0.286 | 4.611 | 2.501 | 4.653 | 0.076 | 0.096 | 0.057 | 0.016 |
| U Nor | ASAS | 12.644 | 0.089 | L18 | 0.400 | 2.558 | 3.973 | 6.030 | 0.171 | 0.126 | 0.102 | 0.017 |
| RS Nor | ASAS | 6.198 | 0.194 | L18 | 0.318 | 3.042 | 5.726 | 2.811 | 0.386 | 0.118 | 0.045 | 0.018 |
| SY Nor | ASAS | 12.646 | 0.202 | L18 | 0.352 | 2.582 | 4.041 | 0.703 | 0.176 | 0.133 | 0.113 | 0.039 |
| TW Nor | BER08 | 10.786 | 0.201 | L18 | 0.363 | 2.767 | 3.309 | 5.585 | 0.060 | 0.117 | 0.090 | 0.021 |
| GU Nor | BER08 | 3.453 | 0.152 | L18 | 0.248 | 2.533 | 5.051 | 0.660 | 0.308 | 0.097 | 0.061 | 0.015 |
| IQ Nor | BER08 | 8.274 | 0.149 | G15 | 0.269 | 4.146 | 5.808 | 3.430 | 0.181 | 0.084 | 0.080 | 0.056 |
| V340 Nor | BER08 | 11.289 | 0.054 | L18 | 0.140 | 4.662 | 0.217 | 1.735 | 0.188 | 0.082 | 0.073 | 0.018 |
| V397 Nor | ASAS-SN | 6.813 | 0.230 | K22 | 0.232 | 3.081 | 0.106 | 5.803 | 0.289 | 0.072 | 0.012 | 0.018 |
| BF Oph | BER08 | 4.068 | -0.003 | L18 | 0.286 | 2.641 | 5.448 | 2.018 | 0.350 | 0.150 | 0.056 | 0.022 |
| RS Ori | ASAS | 7.569 | -0.050 | L18 | 0.355 | 3.430 | 6.193 | 0.876 | 0.273 | 0.179 | 0.060 | 0.022 |
| CR Ori | BER08 | 4.910 | -0.190 | L18 | 0.276 | 2.998 | 5.918 | 2.163 | 0.355 | 0.122 | 0.072 | 0.011 |
| CS Ori | ASAS-SN | 3.889 | -0.321 | G14 | 0.371 | 2.599 | 5.268 | 1.550 | 0.413 | 0.227 | 0.123 | 0.021 |
| DF Ori | ASAS-SN | 3.181 | -0.334 | L18 | 0.289 | 2.640 | 5.347 | 1.591 | 0.465 | 0.284 | 0.139 | 0.027 |
| V1819 Ori | ASAS-SN | 3.150 | -0.850 | T22 | 0.234 | 2.737 | 0.064 | 1.987 | 0.351 | 0.138 | 0.056 | 0.024 |
| SV Per | BER08 | 11.129 | -0.092 | L18 | 0.331 | 3.007 | 3.847 | 0.199 | 0.117 | 0.109 | 0.142 | 0.022 |
| SX Per | ASAS-SN | 4.291 | -0.155 | L18 | 0.300 | 2.754 | 5.527 | 1.997 | 0.407 | 0.206 | 0.088 | 0.036 |
| UX Per | ASAS-SN | 4.566 | -0.105 | L18 | 0.226 | 2.561 | 5.245 | 1.573 | 0.429 | 0.205 | 0.118 | 0.012 |
| UY Per | BER08 | 5.363 | 0.066 | L18 | 0.376 | 2.784 | 5.463 | 1.465 | 0.372 | 0.169 | 0.079 | 0.043 |
| VX Per | BER08 | 10.886 | -0.076 | L18 | 0.303 | 4.001 | 1.646 | 3.382 | 0.122 | 0.118 | 0.094 | 0.014 |
| VY Per | ASAS-SN | 5.532 | -0.028 | L18 | 0.343 | 2.840 | 5.652 | 2.014 | 0.398 | 0.146 | 0.078 | 0.021 |
| BM Per | BER08 | 22.960 | 0.063 | L18 | 0.482 | 3.018 | 5.779 | 2.456 | 0.385 | 0.246 | 0.178 | 0.029 |
| DW Per | ASAS-SN | 3.650 | -0.098 | L18 | 0.286 | 2.625 | 5.415 | 1.804 | 0.348 | 0.159 | 0.079 | 0.013 |
| HQ Per | ASAS-SN | 8.637 | -0.432 | L18 | 0.203 | 3.720 | 0.487 | 1.378 | 0.299 | 0.095 | 0.035 | 0.015 |
| HZ Per | ASAS-SN | 11.282 | -0.316 | L18 | 0.330 | 3.018 | 4.123 | 0.847 | 0.163 | 0.129 | 0.147 | 0.021 |
| MM Per | ASAS-SN | 4.118 | -0.137 | L18 | 0.253 | 2.695 | 5.443 | 2.063 | 0.388 | 0.173 | 0.060 | 0.067 |
| OT Per | ASAS-SN | 26.108 | -0.198 | L18 | 0.397 | 3.095 | 6.089 | 2.811 | 0.391 | 0.229 | 0.146 | 0.026 |
| V598 Per | ASAS-SN | 5.667 | -0.070 | R21 | 0.335 | 2.880 | 5.916 | 2.547 | 0.389 | 0.137 | 0.060 | 0.036 |
| V891 Per | ASAS-SN | 3.220 | -0.051 | L18 | 0.196 | 2.496 | 5.324 | 0.017 | 0.328 | 0.142 | 0.036 | 0.050 |
| X Pup | BER08 | 25.968 | -0.028 | L18 | 0.494 | 3.006 | 5.999 | 2.824 | 0.438 | 0.295 | 0.190 | 0.020 |
| RS Pup | BER08 | 41.510 | 0.187 | L18 | 0.449 | 3.223 | 0.164 | 3.210 | 0.446 | 0.203 | 0.105 | 0.028 |
| VW Pup | ASAS-SN | 4.285 | -0.211 | G14 | 0.278 | 2.801 | 5.745 | 2.200 | 0.436 | 0.205 | 0.084 | 0.019 |
| VZ Pup | ASAS | 23.171 | -0.200 | L18 | 0.490 | 2.889 | 5.749 | 2.535 | 0.408 | 0.289 | 0.199 | 0.020 |
| WW Pup | ASAS | 5.516 | 0.059 | G14 | 0.351 | 2.974 | 5.689 | 2.350 | 0.436 | 0.180 | 0.090 | 0.039 |

Continued on next page

Table C.1 – continued from previous page

| Star | Source | Period | [Fe/H] | Ref. | A_1 | ϕ_{21} | ϕ_{31} | ϕ_{41} | R_{21} | R_{31} | R_{41} | σ |
|-----------|---------|--------|--------|------|-------|-------------|-------------|-------------|----------|----------|----------|----------|
| WX Pup | BER08 | 8.900 | -0.109 | L18 | 0.305 | 3.570 | 0.199 | 1.516 | 0.265 | 0.185 | 0.099 | 0.016 |
| WY Pup | BER08 | 5.213 | -0.171 | G15 | 0.313 | 2.900 | 5.923 | 2.881 | 0.454 | 0.182 | 0.107 | 0.016 |
| WZ Pup | BER08 | 5.016 | -0.141 | G15 | 0.336 | 2.817 | 5.619 | 1.895 | 0.421 | 0.182 | 0.071 | 0.017 |
| AD Pup | ASAS | 13.596 | -0.124 | L18 | 0.417 | 3.019 | 4.640 | 0.878 | 0.221 | 0.129 | 0.151 | 0.014 |
| AP Pup | BER08 | 5.084 | -0.027 | L18 | 0.277 | 2.851 | 5.834 | 2.211 | 0.352 | 0.121 | 0.041 | 0.014 |
| AQ Pup | ASAS | 30.142 | 0.019 | L18 | 0.435 | 2.876 | 5.641 | 2.270 | 0.392 | 0.264 | 0.192 | 0.011 |
| AT Pup | BER08 | 6.665 | -0.054 | L18 | 0.375 | 3.248 | 5.757 | 3.291 | 0.390 | 0.189 | 0.024 | 0.014 |
| BC Pup | BER08 | 3.544 | -0.381 | G14 | 0.349 | 2.754 | 5.727 | 1.872 | 0.507 | 0.265 | 0.151 | 0.028 |
| BM Pup | ASAS | 7.198 | -0.141 | G15 | 0.310 | 3.188 | 5.836 | 1.104 | 0.319 | 0.224 | 0.042 | 0.030 |
| BN Pup | ASAS | 13.673 | -0.002 | L18 | 0.470 | 3.091 | 5.171 | 1.416 | 0.274 | 0.144 | 0.152 | 0.015 |
| CE Pup | ASAS-SN | 49.410 | -0.066 | L18 | 0.370 | 3.552 | 0.616 | 3.480 | 0.311 | 0.089 | 0.025 | 0.022 |
| CK Pup | BER08 | 7.412 | -0.201 | G14 | 0.363 | 3.461 | 0.162 | 1.761 | 0.294 | 0.233 | 0.133 | 0.035 |
| HW Pup | ASAS-SN | 13.460 | -0.264 | L18 | 0.407 | 2.849 | 4.613 | 0.729 | 0.275 | 0.185 | 0.184 | 0.018 |
| LS Pup | BER08 | 14.148 | -0.191 | G14 | 0.394 | 2.979 | 4.484 | 0.937 | 0.163 | 0.140 | 0.147 | 0.033 |
| NT Pup | ASAS-SN | 15.561 | -0.167 | L18 | 0.394 | 3.044 | 5.524 | 1.864 | 0.312 | 0.152 | 0.139 | 0.017 |
| OO Pup | ASAS-SN | 10.983 | -0.180 | R21 | 0.249 | 5.087 | 2.765 | 5.277 | 0.074 | 0.116 | 0.069 | 0.015 |
| V620 Pup | ASAS-SN | 2.586 | -0.140 | K22 | 0.221 | 2.465 | 0.078 | 0.645 | 0.353 | 0.130 | 0.060 | 0.021 |
| V629 Pup | ASAS-SN | 4.175 | -0.120 | K22 | 0.331 | 2.753 | 0.076 | 2.086 | 0.396 | 0.202 | 0.083 | 0.041 |
| V729 Pup | ASAS-SN | 4.089 | -0.060 | K22 | 0.205 | 2.638 | 0.091 | 2.424 | 0.351 | 0.124 | 0.026 | 0.020 |
| V731 Pup | ASAS-SN | 5.464 | -0.180 | K22 | 0.245 | 2.794 | 0.101 | 1.567 | 0.331 | 0.117 | 0.018 | 0.025 |
| DU Pyx | ASAS-SN | 3.707 | 0.010 | K22 | 0.259 | 2.615 | 0.022 | 1.820 | 0.348 | 0.154 | 0.066 | 0.011 |
| DX Pyx | ASAS-SN | 3.737 | -0.130 | K22 | 0.256 | 2.679 | 0.041 | 1.878 | 0.373 | 0.163 | 0.072 | 0.022 |
| RV Sco | BER08 | 6.062 | 0.042 | L18 | 0.333 | 3.061 | 5.722 | 2.564 | 0.393 | 0.139 | 0.065 | 0.017 |
| RY Sco | BER08 | 20.317 | 0.037 | L18 | 0.364 | 2.686 | 5.398 | 1.998 | 0.326 | 0.206 | 0.119 | 0.017 |
| KQ Sco | ASAS | 28.714 | 0.317 | L18 | 0.406 | 2.755 | 5.217 | 1.684 | 0.316 | 0.180 | 0.108 | 0.021 |
| V470 Sco | ASAS-SN | 16.257 | 0.089 | G15 | 0.380 | 2.613 | 5.080 | 1.509 | 0.285 | 0.173 | 0.112 | 0.024 |
| V482 Sco | BER08 | 4.528 | 0.070 | L18 | 0.283 | 2.685 | 5.550 | 1.861 | 0.333 | 0.138 | 0.040 | 0.012 |
| V500 Sco | BER08 | 9.327 | -0.059 | L18 | 0.307 | 3.789 | 1.668 | 4.035 | 0.066 | 0.102 | 0.103 | 0.032 |
| V636 Sco | BER08 | 6.797 | 0.021 | L18 | 0.232 | 3.240 | 5.760 | 0.247 | 0.310 | 0.061 | 0.020 | 0.013 |
| V1622 Sco | ASAS-SN | 8.451 | 0.110 | K22 | 0.229 | 3.694 | 0.088 | 1.899 | 0.182 | 0.160 | 0.121 | 0.031 |
| X Sct | ASAS | 4.198 | 0.049 | G15 | 0.359 | 2.637 | 5.364 | 1.828 | 0.372 | 0.164 | 0.080 | 0.013 |
| Y Sct | ASAS | 10.342 | 0.136 | L18 | 0.325 | 2.750 | 3.244 | 5.933 | 0.035 | 0.109 | 0.082 | 0.018 |
| Z Sct | ASAS | 12.901 | 0.207 | L18 | 0.400 | 2.759 | 4.044 | 0.274 | 0.150 | 0.109 | 0.101 | 0.023 |
| RU Sct | ASAS | 19.698 | 0.057 | L18 | 0.449 | 2.764 | 5.309 | 1.807 | 0.314 | 0.227 | 0.174 | 0.018 |
| SS Sct | ASAS | 3.671 | 0.009 | L18 | 0.230 | 2.620 | 5.352 | 1.524 | 0.305 | 0.117 | 0.039 | 0.012 |
| TX Sct | ASAS-SN | 24.348 | 0.110 | R21 | 0.363 | 2.734 | 5.180 | 1.657 | 0.287 | 0.166 | 0.099 | 0.016 |
| TY Sct | ASAS | 11.053 | 0.294 | L18 | 0.381 | 2.418 | 3.797 | 5.619 | 0.148 | 0.108 | 0.085 | 0.021 |
| UZ Sct | ASAS-SN | 14.747 | 0.365 | L18 | 0.348 | 2.472 | 4.105 | 0.268 | 0.214 | 0.136 | 0.100 | 0.024 |
| BX Sct | ASAS-SN | 6.411 | 0.155 | L18 | 0.342 | 3.033 | 5.640 | 2.349 | 0.374 | 0.120 | 0.077 | 0.014 |
| CK Sct | ASAS | 7.416 | 0.103 | L18 | 0.199 | 3.446 | 5.900 | 0.773 | 0.285 | 0.070 | 0.053 | 0.027 |
| CM Sct | ASAS | 3.917 | 0.055 | L18 | 0.226 | 2.524 | 5.439 | 1.644 | 0.338 | 0.138 | 0.040 | 0.028 |
| CN Sct | ASAS-SN | 9.993 | 0.233 | L18 | 0.297 | 2.693 | 2.565 | 3.984 | 0.098 | 0.053 | 0.069 | 0.018 |
| V459 Sct | ASAS | 5.763 | 0.220 | T22 | 0.196 | 2.761 | 0.266 | 2.377 | 0.310 | 0.148 | 0.118 | 0.056 |
| AA Ser | ASAS-SN | 17.142 | 0.384 | L18 | 0.340 | 2.557 | 4.457 | 0.791 | 0.232 | 0.124 | 0.110 | 0.018 |
| CR Ser | ASAS | 5.301 | 0.049 | G15 | 0.315 | 2.876 | 5.745 | 2.206 | 0.399 | 0.149 | 0.068 | 0.018 |
| DV Ser | BER08 | 23.131 | 0.366 | L18 | 0.400 | 2.536 | 5.375 | 2.604 | 0.393 | 0.173 | 0.123 | 0.029 |
| V536 Ser | ASAS-SN | 9.010 | 0.110 | R21 | 0.238 | 4.444 | 1.604 | 2.543 | 0.108 | 0.050 | 0.033 | 0.035 |
| S Sge | BER08 | 8.383 | 0.051 | L18 | 0.323 | 3.635 | 0.524 | 1.952 | 0.215 | 0.165 | 0.105 | 0.029 |
| DG Sge | ASAS-SN | 4.437 | 0.052 | L18 | 0.311 | 2.718 | 5.414 | 1.807 | 0.383 | 0.156 | 0.055 | 0.017 |
| GX Sge | ASAS-SN | 12.898 | 0.177 | L18 | 0.423 | 2.815 | 4.354 | 0.648 | 0.200 | 0.122 | 0.126 | 0.018 |
| GY Sge | ASAS | 51.561 | 0.163 | L18 | 0.285 | 3.179 | 6.103 | 3.367 | 0.289 | 0.107 | 0.051 | 0.017 |
| V355 Sge | ASAS-SN | 32.051 | 0.030 | R21 | 0.288 | 2.691 | 5.304 | 1.688 | 0.293 | 0.146 | 0.070 | 0.019 |
| U Sgr | BER08 | 6.745 | 0.036 | L18 | 0.307 | 3.247 | 5.801 | 4.541 | 0.365 | 0.130 | 0.024 | 0.026 |
| W Sgr | BER08 | 7.595 | -0.032 | L18 | 0.338 | 3.451 | 6.238 | 1.173 | 0.317 | 0.204 | 0.079 | 0.013 |
| X Sgr | BER08 | 7.013 | -0.321 | L18 | 0.279 | 3.096 | 5.699 | 2.972 | 0.294 | 0.110 | 0.017 | 0.017 |
| Y Sgr | BER08 | 5.774 | 0.018 | L18 | 0.307 | 2.943 | 5.712 | 2.188 | 0.357 | 0.103 | 0.042 | 0.026 |
| VY Sgr | ASAS-SN | 13.560 | 0.263 | L18 | 0.425 | 2.815 | 4.512 | 0.800 | 0.233 | 0.131 | 0.120 | 0.016 |
| WZ Sgr | ASAS | 21.853 | 0.243 | L18 | 0.470 | 2.791 | 5.139 | 1.516 | 0.310 | 0.155 | 0.122 | 0.018 |
| XX Sgr | ASAS | 6.424 | 0.031 | L18 | 0.355 | 3.069 | 5.572 | 2.684 | 0.366 | 0.156 | 0.059 | 0.014 |
| YZ Sgr | ASAS | 9.553 | 0.051 | L18 | 0.293 | 4.253 | 2.117 | 3.910 | 0.109 | 0.096 | 0.068 | 0.015 |
| AV Sgr | ASAS-SN | 15.412 | 0.421 | L18 | 0.462 | 2.774 | 4.875 | 1.155 | 0.248 | 0.160 | 0.121 | 0.029 |

Continued on next page

Table C.1 – continued from previous page

| Star | Source | Period | [Fe/H] | Ref. | A_1 | ϕ_{21} | ϕ_{31} | ϕ_{41} | R_{21} | R_{31} | R_{41} | σ |
|--------------------|---------|--------|--------|------|-------|-------------|-------------|-------------|----------|----------|----------|----------|
| AP Sgr | BER08 | 5.058 | 0.090 | L18 | 0.330 | 2.834 | 5.725 | 2.160 | 0.404 | 0.165 | 0.073 | 0.029 |
| AY Sgr | BER08 | 6.569 | 0.039 | G15 | 0.366 | 3.177 | 5.670 | 2.200 | 0.378 | 0.134 | 0.065 | 0.042 |
| BB Sgr | BER08 | 6.637 | 0.044 | L18 | 0.254 | 3.280 | 5.975 | 0.292 | 0.345 | 0.089 | 0.032 | 0.025 |
| V350 Sgr | ASAS | 5.155 | 0.077 | L18 | 0.296 | 2.802 | 5.672 | 2.044 | 0.368 | 0.144 | 0.050 | 0.014 |
| V773 Sgr | ASAS-SN | 5.749 | 0.039 | G15 | 0.302 | 2.934 | 5.729 | 2.488 | 0.367 | 0.124 | 0.060 | 0.024 |
| V1954 Sgr | ASAS | 6.178 | 0.169 | G15 | 0.298 | 2.962 | 5.872 | 2.363 | 0.357 | 0.098 | 0.026 | 0.023 |
| V5567 Sgr | ASAS | 9.761 | 0.029 | L18 | 0.240 | 3.313 | 0.647 | 2.716 | 0.169 | 0.118 | 0.112 | 0.056 |
| ST Tau | ASAS | 4.034 | -0.091 | L18 | 0.327 | 2.698 | 5.369 | 1.929 | 0.383 | 0.177 | 0.081 | 0.014 |
| AE Tau | ASAS-SN | 3.897 | -0.235 | L18 | 0.237 | 2.694 | 5.533 | 2.096 | 0.417 | 0.190 | 0.076 | 0.010 |
| AV Tau | ASAS-SN | 3.616 | -0.167 | L18 | 0.303 | 2.578 | 5.270 | 1.726 | 0.416 | 0.222 | 0.116 | 0.011 |
| EF Tau | ASAS-SN | 3.448 | -0.751 | G14 | 0.246 | 2.677 | 5.459 | 1.853 | 0.486 | 0.276 | 0.129 | 0.025 |
| R Tra | BER08 | 3.389 | 0.023 | L18 | 0.252 | 2.566 | 5.240 | 1.604 | 0.305 | 0.122 | 0.044 | 0.013 |
| S Tra | BER08 | 6.324 | 0.090 | L18 | 0.314 | 3.117 | 5.757 | 2.951 | 0.373 | 0.123 | 0.034 | 0.014 |
| T Vel | BER08 | 4.640 | -0.067 | L18 | 0.263 | 2.783 | 5.704 | 2.224 | 0.381 | 0.149 | 0.042 | 0.011 |
| V Vel | BER08 | 4.371 | -0.184 | L18 | 0.281 | 2.788 | 5.714 | 2.196 | 0.405 | 0.179 | 0.071 | 0.011 |
| RY Vel | BER08 | 28.141 | 0.033 | L18 | 0.397 | 2.884 | 5.920 | 2.711 | 0.401 | 0.234 | 0.108 | 0.015 |
| RZ Vel | BER08 | 20.399 | 0.018 | L18 | 0.504 | 2.862 | 5.471 | 2.094 | 0.352 | 0.244 | 0.185 | 0.018 |
| ST Vel | ASAS | 5.858 | -0.021 | L18 | 0.281 | 3.069 | 6.038 | 2.916 | 0.391 | 0.108 | 0.035 | 0.012 |
| SV Vel | BER08 | 14.097 | 0.020 | L18 | 0.448 | 2.787 | 4.875 | 1.109 | 0.274 | 0.185 | 0.153 | 0.015 |
| SW Vel | BER08 | 23.416 | -0.069 | L18 | 0.485 | 3.017 | 5.956 | 2.716 | 0.428 | 0.285 | 0.196 | 0.016 |
| SX Vel | ASAS | 9.550 | -0.038 | L18 | 0.343 | 3.188 | 1.336 | 2.928 | 0.130 | 0.101 | 0.098 | 0.009 |
| XX Vel | BER08 | 6.984 | -0.016 | L18 | 0.357 | 3.165 | 5.756 | 4.566 | 0.371 | 0.207 | 0.025 | 0.030 |
| AE Vel | ASAS | 7.134 | 0.017 | L18 | 0.337 | 3.164 | 5.662 | 2.895 | 0.346 | 0.174 | 0.020 | 0.022 |
| BG Vel | BER08 | 6.924 | -0.043 | L18 | 0.201 | 3.311 | 6.101 | 6.044 | 0.274 | 0.041 | 0.036 | 0.013 |
| BQ Vel | ASAS | 3.373 | -0.500 | T22 | 0.224 | 2.642 | 0.080 | 1.568 | 0.479 | 0.308 | 0.159 | 0.035 |
| CP Vel | ASAS-SN | 9.843 | 0.017 | L18 | 0.270 | 4.641 | 3.266 | 5.883 | 0.030 | 0.105 | 0.070 | 0.020 |
| CS Vel | ASAS-SN | 5.906 | 0.019 | G14 | 0.297 | 2.980 | 5.796 | 2.497 | 0.367 | 0.110 | 0.058 | 0.015 |
| CX Vel | ASAS-SN | 6.256 | 0.038 | L18 | 0.278 | 3.120 | 5.784 | 3.150 | 0.361 | 0.104 | 0.026 | 0.014 |
| DR Vel | ASAS | 11.199 | 0.071 | L18 | 0.322 | 1.907 | 3.459 | 0.078 | 0.048 | 0.127 | 0.073 | 0.014 |
| EX Vel | ASAS-SN | 13.234 | -0.019 | L18 | 0.310 | 2.086 | 3.528 | 0.056 | 0.052 | 0.130 | 0.073 | 0.013 |
| FG Vel | ASAS-SN | 6.454 | -0.091 | L18 | 0.227 | 3.197 | 6.024 | 5.096 | 0.340 | 0.072 | 0.033 | 0.013 |
| FN Vel | BER08 | 5.325 | 0.047 | L18 | 0.259 | 2.807 | 5.655 | 1.641 | 0.339 | 0.113 | 0.042 | 0.019 |
| V530 Vel | ASAS-SN | 3.591 | -0.280 | K22 | 0.193 | 2.628 | 0.064 | 1.719 | 0.329 | 0.115 | 0.044 | 0.018 |
| V536 Vel | ASAS-SN | 7.645 | 0.060 | K22 | 0.251 | 3.578 | 0.063 | 1.271 | 0.300 | 0.111 | 0.077 | 0.016 |
| S Vul | BER08 | 68.580 | 0.059 | L18 | 0.262 | 3.354 | 0.238 | 3.419 | 0.298 | 0.097 | 0.023 | 0.052 |
| T Vul | BER08 | 4.435 | -0.078 | L18 | 0.278 | 2.825 | 5.655 | 1.926 | 0.345 | 0.137 | 0.044 | 0.031 |
| U Vul | ASAS | 7.989 | 0.052 | L18 | 0.323 | 3.288 | 6.110 | 1.378 | 0.212 | 0.143 | 0.057 | 0.019 |
| X Vul | BER08 | 6.320 | 0.046 | L18 | 0.325 | 3.110 | 5.664 | 2.656 | 0.361 | 0.123 | 0.056 | 0.024 |
| AS Vul | ASAS-SN | 12.225 | 0.168 | L18 | 0.354 | 2.636 | 3.914 | 0.314 | 0.152 | 0.134 | 0.118 | 0.019 |
| DG Vul | ASAS-SN | 13.612 | 0.101 | L18 | 0.429 | 2.681 | 4.748 | 0.934 | 0.277 | 0.178 | 0.141 | 0.026 |
| HO Vul | ASAS-SN | 5.631 | 0.200 | R21 | 0.298 | 2.849 | 5.711 | 1.698 | 0.352 | 0.134 | 0.054 | 0.014 |
| SV Vul | BER08 | 44.973 | 0.078 | L18 | 0.426 | 3.075 | 6.146 | 2.693 | 0.423 | 0.206 | 0.119 | 0.042 |
| 171305-43 | ASAS-SN | 9.561 | 0.279 | L18 | 0.303 | 3.492 | 2.012 | 3.721 | 0.070 | 0.069 | 0.080 | 0.041 |
| 181024-20 | ASAS-SN | 24.408 | 0.399 | L18 | 0.333 | 2.687 | 4.903 | 1.449 | 0.300 | 0.164 | 0.122 | 0.039 |
| 184443-04 | ASAS | 13.834 | 0.039 | L18 | 0.077 | 3.825 | 4.358 | 4.520 | 0.008 | 0.023 | 0.020 | 0.014 |
| J000234.99+6505179 | ASAS-SN | 10.931 | -0.150 | R21 | 0.162 | 6.244 | 3.392 | 0.761 | 0.086 | 0.041 | 0.008 | 0.010 |
| J052610+11513 | ASAS-SN | 4.232 | -0.060 | R21 | 0.250 | 2.793 | 5.459 | 2.538 | 0.374 | 0.159 | 0.074 | 0.033 |
| J062939-1840.5 | ASAS | 16.940 | -1.100 | T22 | 0.227 | 2.603 | 0.228 | 1.038 | 0.188 | 0.188 | 0.156 | 0.088 |
| J073502-3554.9 | ASAS-SN | 4.244 | -0.090 | K22 | 0.258 | 2.723 | 0.032 | 1.920 | 0.361 | 0.152 | 0.058 | 0.019 |
| J075840-3330.2 | ASAS-SN | 4.403 | -0.100 | K22 | 0.229 | 2.751 | 0.044 | 2.251 | 0.371 | 0.149 | 0.033 | 0.015 |
| J164120-4739.6 | ASAS | 13.020 | 0.180 | T22 | 0.131 | 2.487 | 0.282 | 1.361 | 0.184 | 0.194 | 0.025 | 0.056 |
| J180342-22110 | ASAS | 42.575 | 0.100 | R21 | 0.322 | 2.816 | 5.641 | 2.109 | 0.313 | 0.134 | 0.062 | 0.035 |
| J180946.70-1822382 | ASAS-SN | 7.289 | 0.150 | L18 | 0.294 | 3.308 | 5.815 | 0.230 | 0.314 | 0.140 | 0.048 | 0.023 |
| J182714-15071 | ASAS | 5.545 | 0.360 | R21 | 0.272 | 2.842 | 5.630 | 1.544 | 0.328 | 0.129 | 0.041 | 0.031 |
| J192007+12477 | ASAS | 8.628 | 0.310 | R21 | 0.201 | 4.162 | 1.275 | 3.943 | 0.209 | 0.053 | 0.042 | 0.020 |
| GD-CEP-0120 | ASAS-SN | 7.960 | -0.690 | T22 | 0.317 | 3.276 | 0.076 | 1.576 | 0.286 | 0.273 | 0.080 | 0.047 |
| GD-CEP-0123 | ASAS-SN | 1.399 | -0.630 | T22 | 0.062 | 2.421 | 0.193 | 0.618 | 0.563 | 0.354 | 0.248 | 0.027 |
| GD-CEP-0125 | ASAS-SN | 3.391 | -0.700 | T22 | 0.260 | 2.484 | 0.018 | 1.296 | 0.445 | 0.240 | 0.128 | 0.010 |
| GD-CEP-0127 | ASAS-SN | 13.769 | -0.340 | T22 | 0.312 | 2.792 | 0.038 | 1.133 | 0.166 | 0.117 | 0.090 | 0.013 |
| GD-CEP-0181 | ASAS-SN | 2.342 | -0.740 | T22 | 0.207 | 2.425 | 0.060 | 1.369 | 0.526 | 0.273 | 0.162 | 0.036 |
| GD-CEP-0185 | ASAS-SN | 2.541 | -0.540 | T22 | 0.238 | 2.693 | 0.179 | 1.418 | 0.504 | 0.226 | 0.163 | 0.065 |

Continued on next page

Table C.1 – continued from previous page

| Star | Source | Period | [Fe/H] | Ref. | A_1 | ϕ_{21} | ϕ_{31} | ϕ_{41} | R_{21} | R_{31} | R_{41} | σ |
|--------------|----------|--------|--------|------|-------|-------------|-------------|-------------|----------|----------|----------|----------|
| GD-CEP-0224 | ASAS-SN | 2.716 | -0.510 | T22 | 0.267 | 2.433 | 0.108 | 1.057 | 0.481 | 0.242 | 0.178 | 0.048 |
| GD-CEP-0252 | ASAS-SN | 3.185 | -0.390 | T22 | 0.158 | 2.499 | 0.244 | 2.253 | 0.383 | 0.102 | 0.073 | 0.035 |
| GD-CEP-0264 | ASAS-SN | 25.363 | -0.280 | T22 | 0.416 | 2.790 | 0.023 | 2.028 | 0.370 | 0.256 | 0.188 | 0.023 |
| GD-CEP-0271 | ASAS-SN | 2.985 | -0.660 | T22 | 0.156 | 2.736 | 0.384 | 1.139 | 0.414 | 0.118 | 0.104 | 0.064 |
| GD-CEP-0316 | ASAS-SN | 2.928 | -0.330 | T22 | 0.254 | 2.577 | 0.086 | 1.925 | 0.420 | 0.208 | 0.092 | 0.049 |
| GD-CEP-0344 | ASAS-SN | 13.119 | -0.400 | T22 | 0.329 | 3.078 | 0.076 | 1.207 | 0.219 | 0.122 | 0.145 | 0.028 |
| GD-CEP-0353 | ASAS-SN | 4.863 | -0.410 | T22 | 0.244 | 2.886 | 0.065 | 2.391 | 0.429 | 0.162 | 0.086 | 0.029 |
| GD-CEP-0568 | ASAS-SN | 45.489 | -0.200 | T22 | 0.107 | 2.803 | 0.149 | 3.099 | 0.255 | 0.117 | 0.046 | 0.024 |
| GD-CEP-0575 | ASAS-SN | 6.611 | -0.370 | T22 | 0.223 | 3.281 | 0.115 | 5.377 | 0.337 | 0.090 | 0.022 | 0.023 |
| GD-CEP-0889 | ASAS-SN | 45.232 | -0.640 | T22 | 0.198 | 3.276 | 0.092 | 3.124 | 0.426 | 0.193 | 0.112 | 0.028 |
| GD-CEP-0974 | ASAS-SN | 12.540 | 0.150 | T22 | 0.357 | 2.547 | 0.116 | 0.130 | 0.196 | 0.116 | 0.120 | 0.031 |
| GD-CEP-0996 | ASAS-SN | 6.751 | 0.280 | T22 | 0.247 | 3.087 | 0.172 | 2.674 | 0.371 | 0.125 | 0.075 | 0.061 |
| GD-CEP-1012 | ASAS-SN | 15.968 | 0.120 | T22 | 0.425 | 2.703 | 0.048 | 0.816 | 0.240 | 0.165 | 0.145 | 0.027 |
| GD-CEP-1210 | ASAS-SN | 35.847 | 0.000 | T22 | 0.202 | 2.790 | 0.104 | 2.202 | 0.417 | 0.251 | 0.125 | 0.030 |
| GD-CEP-1289 | ASAS-SN | 2.019 | -0.720 | T22 | 0.351 | 2.441 | 0.071 | 1.404 | 0.479 | 0.314 | 0.222 | 0.039 |
| GD-CEP-1298 | ASAS-SN | 3.861 | -0.350 | T22 | 0.272 | 2.727 | 0.062 | 2.133 | 0.490 | 0.245 | 0.118 | 0.050 |
| GD-CEP-1311 | ASAS-SN | 3.869 | -0.470 | T22 | 0.282 | 2.707 | 0.039 | 2.097 | 0.491 | 0.257 | 0.136 | 0.025 |
| GD-CEP-1353 | ASAS-SN | 3.150 | -0.430 | T22 | 0.256 | 2.697 | 0.122 | 1.895 | 0.505 | 0.285 | 0.092 | 0.096 |
| LMC-CEP-0107 | OGLE-IV | 8.733 | -0.430 | R22 | 0.389 | 3.381 | 6.110 | 1.490 | 0.301 | 0.210 | 0.049 | 0.026 |
| LMC-CEP-0434 | ASAS-SN | 30.353 | -0.400 | R22 | 0.210 | 2.816 | 5.762 | 2.337 | 0.328 | 0.126 | 0.049 | 0.015 |
| LMC-CEP-0461 | ASAS-SN | 45.156 | -0.300 | R22 | 0.257 | 2.880 | 5.847 | 2.500 | 0.308 | 0.123 | 0.044 | 0.021 |
| LMC-CEP-0501 | OGLE-IV | 23.300 | -0.420 | R22 | 0.480 | 2.917 | 5.690 | 2.376 | 0.380 | 0.271 | 0.188 | 0.017 |
| LMC-CEP-0510 | ASAS-SN | 36.855 | -0.380 | R22 | 0.423 | 3.126 | 6.258 | 3.002 | 0.444 | 0.239 | 0.131 | 0.024 |
| LMC-CEP-0512 | ASAS-SN | 39.461 | -0.480 | R22 | 0.432 | 3.074 | 6.184 | 2.889 | 0.459 | 0.265 | 0.156 | 0.019 |
| LMC-CEP-0528 | ASAS-SN | 35.709 | -0.410 | R22 | 0.426 | 3.127 | 0.064 | 3.093 | 0.491 | 0.278 | 0.153 | 0.026 |
| LMC-CEP-0545 | ASAS-SN | 15.828 | -0.370 | R22 | 0.288 | 2.688 | 4.306 | 0.672 | 0.207 | 0.139 | 0.151 | 0.021 |
| LMC-CEP-0590 | OGLE-IV | 31.763 | -0.410 | R22 | 0.488 | 2.962 | 6.070 | 2.789 | 0.475 | 0.298 | 0.168 | 0.015 |
| LMC-CEP-0648 | OGLE-IV | 13.622 | -0.450 | R22 | 0.374 | 2.901 | 4.218 | 0.858 | 0.134 | 0.110 | 0.115 | 0.018 |
| LMC-CEP-0655 | OGLE-IV | 12.987 | -0.410 | R22 | 0.407 | 2.992 | 4.515 | 1.039 | 0.209 | 0.114 | 0.137 | 0.008 |
| LMC-CEP-0683 | OGLE-IV | 14.674 | -0.380 | R22 | 0.423 | 2.974 | 4.494 | 0.886 | 0.203 | 0.112 | 0.145 | 0.015 |
| LMC-CEP-0712 | ASAS-SN | 20.707 | -0.330 | R22 | 0.298 | 2.692 | 5.566 | 2.198 | 0.414 | 0.251 | 0.139 | 0.017 |
| LMC-CEP-0716 | OGLE-IV | 12.187 | -0.450 | R22 | 0.354 | 2.969 | 4.480 | 0.868 | 0.197 | 0.113 | 0.142 | 0.009 |
| LMC-CEP-0727 | OGLE-IV | 14.485 | -0.550 | R22 | 0.423 | 2.816 | 4.365 | 0.423 | 0.236 | 0.170 | 0.164 | 0.016 |
| LMC-CEP-0770 | OGLE-IV | 10.854 | -0.440 | R22 | 0.316 | 3.549 | 3.108 | 5.516 | 0.047 | 0.150 | 0.109 | 0.010 |
| LMC-CEP-0787 | OGLE-IV | 17.519 | -0.380 | R22 | 0.449 | 3.017 | 5.218 | 1.571 | 0.265 | 0.131 | 0.133 | 0.012 |
| LMC-CEP-0798 | OGLE-III | 10.710 | -0.410 | R22 | 0.182 | 5.755 | 2.906 | 5.964 | 0.115 | 0.071 | 0.010 | 0.007 |
| LMC-CEP-0800 | OGLE-IV | 12.637 | -0.570 | R22 | 0.405 | 2.974 | 4.371 | 0.790 | 0.187 | 0.126 | 0.156 | 0.011 |
| LMC-CEP-0812 | OGLE-IV | 12.195 | -0.390 | R22 | 0.386 | 2.771 | 3.314 | 5.400 | 0.138 | 0.146 | 0.122 | 0.006 |
| LMC-CEP-0819 | OGLE-IV | 22.311 | -0.290 | R22 | 0.461 | 2.964 | 5.421 | 1.903 | 0.318 | 0.181 | 0.158 | 0.009 |
| LMC-CEP-0821 | OGLE-IV | 25.814 | -0.580 | R22 | 0.413 | 2.991 | 5.601 | 2.222 | 0.345 | 0.205 | 0.145 | 0.013 |
| LMC-CEP-0831 | OGLE-IV | 9.713 | -0.400 | R22 | 0.290 | 4.017 | 1.307 | 3.027 | 0.202 | 0.148 | 0.091 | 0.007 |
| LMC-CEP-0844 | OGLE-IV | 17.208 | -0.340 | R22 | 0.495 | 3.052 | 5.240 | 1.479 | 0.296 | 0.187 | 0.180 | 0.017 |
| LMC-CEP-0847 | OGLE-IV | 20.638 | -0.400 | R22 | 0.476 | 3.085 | 5.949 | 2.576 | 0.395 | 0.240 | 0.175 | 0.007 |
| LMC-CEP-0848 | OGLE-IV | 15.982 | -0.460 | R22 | 0.507 | 3.076 | 5.651 | 2.110 | 0.342 | 0.204 | 0.164 | 0.023 |
| LMC-CEP-0888 | OGLE-IV | 9.369 | -0.410 | R22 | 0.199 | 4.223 | 1.416 | 3.147 | 0.197 | 0.079 | 0.038 | 0.008 |
| LMC-CEP-0915 | OGLE-IV | 7.396 | -0.470 | R22 | 0.285 | 3.361 | 6.006 | 5.720 | 0.386 | 0.152 | 0.024 | 0.010 |
| LMC-CEP-0936 | OGLE-IV | 8.334 | -0.490 | R22 | 0.335 | 3.607 | 0.288 | 1.628 | 0.301 | 0.215 | 0.095 | 0.011 |
| LMC-CEP-0945 | ASAS-SN | 36.566 | -0.530 | R22 | 0.437 | 2.991 | 6.091 | 2.863 | 0.472 | 0.310 | 0.165 | 0.041 |
| LMC-CEP-0949 | OGLE-IV | 12.917 | -0.430 | R22 | 0.438 | 3.029 | 4.531 | 0.898 | 0.226 | 0.127 | 0.166 | 0.010 |
| LMC-CEP-0966 | ASAS-SN | 47.378 | -0.440 | R22 | 0.407 | 3.412 | 0.423 | 3.579 | 0.455 | 0.205 | 0.101 | 0.020 |
| LMC-CEP-0969 | OGLE-IV | 12.719 | -0.380 | R22 | 0.384 | 2.810 | 3.927 | 0.592 | 0.119 | 0.129 | 0.130 | 0.017 |
| LMC-CEP-0970 | OGLE-IV | 17.455 | -0.320 | R22 | 0.418 | 2.882 | 4.566 | 0.989 | 0.213 | 0.118 | 0.129 | 0.019 |
| LMC-CEP-0975 | OGLE-IV | 12.622 | -0.400 | R22 | 0.343 | 2.707 | 3.922 | 0.453 | 0.093 | 0.126 | 0.107 | 0.011 |
| LMC-CEP-0978 | OGLE-IV | 10.520 | -0.430 | R22 | 0.195 | 4.278 | 1.525 | 2.546 | 0.194 | 0.047 | 0.016 | 0.008 |
| LMC-CEP-0986 | OGLE-IV | 31.030 | -0.400 | R22 | 0.465 | 3.067 | 6.210 | 3.058 | 0.453 | 0.275 | 0.168 | 0.026 |
| LMC-CEP-0992 | ASAS-SN | 52.807 | -0.410 | R22 | 0.170 | 3.199 | 0.105 | 3.095 | 0.206 | 0.043 | 0.015 | 0.015 |
| LMC-CEP-1001 | OGLE-IV | 14.467 | -0.310 | R22 | 0.397 | 2.766 | 4.140 | 0.653 | 0.150 | 0.131 | 0.127 | 0.009 |
| LMC-CEP-1031 | OGLE-IV | 18.461 | -0.410 | R22 | 0.420 | 2.938 | 4.858 | 1.360 | 0.230 | 0.130 | 0.144 | 0.024 |
| LMC-CEP-1058 | OGLE-IV | 30.412 | -0.460 | R22 | 0.479 | 3.146 | 6.283 | 3.108 | 0.421 | 0.256 | 0.154 | 0.011 |
| LMC-CEP-1080 | OGLE-IV | 18.652 | -0.490 | R22 | 0.422 | 2.959 | 5.170 | 1.489 | 0.258 | 0.143 | 0.115 | 0.021 |
| LMC-CEP-1100 | OGLE-IV | 13.628 | -0.330 | R22 | 0.328 | 2.652 | 3.965 | 0.007 | 0.157 | 0.124 | 0.078 | 0.009 |

Continued on next page

Table C.1 – continued from previous page

| Star | Source | Period | [Fe/H] | Ref. | A_1 | ϕ_{21} | ϕ_{31} | ϕ_{41} | R_{21} | R_{31} | R_{41} | σ |
|--------------|----------|--------|--------|------|-------|-------------|-------------|-------------|----------|----------|----------|----------|
| LMC-CEP-1109 | OGLE-IV | 11.860 | -0.480 | R22 | 0.409 | 2.749 | 3.882 | 6.039 | 0.210 | 0.155 | 0.137 | 0.006 |
| LMC-CEP-1112 | OGLE-IV | 7.924 | -0.340 | R22 | 0.364 | 3.062 | 5.696 | 3.100 | 0.369 | 0.134 | 0.046 | 0.021 |
| LMC-CEP-1128 | ASAS-SN | 6.863 | -0.510 | R22 | 0.316 | 3.274 | 5.793 | 3.356 | 0.428 | 0.234 | 0.021 | 0.057 |
| LMC-CEP-1290 | ASAS-SN | 48.350 | -0.370 | R22 | 0.433 | 3.269 | 0.255 | 3.302 | 0.478 | 0.245 | 0.134 | 0.032 |
| LMC-CEP-1313 | OGLE-IV | 6.832 | -0.790 | R22 | 0.261 | 3.091 | 5.794 | 3.493 | 0.373 | 0.112 | 0.039 | 0.010 |
| LMC-CEP-1327 | OGLE-IV | 6.924 | -0.500 | R22 | 0.228 | 3.230 | 5.723 | 0.626 | 0.219 | 0.050 | 0.014 | 0.006 |
| LMC-CEP-1374 | OGLE-IV | 6.890 | -0.630 | R22 | 0.167 | 3.284 | 6.233 | 6.048 | 0.219 | 0.027 | 0.016 | 0.008 |
| LMC-CEP-1389 | OGLE-IV | 7.291 | -0.430 | R22 | 0.273 | 3.390 | 6.110 | 0.140 | 0.358 | 0.131 | 0.042 | 0.009 |
| LMC-CEP-1411 | OGLE-IV | 7.907 | -0.490 | R22 | 0.130 | 4.106 | 1.138 | 1.176 | 0.167 | 0.005 | 0.006 | 0.005 |
| LMC-CEP-1417 | OGLE-IV | 8.673 | -0.410 | R22 | 0.234 | 3.571 | 0.265 | 1.164 | 0.246 | 0.065 | 0.037 | 0.005 |
| LMC-CEP-1424 | OGLE-IV | 6.776 | -0.450 | R22 | 0.186 | 3.401 | 6.130 | 0.538 | 0.279 | 0.030 | 0.033 | 0.006 |
| LMC-CEP-1431 | OGLE-IV | 10.255 | -0.330 | R22 | 0.266 | 5.390 | 3.009 | 5.690 | 0.075 | 0.109 | 0.055 | 0.006 |
| LMC-CEP-1463 | OGLE-IV | 7.528 | -0.350 | R22 | 0.325 | 3.282 | 5.839 | 0.054 | 0.324 | 0.135 | 0.009 | 0.015 |
| LMC-CEP-1466 | OGLE-IV | 6.153 | -0.370 | R22 | 0.185 | 3.110 | 6.208 | 5.454 | 0.286 | 0.036 | 0.022 | 0.006 |
| LMC-CEP-1490 | OGLE-IV | 8.170 | -0.530 | R22 | 0.409 | 3.356 | 0.052 | 1.608 | 0.274 | 0.219 | 0.093 | 0.007 |
| LMC-CEP-1526 | OGLE-IV | 6.734 | -0.340 | R22 | 0.339 | 3.166 | 5.829 | 3.134 | 0.406 | 0.157 | 0.053 | 0.009 |
| LMC-CEP-1539 | OGLE-IV | 13.513 | -0.410 | R22 | 0.386 | 2.839 | 4.307 | 0.830 | 0.158 | 0.116 | 0.120 | 0.011 |
| LMC-CEP-1578 | OGLE-IV | 13.286 | -0.300 | R22 | 0.439 | 2.968 | 4.499 | 0.732 | 0.241 | 0.167 | 0.187 | 0.020 |
| LMC-CEP-1587 | OGLE-IV | 21.608 | -0.290 | R22 | 0.223 | 2.150 | 4.333 | 0.792 | 0.134 | 0.081 | 0.029 | 0.006 |
| LMC-CEP-1616 | OGLE-IV | 15.550 | -0.270 | R22 | 0.510 | 3.074 | 5.478 | 1.868 | 0.308 | 0.192 | 0.175 | 0.010 |
| LMC-CEP-1637 | OGLE-III | 31.960 | -0.350 | R22 | 0.454 | 3.003 | 5.960 | 2.664 | 0.471 | 0.303 | 0.095 | 0.052 |
| LMC-CEP-1641 | OGLE-IV | 13.962 | -0.340 | R22 | 0.428 | 2.666 | 4.070 | 0.000 | 0.224 | 0.164 | 0.141 | 0.011 |
| LMC-CEP-1647 | OGLE-IV | 8.692 | -0.330 | R22 | 0.314 | 3.609 | 0.874 | 2.443 | 0.178 | 0.131 | 0.085 | 0.017 |
| LMC-CEP-1677 | OGLE-IV | 23.567 | -0.310 | R22 | 0.603 | 3.049 | 5.826 | 2.474 | 0.366 | 0.230 | 0.168 | 0.029 |
| LMC-CEP-1862 | OGLE-IV | 13.123 | -0.360 | R22 | 0.336 | 2.355 | 3.801 | 0.423 | 0.078 | 0.125 | 0.090 | 0.010 |
| LMC-CEP-1939 | OGLE-IV | 6.055 | -0.370 | R22 | 0.227 | 2.959 | 5.649 | 2.506 | 0.458 | 0.149 | 0.099 | 0.054 |
| LMC-CEP-1941 | OGLE-IV | 6.805 | -0.220 | R22 | 0.177 | 3.219 | 0.503 | 5.298 | 0.256 | 0.030 | 0.019 | 0.008 |
| LMC-CEP-1994 | OGLE-III | 7.754 | -0.290 | R22 | 0.359 | 3.260 | 5.958 | 1.184 | 0.318 | 0.191 | 0.034 | 0.021 |
| LMC-CEP-2012 | OGLE-IV | 7.457 | -0.380 | R22 | 0.221 | 3.134 | 6.011 | 5.721 | 0.341 | 0.075 | 0.016 | 0.013 |
| LMC-CEP-2019 | OGLE-IV | 28.083 | -0.130 | R22 | 0.493 | 3.033 | 5.995 | 2.718 | 0.423 | 0.255 | 0.143 | 0.022 |
| LMC-CEP-2043 | OGLE-IV | 7.373 | -0.410 | R22 | 0.169 | 3.605 | 0.151 | 0.732 | 0.250 | 0.028 | 0.029 | 0.006 |
| LMC-CEP-2337 | OGLE-IV | 13.142 | -0.360 | R22 | 0.398 | 2.944 | 4.440 | 0.834 | 0.181 | 0.113 | 0.143 | 0.012 |
| LMC-CEP-2832 | OGLE-IV | 24.135 | -0.280 | R22 | 0.421 | 2.873 | 5.095 | 1.636 | 0.262 | 0.158 | 0.136 | 0.011 |
| LMC-CEP-2949 | OGLE-IV | 19.226 | -0.440 | R22 | 0.435 | 2.962 | 4.704 | 1.109 | 0.246 | 0.124 | 0.141 | 0.020 |
| LMC-CEP-3158 | OGLE-IV | 26.552 | -0.450 | R22 | 0.396 | 2.897 | 5.587 | 2.246 | 0.358 | 0.220 | 0.159 | 0.011 |
| LMC-CEP-3320 | OGLE-IV | 4.785 | -0.400 | R22 | 0.352 | 2.767 | 5.774 | 2.306 | 0.398 | 0.198 | 0.071 | 0.010 |
| LMC-CEP-3726 | OGLE-IV | 3.523 | -0.420 | L17 | 0.279 | 2.718 | 5.443 | 1.966 | 0.406 | 0.189 | 0.111 | 0.007 |
| LMC-CEP-3752 | OGLE-IV | 3.439 | -0.390 | L17 | 0.357 | 2.640 | 5.401 | 1.641 | 0.466 | 0.266 | 0.154 | 0.025 |
| LMC-CEP-4033 | OGLE-IV | 9.292 | -0.780 | R22 | 0.323 | 3.500 | 0.073 | 1.398 | 0.359 | 0.213 | 0.064 | 0.018 |
| LMC-CEP-4061 | OGLE-IV | 16.902 | -0.440 | R22 | 0.410 | 3.010 | 4.979 | 1.289 | 0.255 | 0.106 | 0.142 | 0.019 |
| LMC-CEP-4208 | OGLE-IV | 8.716 | -0.550 | R22 | 0.196 | 3.891 | 0.908 | 2.754 | 0.243 | 0.089 | 0.033 | 0.014 |
| LMC-CEP-4357 | OGLE-IV | 17.518 | -0.470 | R22 | 0.431 | 2.980 | 4.822 | 1.233 | 0.221 | 0.113 | 0.137 | 0.021 |
| LMC-CEP-4451 | OGLE-IV | 10.980 | -0.510 | R22 | 0.343 | 2.921 | 3.696 | 0.514 | 0.097 | 0.127 | 0.135 | 0.018 |
| LMC-CEP-4544 | OGLE-IV | 8.153 | -0.440 | R22 | 0.221 | 3.749 | 0.544 | 1.897 | 0.277 | 0.080 | 0.052 | 0.007 |
| LMC-CEP-4628 | ASAS-SN | 99.046 | -0.530 | R22 | 0.231 | 3.840 | 0.300 | 2.870 | 0.234 | 0.041 | 0.012 | 0.024 |
| LMC-CEP-4689 | ASAS-SN | 78.771 | -0.400 | R22 | 0.238 | 3.291 | 0.204 | 3.313 | 0.312 | 0.078 | 0.011 | 0.018 |
| SMC-CEP-0152 | OGLE-III | 15.836 | -0.650 | L17 | 0.332 | 2.507 | 4.301 | 0.196 | 0.266 | 0.158 | 0.101 | 0.009 |
| SMC-CEP-0230 | OGLE-III | 16.294 | -0.880 | L17 | 0.396 | 3.005 | 5.241 | 1.389 | 0.315 | 0.190 | 0.205 | 0.010 |
| SMC-CEP-0246 | OGLE-III | 14.382 | -0.800 | L17 | 0.322 | 2.785 | 4.680 | 1.078 | 0.263 | 0.198 | 0.158 | 0.011 |
| SMC-CEP-0423 | OGLE-III | 12.413 | -0.930 | R08 | 0.303 | 2.540 | 4.504 | 0.803 | 0.198 | 0.184 | 0.144 | 0.028 |
| SMC-CEP-0431 | ASAS-SN | 16.740 | -0.720 | L17 | 0.242 | 2.970 | 5.427 | 1.726 | 0.313 | 0.177 | 0.164 | 0.036 |
| SMC-CEP-0574 | ASAS-SN | 31.928 | -0.910 | R08 | 0.403 | 3.032 | 6.065 | 2.891 | 0.423 | 0.298 | 0.194 | 0.042 |
| SMC-CEP-0921 | ASAS-SN | 65.875 | -0.840 | R08 | 0.374 | 3.577 | 0.756 | 4.054 | 0.423 | 0.176 | 0.077 | 0.028 |
| SMC-CEP-1502 | ASAS-SN | 83.645 | -0.870 | R08 | 0.294 | 3.850 | 1.099 | 3.809 | 0.347 | 0.081 | 0.028 | 0.019 |
| SMC-CEP-2099 | ASAS-SN | 73.742 | -0.740 | R08 | 0.225 | 3.153 | 6.091 | 2.605 | 0.585 | 0.240 | 0.104 | 0.018 |
| SMC-CEP-2470 | ASAS-SN | 42.669 | -0.940 | R08 | 0.357 | 3.298 | 0.260 | 3.395 | 0.424 | 0.211 | 0.126 | 0.040 |
| SMC-CEP-3212 | ASAS-SN | 27.061 | -0.860 | R08 | 0.379 | 3.015 | 5.862 | 2.608 | 0.374 | 0.231 | 0.183 | 0.047 |
| SMC-CEP-3565 | ASAS-SN | 16.696 | -0.870 | R08 | 0.276 | 2.503 | 4.005 | 6.110 | 0.256 | 0.172 | 0.110 | 0.040 |
| SMC-CEP-4017 | ASAS-SN | 33.707 | -0.750 | R08 | 0.323 | 3.140 | 6.226 | 2.990 | 0.396 | 0.208 | 0.116 | 0.037 |
| SMC-CEP-4444 | ASAS-SN | 41.848 | -0.780 | R08 | 0.323 | 2.986 | 6.018 | 2.554 | 0.572 | 0.328 | 0.176 | 0.031 |
| SMC-CEP-4555 | ASAS-SN | 22.639 | -0.760 | R08 | 0.287 | 2.612 | 5.068 | 1.505 | 0.302 | 0.172 | 0.103 | 0.023 |

Continued on next page

Table C.1 – continued from previous page

| Star | Source | Period | [Fe/H] | Ref. | A_1 | ϕ_{21} | ϕ_{31} | ϕ_{41} | R_{21} | R_{31} | R_{41} | σ |
|--------------|---------|--------|--------|------|-------|-------------|-------------|-------------|----------|----------|----------|----------|
| SMC-CEP-4697 | ASAS-SN | 18.899 | -0.930 | R08 | 0.348 | 2.615 | 4.552 | 0.626 | 0.298 | 0.214 | 0.146 | 0.044 |
| SMC-CEP-4919 | ASAS-SN | 33.341 | -0.980 | R08 | 0.411 | 3.069 | 6.185 | 3.018 | 0.487 | 0.324 | 0.212 | 0.047 |
| SMC-CEP-4953 | ASAS-SN | 21.392 | -0.940 | R08 | 0.364 | 3.099 | 5.860 | 2.490 | 0.338 | 0.221 | 0.181 | 0.035 |